STRUCTURAL/FUNCTIONAL INSIGHTS DERIVED FROM STUDIES OF

HUMAN AND ZEBRAFISH CFTR ORTHOLOGS

A Dissertation

presented to

the Faculty of the Graduate School

at the University of Missouri-Columbia

In Partial Fulfillment

of the Requirements for the Degree

Doctor of Philosophy

---

by

JINGYAO ZHANG

Dr. Tzyh-Chang Hwang, Dissertation Supervisor

July 2018

The undersigned, appointed by the dean of the Graduate School, have examined the dissertation entitled

STRUCTURAL/FUNCTIONAL INSIGHTS DERIVED FROM STUDIES OF

HUMAN AND ZEBRAFISH CFTR ORTHOLOGS

Presented by Jingyao Zhang,

a candidate for the degree of doctor of philosophy,

and hereby certify that, in their opinion, it is worthy of acceptance.

_____

Dr. Tzyh-Chang Hwang, Medical Pharmacology and Physiology

_____

Dr. Kevin Gillis, Biological Engineering

_____

Dr. Liqun Gu, Biological Engineering

_____

Dr. Shinghua Ding, Biological Engineering

_____

Dr. Xiaoqin Zou, Physics

'Thank you' is not enough to deliver my gratefulness to my family. I was raised up by my grandparents and they constantly provide the strongest support they can for my dream chasing. We miss each other so much and I feel guilty for being absent from them for so many years chasing my own dream while they are getting older and older. I can't wait flying back to their house to stay with them and do my best to make up the time for them. I love you all.

To my dear Siyang, my best friend and my love. You shared my suffering and grant your joy with me. It is my biggest luck to meet you in Columbia and thank you so much for your companion. Since you are becoming busier, let me share the stress with you. Love you.

Thank myself for the persistence. Doctor degree is one of my dreams but I was once so close to give it up seven years ago. So glad that I finally insisted.

ACKNOWLEDGEMENTS

First, I would like to give my sincere thanks to my academic advisor Dr. Hwang for giving me the privilege to work and study in his lab towards my doctoral degree. When my memory flashes back over the past six years, it was really not easy to work with Dr. Hwang because of his high standard on data quality, his punctuality in following up my research progress, his rigorousness in analyzing and interpreting data and his critical thinking in our academic discussions. But it is the hard time that makes me grow the most and trains me how to do good science. It is also not hard to work with Dr. Hwang since he is already a role model in many aspects not only in academia but also in being a good and decent person. All I have to do is to simply follow him and work just like him. I am so grateful for the time learning after his guidance and so sure that what I have learnt from him will constantly benefit me in the rest of my life.

Second, I would like to thank my all committee members Dr. Zou, Dr. Gu, Dr. Gillis and Dr. Ding, for their critical discussions with me and their advices on improving my research as well as my scientific writing. Especially, I would like to apologize to them and thank them again for being so considerate when I have to arrange the committee meetings urgently without making the appointments long time in advance.

I would also thank all my lab members for their advices and help in the past years since I know without them, I am not able to finish the demanding research and the PhD program. Thank Cindy for making the large amount of constructs, which is so exhausting. Thank Shenghui for being a good friend, for his expertise in maintaining our sensitive and complicated setups and for his brilliant advices on how to debug when the things

TABLE OF CONTENTS

LIST OF ILLUSTRATIONS

STRUCTURAL/FUNCTIONAL INSIGHTS DERIVED FROM STUDIES OF

HUMAN AND ZEBRAFISH CFTR ORTHOLOGS

Jingyao Zhang

Dr. Tzyh-Chang Hwang, Dissertation Supervisor

ABSTRACT

Cystic fibrosis transmembrane conductance regulator (CFTR) chloride channels
play a critical role in regulating the trans-epithelial movement of water and electrolyte in
exocrine tissues and the malfunctions of CFTR result in cystic fibrosis, the most
prevalent lethal autosomal recessive hereditary disease among the Caucasian populations.
Despite decades of biochemical and biophysical studies of CFTR, our understanding of
CFTR's structure and gating mechanism remains limited. My dissertation research started
with a focus on the structural and functional contribution of the fifth transmembrane
segment (TM5) of human CFTR in forming the chloride permeation pathway and
continued into tackling the role of the electrostatic profile in the pore for anion flux.
These studies have led to the following conclusions: First, TM5 indeed contributes to
forming the chloride permeation pathway but TM7 does not line the pore. Unlike the
well-studied TM1, TM6, and TM12, the six identified pore-lining residues (A299, R303,
N306, S307, F310 and F311) in TM5 only line the internal vestibule of the pore, not the
narrow region nor the outer vestibule. Second, changing the side-chain properties of
several pore-lining residues along TM5 resulted in channels with two distinct
subconductance levels, small conductance O_1 state and large conductance O_2 state,

respectively. Intriguingly, the preferred gating transition $C{\rightarrow}O_1{\rightarrow}O_2{\rightarrow}C$ over

$C{\rightarrow}O_2{\rightarrow}O_1{\rightarrow}C$ (namely the O_1O_2 phenotype) as reported previously for R352 mutations

suggests the existence of an irreversible gating process attributed to the input of the free

energy from ATP hydrolysis. Then the timely solution of the cryo-EM structures of

human and zebrafish CFTR offers a great opportunity to interweave the structural and

functional data for a comprehensive understanding of CFTR. Taking a full advantage of

this opportunity, I launched a thorough investigation of zebrafish CFTR to fill the blank

of functional data for this ortholog. Although current cryo-EM data show minimal

structural differences between human and zebrafish CFTR, my electrophysiological

characterization of zebrafish CFTR revealed unexpected functional differences, which

subsequently offer novel mechanistic insights regarding the mechanism of CFTR gating

by ATP binding and hydrolysis.

CHAPTER 1

Introduction

1.1. CFTR causes cystic fibrosis

Cystic fibrosis (CF), the most prevalent lethal autosomal recessive hereditary disease among the Caucasian populations, is caused by the malfunctions of the anion channel protein cystic fibrosis transmembrane conductance regulator (CFTR) encoded by the *cftr* gene (Riordan et al., 1989). CFTR is found mainly in the apical membrane of epithelial cells and plays a critical role in regulating the trans-epithelial movement of water and electrolyte in many tubular organs such as the airways, the gastrointestinal tract, the biliary duct, the pancreas, the sweat duct and the reproductive organs (Cohn et al., 1993; Huang et al., 2001; Pezzulo et al., 2012; Pettit and Fellner, 2014). The loss of function mutations in *cftr* result in severe alteration of the lungs and intestines due to abnormal surface hydration (condensed mucus) induced inflammation and infection or insufficient nutrient supply (Riordan, 2008; Boyle and De Boeck, 2013; Stoltz et al., 2015).

So far, over 2000 mutations in *cftr* have been identified, and many of them (http://www.genet.sickkids.on.ca) are found in more than 85,000 CF patients worldwide (De Boeck and Amaral, 2016). Although most of the mutations are rare, some are quite common, including ΔF508, G551D and G542X, which account for 70%, 5% and 5% of the worldwide CF-associated alleles respectively (Sosnay et al., 2013; Eckford et al., 2014; Molinski et al., 2014; Veit et al., 2016). More than two decades of basic studies of

CFTR in academia have made great strides in moving the field forward. Furthermore, many years of drug screening in pharmaceutical industry also led to the discovery of CFTR modulators that are approved by FDA for the treatment of patients with CF (e.g. ivacaftor and lumacaftor). These reagents either increase the surface expression of CFTR proteins (i.e., CFTR correctors) or increase the activity of channels that are successfully expressed and delivered into the membrane, i.e., CFTR potentiators (Van Goor et al., 2009; Accurso et al., 2010; Ramsey et al., 2011; Van Goor et al., 2011; He et al., 2013; Loo et al., 2013; Ren et al., 2013). While improvements in traditional therapies for CF have prolonged the median life expectancy of CF patients from around 1 year in 1950 to around 40 years old at present (Elborn, 2016), scientific achievements in the past two decades are expected to further improve not only life expectancy, but also life quality.

1.2. CFTR's basic architecture

According to the sequence and domain analysis, CFTR is categorized into the ATP Binding Cassette transporter superfamily (ABC superfamily) (Riordan et al., 1989; Dean and Annilo, 2005), whose members are mostly active transporters carrying a broad range of substrates across the cell membrane against their electrochemical gradients (Davidson and Maloney, 2007; Oldham et al., 2008; Kathawala et al., 2015). Unlike all the other members in the family that are transporters, CFTR is unique for functioning as a chloride channel (Bear et al., 1992). Bearing high structural resemblance to ABC transporters, the basic architecture of CFTR (Figure 1.1) contains two Transmembrane Domains (TMD1 and TMD2), each of which is constituted of six transmembrane segments (TM1- TM6 in TMD1 and TM7- TM12 in TMD2) and each TMD is followed by a cytosolic Nucleotide

Binding Domain (NBD1 and NBD2 respectively). CFTR has a unique cytosolic

Regulatory Domain (RD) that links the two sets of TMD-NBD complex. The role of RD

is to regulate the activity of CFTR through phosphorylation/dephosphorylation of its

multiple phosphorylation sites (Berger et al., 1991; Cohn et al., 1992; Picciotto et al.,

1992; Gadsby et al., 2006; Chen and Hwang, 2008; Hwang and Sheppard, 2009; Hwang

and Kirk, 2013).
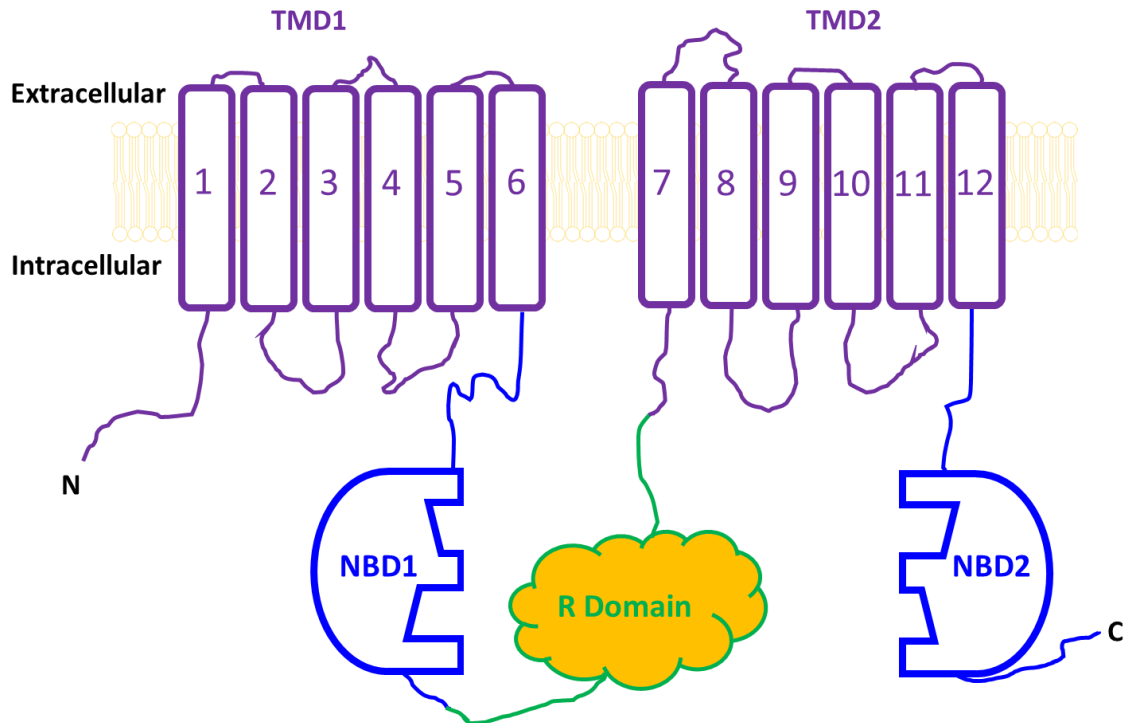
Figure 1.1. CFTR topology structure. CFTR has two TMDs (TMD1 and TMD2) that are responsible to form the continuous anion permeation pathway (pore) and the gate of the channel. Each TMD is constituted of six transmembrane segments (TM1- TM6 in TMD1, and TM7- TM12 in TMD2) and is followed by a cytosolic Nucleotide Binding Domain (NBD1 and NBD2 respectively). CFTR also has a unique cytosolic Regulatory Domain (RD) that links the two sets of TMD-NBD complex.

1.3. CFTR's gating mechanisms are under debate

For CFTR to function as an anion channel just like all ion channel proteins, CFTR must have a key functional unit for a channel: a continuous permeation pathway (pore) for ions to past through the membrane. The pore of CFTR is formed by its 12 TMs in the two TMDs (Figure 1.1) based on hydrophobicity analysis. The RD and NBDs play major roles in regulating and driving the gating cycles of the channel properly according to the physiological needs (Hwang et al., 2018). In short, CFTR is a PKA-phosphorylation activated, ATP gated chloride channel.

Before CFTR can open and close properly, the RD has to be phosphorylated by cyclic AMP-dependent protein kinase A (PKA) (Berger et al., 1991; Cohn et al., 1992; Picciotto et al., 1992; Chen and Hwang, 2008; Hwang and Sheppard, 2009). After fully phosphorylation, the opening and closing of the gate in the TMDs are mainly controlled by ATP binding/hydrolysis at CFTR's two cytosolic nucleotide-binding domains NBD1 and NBD2 (Higgins and Linton, 2004; Vergani et al., 2005; Gadsby et al., 2006; Hwang and Sheppard, 2009; Locher, 2009; Rees et al., 2009). The transition of the TMDs from the closed state (inward-facing conformation) to the open state (outward-facing conformation) is linked to the ATP-mediated NBD1/NBD2 dimerization in a head-to-tail configuration (Vergani et al., 2005; Sohma and Hwang, 2015). We have a relatively good understanding of the role of CFTR's two ATP binding sites (Site 1 and Site 2) at the NBD dimer interface in gating, as NBDs follow the canonical architectures among all ABC proteins (Lewis et al., 2004; Lewis et al., 2005). Site 1 is formed between the head subdomain from NBD1 and the tail subdomain from NBD2 and Site 2 is formed between the head subdomain from NBD2 and the tail subdomain from NBD1. However, our

understanding of the strictness about the coupling mechanisms between the conformational changes in CFTR's TMDs (opening and closing events) and those in the NBDs (ATP binding to NBDs, NBD dimerization, ATP hydrolysis and release of the hydrolytic products from the NBDs, dissociation of the tight NBD dimer) is still incomplete and under debate, especially on how and when the channel closes in relation to ATP hydrolysis. Two gating models describing the molecular motions of NBDs and TMDs are currently available (Csanady et al., 2010; Jih and Hwang, 2012; Jih et al., 2012; Jih et al., 2017; Liu et al., 2017). On one hand, the strict coupling gating model dictates that opening of the gate in the TMDs is triggered by the dimerization of the NBDs; whereas the gate closure is associated with hydrolysis-induced partial/complete separation of the NBD dimer (Tsai et al., 2009; Csanady et al., 2010; Tsai et al., 2010), resulting in a one-to-one stoichiometry between the gating cycle and the ATP hydrolysis cycle. On the other hand, the energetic coupling model portrays a probabilistic relationship between NBD dimerization and gate opening: NBD dimerization makes the gate more likely to open and separation of the NBDs makes the gate more likely to close (Jih and Hwang, 2012). Thus one gating cycle is not strictly coupled with one ATP hydrolysis cycle. In other words, each gating cycle is not necessarily coupled to hydrolysis of one molecule of ATP (Figure 1.2).
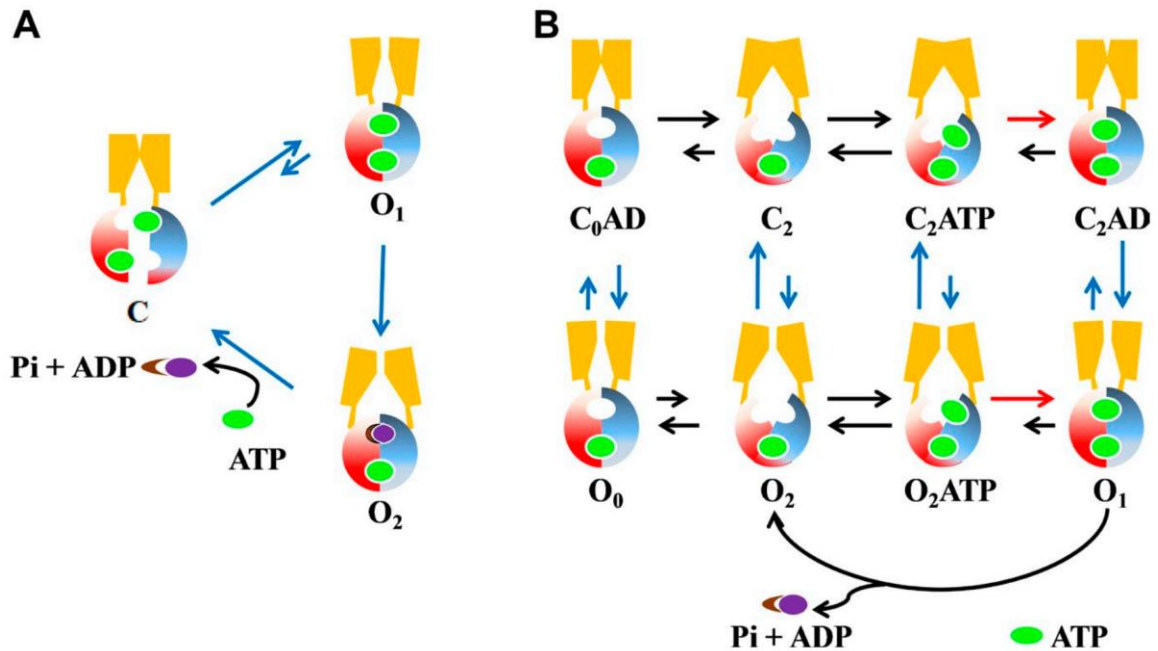
Figure 1.2. Two coupling models of CFTR. A. Strict coupling model depicted in Liu et at. (2017). NBD dimerization is coupled to channel opening (O_1 state). Once one ATP is hydrolyzed (O_2 state), ATP hydrolysis and the release of hydrolytic produces (P_i + ADP) from NBD binding interface trigger the dissociation of the NBD dimer that closes the gate (C state). **B.** Energetic coupling model shown in Jih et at. (2017). In this model, the NBD dimerization facilitates but does not guarantee the opening of the channel. Meanwhile, ATP hydrolysis, subsequent release of the hydrolytic products from the NBD binding interface and the eventual dissociation of the NBD dimer facilitate but do not guarantee closing of the channel. The motions of the NBDs and TMDs are coupled energetically, following a probabilistic relationship.

In the field of biophysics, the patch-clamp technique is widely employed to monitor the opening and closing events in real time even at a single channel level by measuring the current passing through the open channel. However, if the open channel conformation only shows one uniform conductance level like human WT-CFTR (see representative trace in Figure 4.3A) as well as most CFTR mutations studied so far, regular single-channel recordings simply reflect the status of the gate in TMDs, and do not directly tell the molecular events such as ATP hydrolysis in NBDs. However, previous reports in our lab show that some CFTR mutations (e.g., R352C, R352Q) exhibit two distinct open-channel conductance levels (Jih et al., 2012): a smaller level O_1 and a larger one O_2. The preferred gating topology $C \rightarrow O_1 \rightarrow O_2 \rightarrow C$ over $C \rightarrow O_2 \rightarrow O_1 \rightarrow C$ (namely the O_1O_2 phenotype) seen in these mutations suggests an input of free energy from ATP hydrolysis to drive the $O_1 \rightarrow O_2$ transition. My investigation into the role of TM5, elaborated in Chapter 2, not only supports the notion that TM5 lines the CFTR pore, but also identified several mutations in TM5 that show similar O_1O_2 phenotype. This study on visualizing the process of ATP hydrolysis will be elaborated in Chapter 3, where the O_1O_2 phenotype allows us to discern the pre- and post-hydrolytic open states within an opening burst.

1.4. CFTR's asymmetrical pore

As a key component of an anion channel, the structure of CFTR's pore is always one of the central topics of interest. Whether a CFTR research project is trying to address a structural or functional question, a good understanding of the pore architecture is no doubt of great help. Biophysical data collected over the past two decades suggest four functional components of a continuous chloride permeation pathway in CFTR: 1) a

lateral entrance (El Hiani and Linsdell, 2015; El Hiani et al., 2016) between TM4 and

TM6, 2) a large internal vestibule (Bai et al., 2011), 3) a narrow region that may serve as

a gate and selectivity filter (Gao and Hwang, 2015; Linsdell, 2016) and 4) a shallow

external vestibule (Muanprasat et al., 2004; Norimatsu et al., 2012) (Figure 1.3).
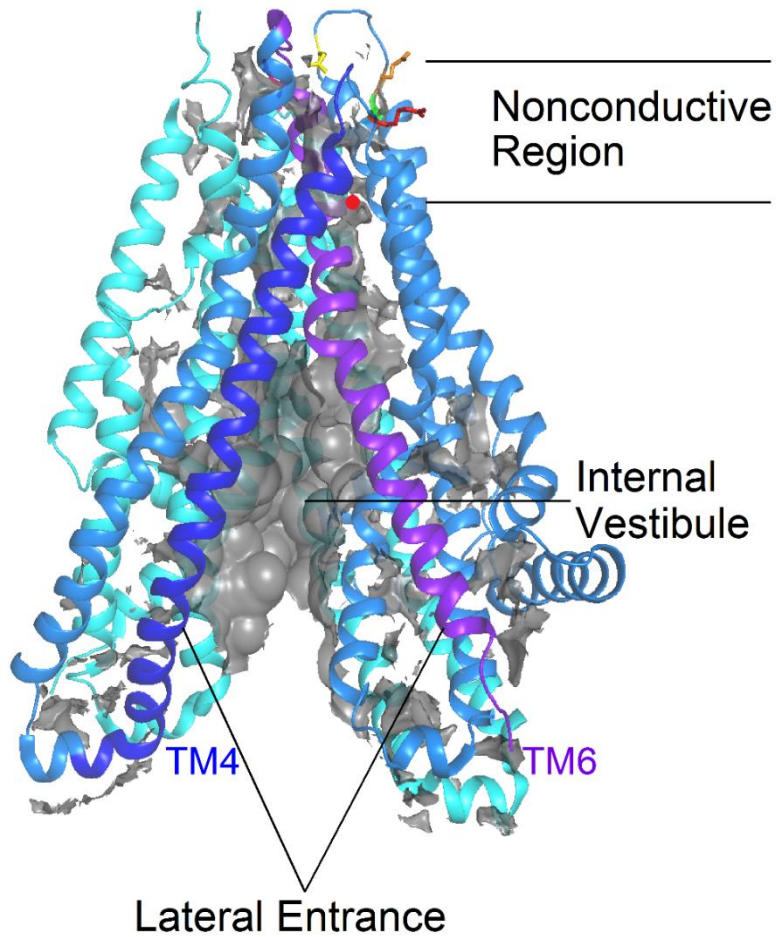
Figure 1.3. Lateral view of CFTR's pore architecture. The pore architecture of CFTR contains a lateral entrance framed by TM4 (in blue) and TM6 (in purple), a spacious internal vestibule (in gray) that narrows down while protruding to the extracellular side and a nonconductive region that contains the selectivity filter in the open state and the gate in the closed state, where local close contacts among TMs obstruct the pore to close the gate. Other 10 TMs are shown as ribbons in light blue (TMD1) and cyan (TMD2). A red dot marks the end of the water accessible space in the internal vestibule in this unphosphorylated human CFTR structure in the closed state (Liu et al., 2017). Of note, the red dot is shifted away from the central axis of the pore, which adds one more evidence for an asymmetrical pore. (Adopted from Hwang et al, 2018)

Up to date, functional data collected from substituted cysteine accessibility method (SCAM) studies have suggested that the pore of CFTR is contributed by TM1 (Wang et al., 2011; Gao et al., 2013), TM3 (Norimatsu et al., 2012; El Hiani et al., 2016), TM4 (El Hiani et al., 2016), TM5 (Zhang and Hwang, 2015; El Hiani et al., 2016), TM6 (Fatehi and Linsdell, 2008; Alexander et al., 2009; Bai et al., 2010; El Hiani and Linsdell, 2010; Norimatsu et al., 2012; El Hiani et al., 2016), TM9 (Norimatsu et al., 2012), TM10 (El Hiani and Linsdell, 2015), TM11 (Wang et al., 2014) and TM12 (Bai et al., 2011; Qian et al., 2011; Norimatsu et al., 2012; Gao and Hwang, 2015). On the contrary, TM7 is not pore-lining (Wang et al., 2014; Zhang and Hwang, 2015) contradicting the presumed two-fold symmetry seen in other ABC transporters' TMDs (Dawson and Locher, 2006; Aller et al., 2009). Although the pore structure above depicted in the unit of TM is quite rough and TM2 and TM8 are still waiting for thorough SCAM investigation, it is already safe to point out that the permeation pathway of CFTR is asymmetrically contributed by the TMs. For instance TM1 contributes to the whole length of the pore (Gao et al., 2013; Gao and Hwang, 2015, 2016) but its counterpart TM7 does not line the pore at all (Zhang and Hwang, 2015); TM6 in TMD1 and the corresponding TM12 in TMD2 play different roles in the construction of the pore (Bai et al., 2011; Gao and Hwang, 2016).

In my first two projects using patch-clamp technique combined with several other molecular biology and pharmacology approaches, I focused my research on the role of TM5 and TM7 in lining the pore and the changes of pore-lining residues upon ATP hydrolysis, which will be elaborated thoroughly in Chanter 2 and Chapter 3.

1.5. Cryo-EM structures offer structural insights at an atomic level.

More than two decades of biochemical and biophysical studies no doubt have shed light on revealing the structure/function relationship of this medically important molecule. Recently, three ground-breaking cryo-EM structures of CFTR became available with high resolution right after my studies described in Chapter 2 and Chapter 3 were published. These structures include unphosphorylated human and zebrafish CFTR (hCFTR and zCFTR), as well as phosphorylated ATP-bound zebrafish CFTR (Zhang and Chen, 2016; Liu et al., 2017; Zhang et al., 2017). The unphosphorylated human and zebrafish CFTR (hCFTR and zCFTR) show widely separated NBDs with the TMDs in the closed state. The phosphorylated ATP-bound zebrafish CFTR shows a tight NBD dimer consistent with the proposed head-to-tail dimer conformation by functional studies (Vergani et al., 2005; Sohma and Hwang, 2015), although the TMDs stay in a surprising closed state. These three structures offer investigators an unprecedented opportunity to not only re-examine previously published biochemical/biophysical results at a molecular level but also propose possible new directions of research using the structures as a guide.

Naturally, it is a good time to re-exam my published work described in Chapter 2 and Chapter 3 using the high-resolution cryo-EM structures as my references. Indeed, as I proposed, TM5 lines the pore in all three structures right at the positions of the six pore-lining residues (A299, R303, N306, S307, F310 and F311) I have identified. In addition, TM7 does not line the pore in all three structures, exactly as proposed in Chapter 2. Furthermore, detailed comparison among the three structures suggests that the internal vestibule of the pore when the two NBDs form a tight dimer (Zhang et al., 2017) is indeed much smaller than that in the closed state conformation when the two NBDs are widely apart (Zhang and Chen, 2016; Liu et al., 2017). If we accept the idea that the latest

phosphorylated, ATP-bound zCFTR structure is closely similar to the open channel

conformation when the two NBDs form a tight dimer, it seems reasonable to speculate

that the internal vestibule of a real open channel conformation with the two NBDs in a

tight dimerization form should also be as small and should undergo expansion during its

transition towards the closed channel. This speculation is again consistent with what we

proposed in Chapter 3 after studying the differential blocking effect of channel blocker

MOPS$^-$ on CFTR and the changes of the pore-lining residues upon ATP hydrolysis.

Furthermore, a more thorough re-examination between the cryo-EM structures and

currently available functional data indeed suggest a high consistency with only minor

unresolved discrepancies (see details in review by Hwang et al., 2018). For instance, the

three structures confirm a lateral anion entrance between TM4 and TM6, consistent with

the proposed location of a major anion entrance by functional data (El Hiani and Linsdell,

2015). Moreover, these three structures also confirm the idea that CFTR has an

asymmetrical pore, an idea derived from large amount of functional data (Bai et al., 2010,

2011; Gao and Hwang, 2015; Zhang and Hwang, 2015).

1.6. Comparative studies of human and zebrafish CFTR orthologs

Despite millions of years of phylogenetic distance between human and zebrafish, the

structures of unphosphorylated zCFTR and hCFTR exhibit remarkable similarities

(Zhang and Chen, 2016; Liu et al., 2017). However, biochemical/biophysical studies also

repetitively highlight the delicateness of proteins, where minor changes or a single

mutation within the amino acid sequence could result in dramatic functional divergence

such as G551D, ΔF508 in CFTR. That's also why site-directed mutagenesis is a powerful tool in the study of proteins. More specifically, my own electrophysiology data also emphasize that tiny local changes of the interval vestibule such as mutant R352C and N306D not only elicit different gating activities, but also show multiple subconductance levels within one single opening burst (see Chapter 3). Following this principle of protein delicateness, we are extremely cautious of using the zebrafish CFTR structures to interpret or explain the functional data from human CFTR considering the 55% sequence identity between zebrafish and human CFTR orthologs. Although the two zebrafish CFTR structures representing two different conformational states show a large extent of consistency with the current available functional data mostly achieved from human CFTR, the lack of the functional data for zebrafish CFTR severely restricted our utilization of these precious structures. Thus, following the first two projects studying TM7, TM5 and the electrostatic tuning of the internal vestibule, I thoroughly characterized the functional properties of zebrafish CFTR expressed in Chinese Hamster Ovary (CHO) cells and compared the functional differences between human and zebrafish CFTR orthologs. My data suggest that indeed, zebrafish CFTR shows a large extent of functional differences from human CFTR despite their 55% sequence identity, not only in its gating behaviors but also in its responses to ATP analogues, inhibitor and CFTR potentiators. Detailed information about this series of studies is elaborated in Chapter 4.

1.7. References

Accurso, F.J., S.M. Rowe, J.P. Clancy, M.P. Boyle, J.M. Dunitz, P.R. Durie, S.D. Sagel, D.B. Hornick, M.W. Konstan, S.H. Donaldson, R.B. Moss, J.M. Pilewski, R.C. Rubenstein, A.Z. Uluer, M.L. Aitken, S.D. Freedman, L.M. Rose, N. Mayer-Hamblett, Q. Dong, J. Zha, A.J. Stone, E.R. Olson, C.L. Ordonez, P.W. Campbell, M.A. Ashlock, and B.W. Ramsey. 2010. Effect of VX-770 in persons with cystic fibrosis and the G551D-CFTR mutation. *The New England journal of medicine*. 363:1991-2003.

Alexander, C., A. Ivetac, X. Liu, Y. Norimatsu, J.R. Serrano, A. Landstrom, M. Sansom, and D.C. Dawson. 2009. Cystic Fibrosis Transmembrane Conductance Regulator: Using Differential Reactivity toward Channel-Permeant and Channel-Impermeant Thiol-Reactive Probes To Test a Molecular Model for the Pore. *Biochemistry*. 48:10078-10088.

Aller, S.G., J. Yu, A. Ward, Y. Weng, S. Chittaboina, R. Zhuo, P.M. Harrell, Y.T. Trinh, Q. Zhang, I.L. Urbatsch, and G. Chang. 2009. Structure of P-Glycoprotein Reveals a Molecular Basis for Poly-Specific Drug Binding. *Science*. 323:1718-1722.

Bai, Y., M. Li, and T.C. Hwang. 2010. Dual roles of the sixth transmembrane segment of the CFTR chloride channel in gating and permeation. *The Journal of general physiology*. 136:293-309.

Bai, Y., M. Li, and T.C. Hwang. 2011. Structural basis for the channel function of a

degraded ABC transporter, CFTR (ABCC7). *The Journal of general physiology*.

138:495-507.

Bear, C.E., C.H. Li, N. Kartner, R.J. Bridges, T.J. Jensen, M. Ramjeesingh, and J.R.

Riordan. 1992. Purification and functional reconstitution of the cystic fibrosis

transmembrane conductance regulator (CFTR). *Cell*. 68:809-818.

Berger, H.A., M.P. Anderson, R.J. Gregory, S. Thompson, P.W. Howard, R.A. Maurer, R.

Mulligan, A.E. Smith, and M.J. Welsh. 1991. Identification and regulation of the

cystic fibrosis transmembrane conductance regulator-generated chloride channel.

The Journal of clinical investigation. 88:1422-1431.

Boyle, M.P., and K. De Boeck. 2013. A new era in the treatment of cystic fibrosis:

correction of the underlying CFTR defect. *The lancet. Respiratory medicine*.

1:158-163.

Chen, T.Y., and T.C. Hwang. 2008. CLC-0 and CFTR: Chloride Channels Evolved From

Transporters. *Physiological reviews*. 88:351-387.

Cohn, J.A., A.C. Nairn, C.R. Marino, O. Melhus, and J. Kole. 1992. Characterization of

the cystic fibrosis transmembrane conductance regulator in a colonocyte cell line.

Proceedings of the National Academy of Sciences of the United States of America.

89:2340-2344.

Cohn, J.A., T.V. Strong, M.R. Picciotto, A.C. Nairn, F.S. Collins, and J.G. Fitz. 1993.

Localization of the cystic fibrosis transmembrane conductance regulator in human

bile duct epithelial cells. *Gastroenterology*. 105:1857-1864.

Csanady, L., P. Vergani, and D.C. Gadsby. 2010. Strict coupling between CFTR's catalytic cycle and gating of its Cl- ion pore revealed by distributions of open channel burst durations. *Proceedings of the National Academy of Sciences of the United States of America*. 107:1241-1246.

Davidson, A.L., and P.C. Maloney. 2007. ABC transporters: how small machines do a big job. *Trends in Microbiology*. 15:448-455.

Dawson, R.J., and K.P. Locher. 2006. Structure of a bacterial multidrug ABC transporter. *Nature*. 443:180-185.

De Boeck, K., and M.D. Amaral. 2016. Classification of CFTR mutation classes - Authors' reply. *The lancet. Respiratory medicine*.

Dean, M., and T. Annilo. 2005. Evolution of the ATP-binding cassette (ABC) transporter superfamily in vertebrates. *Annual review of genomics and human genetics*. 6:123-142.

Eckford, P.D., M. Ramjeesingh, S. Molinski, S. Pasyk, J.F. Dekkers, C. Li, S. Ahmadi, W. Ip, T.E. Chung, K. Du, H. Yeger, J. Beekman, T. Gonska, and C.E. Bear. 2014. VX-809 and Related Corrector Compounds Exhibit Secondary Activity Stabilizing Active F508del-CFTR after Its Partial Rescue to the Cell Surface. *Chemistry & biology*. 21:666-678.

El Hiani, Y., and P. Linsdell. 2010. Changes in accessibility of cytoplasmic substances to the pore associated with activation of the cystic fibrosis transmembrane conductance regulator chloride channel. *The Journal of biological chemistry*. 285:32126-32140.

El Hiani, Y., and P. Linsdell. 2015. Functional Architecture of the Cytoplasmic Entrance to the Cystic Fibrosis Transmembrane Conductance Regulator Chloride Channel Pore. *The Journal of biological chemistry*. 290:15855-15865.

El Hiani, Y., A. Negoda, and P. Linsdell. 2016. Cytoplasmic pathway followed by chloride ions to enter the CFTR channel pore. *Cellular and molecular life sciences : CMLS*. 73:1917-1925.

Elborn, J.S. 2016. Cystic fibrosis. *Lancet*.

Fatehi, M., and P. Linsdell. 2008. State-dependent access of anions to the cystic fibrosis transmembrane conductance regulator chloride channel pore. *The Journal of biological chemistry*. 283:6102-6109.

Gadsby, D.C., P. Vergani, and L. Csanády. 2006. The ABC protein turned chloride channel whose failure causes cystic fibrosis. *Nature*. 440:477-483.

Gao, X., Y. Bai, and T.C. Hwang. 2013. Cysteine scanning of CFTR's first transmembrane segment reveals its plausible roles in gating and permeation. *Biophys J*. 104:786-797.

Gao, X., and T.C. Hwang. 2015. Localizing a gate in CFTR. *Proceedings of the National Academy of Sciences of the United States of America*.

Gao, X., and T.C. Hwang. 2016. Spatial positioning of CFTR's pore-lining residues affirms an asymmetrical contribution of transmembrane segments to the anion permeation pathway. *The Journal of general physiology*. 147:407-422.

He, L., P. Kota, A.A. Aleksandrov, L. Cui, T. Jensen, N.V. Dokholyan, and J.R. Riordan. 2013. Correctors of DeltaF508 CFTR restore global conformational maturation without thermally stabilizing the mutant protein. *FASEB journal : official publication of the Federation of American Societies for Experimental Biology*. 27:536-545.

Higgins, C.F., and K.J. Linton. 2004. The ATP switch model for ABC transporters. *Nature Structural & Molecular Biology*. 11:918-926.

Huang, P., E.R. Lazarowski, R. Tarran, S.L. Milgram, R.C. Boucher, and M.J. Stutts. 2001. Compartmentalized autocrine signaling to cystic fibrosis transmembrane conductance regulator at the apical membrane of airway epithelial cells. *Proceedings of the National Academy of Sciences of the United States of America*. 98:14120-14125.

Hwang, T.C., and K.L. Kirk. 2013. The CFTR ion channel: gating, regulation, and anion permeation. *Cold Spring Harbor perspectives in medicine*. 3:a009498.

Hwang, T.C., and D.N. Sheppard. 2009. Gating of the CFTR Cl- channel by ATP-driven nucleotide-binding domain dimerisation. *The Journal of physiology*. 587:2151-2161.

Hwang, T.C., J.T. Yeh, J. Zhang, Y.C. Yu, H.I. Yeh, and S. Destefano. 2018. Structural mechanisms of CFTR function and dysfunction. *The Journal of general physiology*.

Jih, K.Y., and T.C. Hwang. 2012. Nonequilibrium gating of CFTR on an equilibrium theme. *Physiology*. 27:351-361.

Jih, K.Y., W.Y. Lin, Y. Sohma, and T.C. Hwang. 2017. CFTR potentiators: from bench to bedside. *Curr Opin Pharmacol*. 34:98-104.

Jih, K.Y., Y. Sohma, and T.C. Hwang. 2012. Nonintegral stoichiometry in CFTR gating revealed by a pore-lining mutation. *The Journal of general physiology*. 140:347-359.

Kathawala, R.J., P. Gupta, C.R. Ashby, Jr., and Z.S. Chen. 2015. The modulation of ABC transporter-mediated multidrug resistance in cancer: a review of the past decade. *Drug Resist Updat*. 18:1-17.

Lewis, H.A., S.G. Buchanan, S.K. Burley, K. Conners, M. Dickey, M. Dorwart, R. Fowler, X. Gao, W.B. Guggino, W.A. Hendrickson, J.F. Hunt, M.C. Kearins, D. Lorimer, P.C. Maloney, K.W. Post, K.R. Rajashankar, M.E. Rutter, J.M. Sauder, S. Shriver, P.H. Thibodeau, P.J. Thomas, M. Zhang, X. Zhao, and S. Emtage. 2004. Structure of nucleotide-binding domain 1 of the cystic fibrosis transmembrane conductance regulator. *EMBO J*. 23:282-293.

Lewis, H.A., X. Zhao, C. Wang, J.M. Sauder, I. Rooney, B.W. Noland, D. Lorimer, M.C. Kearins, K. Conners, B. Condon, P.C. Maloney, W.B. Guggino, J.F. Hunt, and S. Emtage. 2005. Impact of the deltaF508 mutation in first nucleotide-binding domain of human cystic fibrosis transmembrane conductance regulator on domain folding and structure. *The Journal of biological chemistry*. 280:1346-1353.

Linsdell, P. 2016. Anion conductance selectivity mechanism of the CFTR chloride channel. *Biochimica et biophysica acta*. 1858:740-747.

Liu, F., Z. Zhang, L. Csanady, D.C. Gadsby, and J. Chen. 2017. Molecular Structure of the Human CFTR Ion Channel. *Cell*. 169:85-95 e88.

Locher, K.P. 2009. Structure and mechanism of ATP-binding cassette transporters. *Philosophical Transactions of the Royal Society B: Biological Sciences*. 364:239-245.

Loo, T.W., M.C. Bartlett, and D.M. Clarke. 2013. Corrector VX-809 stabilizes the first transmembrane domain of CFTR. *Biochem Pharmacol*. 86:612-619.

Molinski, S.V., T. Gonska, L.J. Huan, B. Baskin, I.A. Janahi, P.N. Ray, and C.E. Bear. 2014. Genetic, cell biological, and clinical interrogation of the CFTR mutation c.3700 A>G (p.Ile1234Val) informs strategies for future medical intervention. *Genetics in medicine : official journal of the American College of Medical Genetics*.

Muanprasat, C., N.D. Sonawane, D. Salinas, A. Taddei, L.J. Galietta, and A.S. Verkman. 2004. Discovery of glycine hydrazide pore-occluding CFTR inhibitors: mechanism, structure-activity analysis, and in vivo efficacy. *The Journal of general physiology*. 124:125-137.

Norimatsu, Y., A. Ivetac, C. Alexander, J. Kirkham, N. O'Donnell, D.C. Dawson, and M.S.P. Sansom. 2012. Cystic Fibrosis Transmembrane Conductance Regulator: A Molecular Model Defines the Architecture of the Anion Conduction Path and Locates a "Bottleneck" in the Pore. *Biochemistry*. 51:2199-2212.

Oldham, M.L., A.L. Davidson, and J. Chen. 2008. Structural insights into ABC transporter mechanism. *Current Opinion in Structural Biology*. 18:726-733.

Pettit, R.S., and C. Fellner. 2014. CFTR Modulators for the Treatment of Cystic Fibrosis. *P & T : a peer-reviewed journal for formulary management*. 39:500-511.

Pezzulo, A.A., X.X. Tang, M.J. Hoegger, M.H. Alaiwa, S. Ramachandran, T.O. Moninger, P.H. Karp, C.L. Wohlford-Lenane, H.P. Haagsman, M. van Eijk, B. Banfi, A.R. Horswill, D.A. Stoltz, P.B. McCray, Jr., M.J. Welsh, and J. Zabner. 2012. Reduced airway surface pH impairs bacterial killing in the porcine cystic fibrosis lung. *Nature*. 487:109-113.

Picciotto, M.R., J.A. Cohn, G. Bertuzzi, P. Greengard, and A.C. Nairn. 1992. Phosphorylation of the cystic fibrosis transmembrane conductance regulator. *The Journal of biological chemistry*. 267:12742-12752.

Qian, F., Y. El Hiani, and P. Linsdell. 2011. Functional arrangement of the 12th transmembrane region in the CFTR chloride channel pore based on functional investigation of a cysteine-less CFTR variant. *Pflugers Archiv : European journal of physiology*. 462:559-571.

Ramsey, B.W., J. Davies, N.G. McElvaney, E. Tullis, S.C. Bell, P. Drevinek, M. Griese, E.F. McKone, C.E. Wainwright, M.W. Konstan, R. Moss, F. Ratjen, I. Sermet-Gaudelus, S.M. Rowe, Q. Dong, S. Rodriguez, K. Yen, C. Ordonez, J.S. Elborn, and V.X.S. Group. 2011. A CFTR potentiator in patients with cystic fibrosis and the G551D mutation. *The New England journal of medicine*. 365:1663-1672.

Rees, D.C., E. Johnson, and O. Lewinson. 2009. ABC transporters: the power to change. *Nature Reviews Molecular Cell Biology*. 10:218-227.

Ren, H.Y., D.E. Grove, O. De La Rosa, S.A. Houck, P. Sopha, F. Van Goor, B.J. Hoffman, and D.M. Cyr. 2013. VX-809 corrects folding defects in cystic fibrosis transmembrane conductance regulator protein through action on membrane-spanning domain 1. *Molecular biology of the cell*. 24:3016-3024.

Riordan, J.R. 2008. CFTR Function and Prospects for Therapy. *Annual Review of Biochemistry*. 77:701-726.

Riordan, J.R., J.M. Rommens, B. Kerem, N. Alon, R. Rozmahel, Z. Grzelczak, J. Zielenski, S. Lok, N. Plavsic, J.L. Chou, and et al. 1989. Identification of the cystic fibrosis gene: cloning and characterization of complementary DNA. *Science*. 245:1066-1073.

Sohma, Y., and T.C. Hwang. 2015. Cystic fibrosis and the CFTR anion channel. *In* Handbook of Ion Channels. Taylor & Francis Group, LLC. Boca Taton. FL. 627.

Sosnay, P.R., K.R. Siklosi, F. Van Goor, K. Kaniecki, H. Yu, N. Sharma, A.S. Ramalho, M.D. Amaral, R. Dorfman, J. Zielenski, D.L. Masica, R. Karchin, L. Millen, P.J. Thomas, G.P. Patrinos, M. Corey, M.H. Lewis, J.M. Rommens, C. Castellani, C.M. Penland, and G.R. Cutting. 2013. Defining the disease liability of variants in the cystic fibrosis transmembrane conductance regulator gene. *Nature genetics*. 45:1160-1167.

Stoltz, D.A., D.K. Meyerholz, and M.J. Welsh. 2015. Origins of cystic fibrosis lung disease. *The New England journal of medicine*. 372:1574-1575.

Tsai, M.F., M. Li, and T.C. Hwang. 2010. Stable ATP binding mediated by a partial

    NBD dimer of the CFTR chloride channel. *The Journal of general physiology*.

    135:399-414.

Tsai, M.F., H. Shimizu, Y. Sohma, M. Li, and T.C. Hwang. 2009. State-dependent

    modulation of CFTR gating by pyrophosphate. *The Journal of general physiology*.

    133:405-419.

Van Goor, F., S. Hadida, P.D. Grootenhuis, B. Burton, D. Cao, T. Neuberger, A.

    Turnbull, A. Singh, J. Joubran, A. Hazlewood, J. Zhou, J. McCartney, V.

    Arumugam, C. Decker, J. Yang, C. Young, E.R. Olson, J.J. Wine, R.A. Frizzell,

    M. Ashlock, and P. Negulescu. 2009. Rescue of CF airway epithelial cell function

    in vitro by a CFTR potentiator, VX-770. *Proceedings of the National Academy of*

    Sciences of the United States of America. 106:18825-18830.

Van Goor, F., S. Hadida, P.D. Grootenhuis, B. Burton, J.H. Stack, K.S. Straley, C.J.

    Decker, M. Miller, J. McCartney, E.R. Olson, J.J. Wine, R.A. Frizzell, M.

    Ashlock, and P.A. Negulescu. 2011. Correction of the F508del-CFTR protein

    processing defect in vitro by the investigational drug VX-809. *Proceedings of the*

    National Academy of Sciences of the United States of America. 108:18843-18848.

Veit, G., R.G. Avramescu, A.N. Chiang, S.A. Houck, Z. Cai, K.W. Peters, J.S. Hong,

    H.B. Pollard, W.B. Guggino, W.E. Balch, W.R. Skach, G.R. Cutting, R.A.

    Frizzell, D.N. Sheppard, D.M. Cyr, E.J. Sorscher, J.L. Brodsky, and G.L. Lukacs.

    2016. From CFTR biology toward combinatorial pharmacotherapy: expanded

classification of cystic fibrosis mutations. *Molecular biology of the cell*. 27:424-433.

Vergani, P., S.W. Lockless, A.C. Nairn, and D.C. Gadsby. 2005. CFTR channel opening by ATP-driven tight dimerization of its nucleotide-binding domains. *Nature*. 433:876-880.

Wang, W., Y. El Hiani, and P. Linsdell. 2011. Alignment of transmembrane regions in the cystic fibrosis transmembrane conductance regulator chloride channel pore. *The Journal of general physiology*. 138:165-178.

Wang, W., Y. El Hiani, H.N. Rubaiy, and P. Linsdell. 2014. Relative contribution of different transmembrane segments to the CFTR chloride channel pore. *Pflugers Archiv : European journal of physiology*. 466:477-490.

Zhang, J., and T.C. Hwang. 2015. The Fifth Transmembrane Segment of Cystic Fibrosis Transmembrane Conductance Regulator Contributes to Its Anion Permeation Pathway. *Biochemistry*. 54:3839-3850.

Zhang, Z., and J. Chen. 2016. Atomic Structure of the Cystic Fibrosis Transmembrane Conductance Regulator. *Cell*. 167:1586-1597 e1589.

Zhang, Z., F. Liu, and J. Chen. 2017. Conformational Changes of CFTR upon Phosphorylation and ATP Binding. *Cell*.

Chapter 2

The fifth transmembrane segment of cystic fibrosis transmembrane conductance regulator contributes to its anion permeation pathway

This chapter has been adapted from my manuscript published in Biochemistry 54(24): 3839-3850. By Jingyao Zhang and Tzyh-Chang Hwang. According to their website: https://pubs.acs.org/page/copyright/learning_module/module.html#, I retain the copyright for this work and am allowed to reuse this work.

2.1. Abstract

Previous studies have identified several transmembrane segments (TMs) including TM1, TM3, TM6, TM9, TM11 and TM12 as pore-lining in cystic fibrosis transmembrane conductance regulator (CFTR), but the role of TM5 in pore construction remains controversial. In the current study, we employed substituted cysteine accessibility methodology (SCAM) to screen the entire TM5 defined by the original topology model and its cytoplasmic extension in a Cysless background. We found six positions (A299, R303, N306, S307, F310 and F311) where engineered cysteines react to intracellular MTSES$^-$. Quantification of the modification rate of engineered cysteines in the presence or absence of ATP suggests that these six residues are accessible in both the open and closed states. Whole-cell experiments with external MTSES$^-$ identified only two positive positions (L323 and A326), resulting in a segment containing 11 consecutive amino acids, where substituted cysteines respond to neither internal nor external MTSES$^-$, a

unique feature not seen previously in CFTR's pore-lining segments. The observation that these positions are inaccessible to channel permeant thiol-specific reagent $[Au(CN)_2]^-$ suggests that this segment of TM5 between F311 and L323 is concealed from the pore by other TMs and/or lipid bilayers. In addition, our data support the idea that the positively charged arginine at position 303 poses a pure electrostatic action in determining the single-channel current amplitude of CFTR and the effect of an open-channel blocker glibencalmide. Collectively, we conclude that the cytoplasmic portion of CFTR's TM5 lines the pore. Our functional data are remarkably consistent with predicted structural arrangements of TM5 in some homology models of CFTR.

2.2. Introduction

Members in the ATP Binding Cassette (ABC) protein superfamily enact the active movement of a broad range of cargos across the cell membrane against their electrochemical gradients through a translocation pathway embedded in their Transmembrane Domains (TMDs); whereas the conformational changes in the TMDs during a transport cycle is fueled by the free energy from ATP hydrolysis in the Nucleotide Binding Domains (NBDs) (Riordan et al., 1989; Dean and Annilo, 2005). However, Cystic Fibrosis Transmembrane conductance Regulator (CFTR), a bona fide member of this superfamily, functions as a tightly regulated anion-selective ion channel, which is found mainly in the apical membrane of a host of epithelial cells (Bear et al., 1992). Dysfunction of CFTR, resulting from loss-of-function mutations of the CFTR

gene, causes the lethal recessively inherited disease cystic fibrosis (Moskowitz et al., 2008).

In addition to the basic architecture of the two TMD/NBD complexes seen in all ABC proteins, CFTR has a unique disordered Regulatory Domain (RD), whose phosphorylation is a prerequisite for its activity (Gadsby et al., 2006; Chen and Hwang, 2008; Hwang and Sheppard, 2009; Hwang and Kirk, 2013). It is now generally accepted that opening and closing (gating) of phosphorylated CFTR is controlled respectively by the ATP-induced dimerization and hydrolysis-triggered partial separation of CFTR's two NBDs, although how strictly these molecular motions are coupled remains debatable (Jih and Hwang, 2012; Csanady and Torocsik, 2014). Unlike NBDs that are evolutionarily conserved among ABC proteins, little sequence homology in TMDs makes it very difficult to predict their 3-D structure based on homology modeling that utilizes the crystal structures of ABC transporters (Dawson and Locher, 2006, 2007; Ward et al., 2007; Aller et al., 2009; Hohl et al., 2012) as templates. Nonetheless, several CFTR homology models have been developed (Mornon et al., 2008, 2009; Dalton et al., 2012; Norimatsu et al., 2012a; Mornon et al., 2015). It is perhaps not surprising that these structural models of CFTR all exhibit a two-fold symmetry in their TMDs that is observed in the crystal structures of those ABC transporters. Recent studies using substituted cysteine accessibility methodology (SCAM) on CFTR's TMDs indeed support the idea that the aqueous pore is formed by some of the putative 12 transmembrane segments (TMs). These include TM1 (Gao et al., 2013), TM3 (Akabas, 1998), TM6 (Bai et al., 2010; El Hiani and Linsdell, 2010), TM9 (Jordan et al., 2008; Norimatsu et al., 2012a), TM11 (Fatehi and Linsdell, 2009) and TM12 (Bai et al., 2011;

Qian et al., 2011). Furthermore, the reactivity patterns of the engineered cysteines in several TMs corroborate the predicted secondary structure of α-helix for TM1 (Gao et al., 2013), TM3 (Akabas, 1998), TM6 (Bai et al., 2010) and TM12 (Bai et al., 2011). Also interestingly, state-dependent reactivity of the engineered cysteines in TM1, 6, and 12 endorses the "degraded transporter" hypothesis: CFTR evolves from a primordial ABC exporter with its cytoplasmic gate degenerated (ref. Bai et al., 2011, but cf. ref. Wang and Linsdell, 2012a).

Although aforementioned studies suggest a two-fold symmetry in CFTR's TMDs that is in agreement with the prediction based on the degraded transporter hypothesis, a recent paper reported experimental results contradicting this symmetry. First, by cysteine scanning 9 positions in TM7 (F870 to L878) of CFTR's TMD2, Wang et al. (2014) concluded that this TM does not contribute to pore formation despite the fact that the corresponding TM (i.e., TM1) in TMD1 has been shown unequivocally to be part of the pore (Ge et al., 2004; Gao et al., 2013). Second, by scanning 6 positions (F315 – L320) in TM 5 of TMD1 and 7 residues (I1109 to T1115) in its equivalent TM in TMD2 (i.e., TM11), they also concluded that the "central part" of TM11 but not of TM5 lines the pore (Wang et al., 2014). The pore-lining role of TM11 is supported by previous work (Fatehi and Linsdell, 2009), and those SCAM data on TM7 are also consistent with our observations using SCAM to probe a more extended region of TM7 (I860C to V880C) (Figure 2.S1). Moreover, it has been shown that several positively charged residues including K95 in TM1 (Linsdell, 2005; Zhou et al., 2010; Wang and Linsdell, 2012b), R303 in TM5 (Aubin and Linsdell, 2006; Zhou et al., 2007) and R352 in TM6 (Cheung and Akabas, 1997; Guinamard and Akabas, 1999; Aubin and Linsdell, 2006; Cui et al.,

2008; Bai et al., 2010) play critical roles in anion permeation by electrostatically attracting chloride ions to the internal entryway of CFTR's pore. Thus, it seems counter-intuitive that both TM1 and TM6 line the pore, but the R303-containing TM5 does not.

In the present study, we examined the role of TM5 in CFTR's pore construction with SCAM that covers the entire TM5 (S308 - K329) plus its cytoplasmic extension (L295 - S307) in a Cysless background. By applying the negatively charged thiol-specific 2-sulfonatoethyl MTS (MTSES$^-$) from the cytoplasmic side of the membrane, we identified six positive hits, A299C, R303C, N306C, S307C, F310C and F311C. The modification rates are somewhat higher in the absence of ATP than in the presence of ATP for cysteines placed in all these positions, implying that this segment of TM5 is slightly more accessible when the channel is in the closed state. Two MTSES$^-$ reactive positions, C323 and C326, were identified in whole-cell configuration, when the reagent was applied from the extracellular side. The eleven positions between F311 and L323 were all negative to MTSES$^-$ applied from either side of the cell membrane. Cysteines introduced into these 11 positions were also insensitive to the channel-permeant, thiol-reactive [Au(CN)$_2$]$^-$ applied from intracellular side, suggesting that these 11 residues long enough to span at least 3 helical turns are not exposed to the aqueous pathway. We therefore conclude that TM5 does contribute to CFTR's pore in a way that distinguishes itself from other TMs. Our results will be discussed in the context of several homology models of CFTR.

2.3.Materials and Methods

Mutagenesis, cell culture, and transient expression

All experiments were performed in a Cysless CFTR construct reported previously (Bai et al., 2010). Cysteine, one at a time, was then engineered into each position in originally defined TM5 (S308 - K329) and its cytoplasmic extension (L295 - S307) using the QuikChange XL kit (Agilent Technologies). All mutations were confirmed by DNA sequencing (DNA core; University of Missouri).

Before transfection, the Chinese hamster ovary (CHO) cells were grown at 37°C in Dulbecco's modified Eagle's medium containing 10% fetal bovine serum. Together with peGFP-C3 (Takara Bio Inc.) encoding green fluorescent protein, the cDNA constructs of CFTR were cotransfected into CHO cells, using PolyFect transfection reagent (QIAGEN) according to the manufacturer's instructions. The transfected cells were transferred onto sterile glass chips in 35-mm tissue culture dishes and incubated at 27°C for 2 - 7d before electrophysiological experiments were performed. The majority of our experiments require recordings of macroscopic CFTR currents. However, some mutations such as G314C display trafficking defects that prohibit an efficient membrane expression. We thus routinely incubated transfected cells at 27°C for 2 - 7d in order for CFTR channels to effectively traffic to the plasma membrane before electrophysiological experiments were performed. The majority of the CFTR constructs used in the current study generated macroscopic CFTR chloride currents.

Electrophysiology

31

For experiments in excised inside-out patches, micropipettes made of borosilicate capillary glass were pulled with a two-stage vertical puller (Narishige) and then fire-polished with a homemade microforge to reach a pipette resistance of 2–5 MΩ when filled with pipette solution containing (in mM): 140 NMDG-Cl, 2 $MgCl_2$, 5 $CaCl_2$, and 10 HEPES, adjusted to pH 7.4 with NMDG. Glass chips with transfected cells grown on were placed into a chamber on the stage of an inverted microscope (Olympus) and continuously perfused with a bath solution containing (in mM): 145 NaCl, 5 KCl, 2 $MgCl_2$, 1 $CaCl_2$, 5 glucose, 5 HEPES, and 20 sucrose, adjusted to pH 7.4 with NaOH. Immediately after patches with seal resistances > 40 GΩ were excised, the perfusion solution was switched to a standard perfusate containing (in mM): 150 NMDG-Cl, 10 EGTA, 10 HEPES, 8 Tris, and 2 $MgCl_2$, adjusted to pH 7.4 with NMDG. Experiments were conducted at room temperature (22 – 24°C). Current signals at -50 mV holding potential (unless specified otherwise) were acquired with a patch-clamp amplifier (EPC9; HEKA), filtered at 100 Hz digitized online at 500 Hz with Pulse software (V8.53; HEKA), and captured onto a hard disk. Fast solution exchange was achieved with a commercial solution exchange system (SF-77B Perfusion Fast - Step; Warner Instruments).

Micropipettes used in whole-cell experiments were made as described above to yield a resistance of 1.5 – 2.5 MΩ when filled with whole-cell pipette solution containing (in mM): 10 EGTA, 10 HEPES, 20 TEACl, 10 MgATP, 2 $MgCl_2$, 85 aspartate, 16 pyruvate, 5.8 glucose, with pH adjusted to 7.4 using CsOH. During whole-cell experiments, cells were perfused with the same bath solution as the one used for inside-out recordings before patch excision. Experiments were conducted at room temperature

(22 – 24°C). Whole-cell currents were recorded with a 200-ms voltage ramp of ± 100 mV applied every 5 s. The signals were acquired with a patch-clamp amplifier (EPC9; HEKA), filtered at 1 kHz with an eight-pole Bessel filter (LPF-8, Warner Instruments), digitized online at 2 kHz with Pulse software (V8.53; HEKA), and captured onto a hard disk.

Reagents and Cysteine modification

MTS reagents (MTSES$^-$, MTSET$^+$, and MTSEA$^+$; Toronto Research Chemicals Inc.) were prepared as 100 mM stock solutions in ddH$_2$O and stored at -70°C. A single aliquot of the stock solution was thawed immediately before use and diluted into the perfusion solution with or without 2 mM ATP (Sigma-Aldrich) to test the modification on cysteines in the presence of ATP (Figure 2.1) or in the absence of ATP (Figure 2.4), for experiments in inside-out patches. In whole-cell configuration, the stock was thawed and diluted into the bath solution containing 10 µM Forskolin (Figure 2.2). K[Au(CN)$_2$] (Sigma-Aldrich) was prepared as 10 mM stock solutions and stored at 4 °C in a dry and sealed dark box to avoid degradation. During the experiment, K[Au(CN)$_2$] was protected from light by wrapping the perfusion tubes with aluminum foil. PP$_i$ and Glibenclamide were purchased from Sigma-Aldrich Co. LLC.. GlyH-101 was provided by the Chemical Compound Distribution Program sponsored by the Cystic Fibrosis Foundation Therapeutics.

To measure the modification rate of MTSES$^-$ in the absence of ATP, we first applied 32 IU/mL PKA (Sigma-Aldrich) and 2 mM ATP to fully phosphorylate CFTR. Phosphorylated CFTR channels were subsequently opened with ATP for 3 s followed by

a 13-s washout to determine the control peak mean current. The channels were then opened with ATP for 3 s followed by an 8-s washout; in the absence of ATP, MTSES$^-$ was applied for 3 s followed by a 2-s washout. This process was repeated for 12 times or 24 times depending on the time required for modification to complete. The peak mean current amplitudes were plotted against cumulative application times of MTSES$^-$. This relationship was fitted with a single exponential function to obtain the modification rate of MTSES$^-$ in the absence of ATP. To prevent the thiol-group of engineered cysteine from spontaneous oxidation, (Li et al., 2005; Liu et al., 2006), we routinely added 2.67 mM dithiothreitol (DTT; Sigma-Aldrich) into the perfusion solution containing 32 IU/mL PKA and 2 mM ATP in the inside-out experiments, and 5 mM DTT to the bath solution containing forskolin in the whole-cell configuration.

Data analysis

The single-channel current amplitude was estimated by Gaussian fitting of the all-point amplitude histogram with the multi-peak fitting package in the Igor Pro program (WaveMetrics). For the modification of MTSES$^-$, the apparent second-order reaction rate constant was calculated as $1/(\tau \times [\text{MTSES}^-])$, where τ was measured by fitting the current decay phase upon the addition of MTSES$^-$ with a single-exponential function and [MTSES$^-$] represents the working concentration of MTSES$^-$. All results were presented as mean $\pm$ SEM; n: the number of experiments. Student's unpaired t test (two-tailed) was performed with Minitab16.2. $P < 0.05$ was considered significant. Figures of homology models were prepared with PyMOL (V1.3; Schrödinger).

Abbreviations used in this chapter

ABC, ATP-binding cassette; CFTR, Cystic Fibrosis Transmembrane conductance Regulator; NBD, nucleotide binding domain; TMD, transmembrane domain; TM, transmembrane segment; SCAM, substituted cysteine accessibility methodology; RD, Regulatory Domain; MTS, methanethiosulfonate; MTSES⁻, 2-sulfonatoethyl MTS; MTSET⁺, 2-trimethylaminoethyl MTS; MTSEA⁺, 2-aminoethyl MTS hydrochloride; DTT, dithiothreitol; WT, wildtype; $Pt[NO_2]_4^{2-}$, tetranitroplatinate; PPi, pyrophosphate; Glib, glibenclamide.

2.4. Results

Reactivity of substituted cysteines in TM5 to both intracellular and extracellular MTSES⁻

To investigate the role of TM5 in CFTR's pore construction, we introduced cysteines, one at a time, into the originally defined TM5 (residues 308 – 329) (Riordan et al., 1989) and its cytoplasmic extension (295 - 307) in a Cysless background as described previously (Bai et al., 2010, 2011; Gao et al., 2013). Each construct was then studied by assessing the reactivity of the substituted cysteines toward intracellularly applied, negatively charged MTSES⁻. After inside-out patches containing cysteine-substituted channels were fully activated with 32 IU/mL PKA and 2 mM ATP, 1 mM MTSES⁻ was applied in the presence of ATP for at least 1 min. We then switched the perfusion solution back to one with ATP alone to ensure that the current response is due to a covalent modification of the engineered cysteine by MTSES⁻ and hence is not reversed by a simple removal of the reagent. In a representative recording of R303C-CFTR

(Figure 2.1A), the comparison of the mean current before and after the MTSES⁻ treatment shows an irreversible decrease of the mean current by ~87%. In contrast, Figure 2.1B shows an experiment where MTSES⁻ does not affect the ATP-dependent current of Y304C-CFTR channels. Although we cannot rule out the possibility that the cysteine at position 304 was actually modified but without noticeable effects, the simplest explanation for this negative result is that the side-chain of cysteine at this position is not exposed to the aqueous environment so as not to be modified by MTSES⁻.

As seen in the summarized results (Figure 2.1C), 6 cysteine-substituted CFTR channels, including A299C, R303C, N306C, S307C, F310C and F311C, responded to cytoplasmic application of MTSES⁻. The apparent periodicity of these six reactive positions on TM5 suggests that the innermost part of TM5 and its cytoplasmic extension assumes a secondary structure of α-helix as proposed previously (McCarty, 2000). Similar inference of an α-helical structure was made for other TMs (e.g., TM1, TM3, TM6, and TM12). Consistent with our previous SCAM studies on TM1, TM6 and TM12 (Bai et al., 2010, 2011; Gao et al., 2013), there is a clear accessibility limit in TM5 (position 311), beyond which cytoplasmic application of MTSES⁻ fails to modify the engineered cysteine.
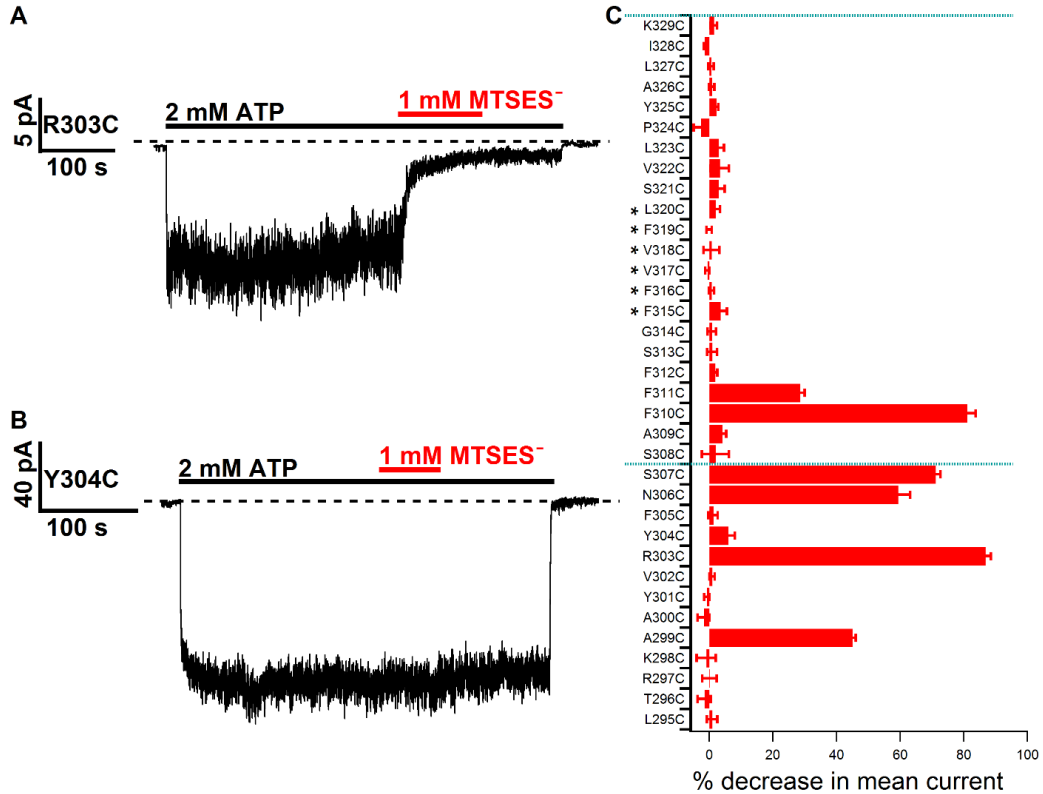
Figure 2.1. Cysteine scanning of TM5 in CFTR with intracellularly applied MTSES⁻. A. A representative current trace recorded at -50 mV in an inside-out membrane patch containing R303C-CFTR channels. Dashed line represents baseline. Application of a saturating concentration of ATP elicited chloride currents (downward deflections). The ATP-induced CFTR current was reduced by intracellular MTSES⁻ treatment. The decrease of current was not restored by the removal of MTSES⁻ indicating that the current decrease was likely due to a covalent modification of C303 by MTSES⁻. **B.** A representative recording of Y304C-CFTR channels using a similar experimental protocol as shown in A. The ATP-induced current was not altered upon intracellular MTSES⁻ treatment suggesting that the cysteine placed at position 304 is not accessible to intracellular MTSES⁻. **C.** Summary of percent decrease in macroscopic mean currents after intracellular application of MTSES⁻ for each cysteine-substituted channels (from cytoplasmic side L295C to extracellular side K329C). Stars mark the positions selected for SCAM studies in Wang et al. (2014)(Wang et al., 2014). The dotted lines mark the membrane boundaries depicted in the originally defined CFTR topology. n = 3 – 9. Data points in this and all subsequent figures are presented as mean ± SEM.

We next employed whole-cell patch-clamp techniques and applied MTSES$^-$ from the extracellular side of the membrane to identify positions that are accessible from the external end of the channel. Although R303C-, N306C- and F310C-CFTR can be readily modified by internal MTSES$^-$, external MTSES$^-$ failed to alter whole-cell currents from either of these three constructs (data not shown). Surprisingly, after testing 15 cysteine-substituted constructs (positions 315 - 329), we only identified two positive hits (residues 323 and 326). Figure 2.2A and 2.2B demonstrate representative whole-cell forskolin-activated CFTR currents in response to extracellular applications of MTSES$^-$: while 1 mM MTSES$^-$ has little effect on F316C-CFTR, it decreased A326C-CFTR currents by ~50%. GlyH-101, a CFTR inhibitor (Norimatsu et al., 2012b; Melis et al., 2014), was applied at the end of the experiments to ensure any currents remained after the application of MTSES$^-$ are indeed from CFTR. Figure 2.2C summarizes these whole-cell experiments with external applications of MTSES$^-$.
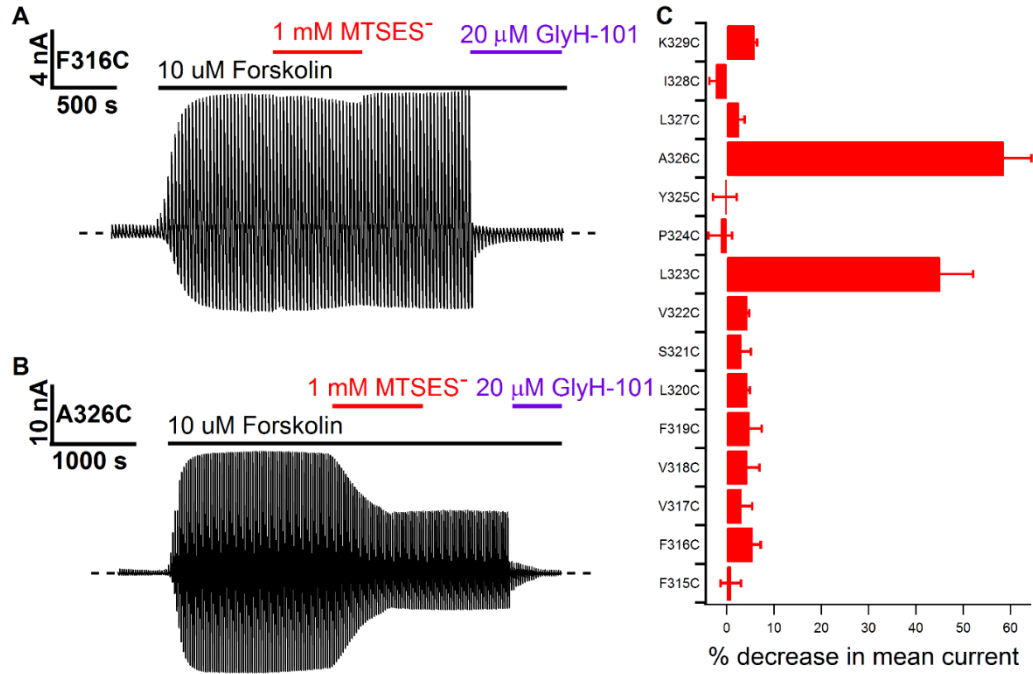
Figure 2.2. Cysteine scanning of CFTR TM5 with extracellularly applied MTSES⁻ in the whole-cell configuration. A. A representative recording of whole-cell currents from F316C-CFTR channels. Dashed line represents the zero current level. A voltage ramp ranging from -100 mV to 100 mV was applied every 5 s. After the currents were fully activated by forskolin, 1 mM MTSES⁻ was applied extracellularly for several minutes until a steady state is reached. MTSES⁻ was subsequently washed out. The final baseline conductance was obtained with 20 µM CFTR blocker GlyH101 to abolish all residual CFTR currents. **B.** A representative recording of whole-cell patch currents of A326C-CFTR channels using a similar protocol as described in A. The CFTR current induced by forskolin decreased upon the application of extracellular MTSES⁻. **C.** Summary of the percentage decrease in macroscopic mean currents after the extracellular application of MTSES⁻ for each cysteine-substituted channel (from cytoplasmic side F315C to extracellular side K329C). n = 3 − 4.

Reactivity of substituted cysteines in TM5 to intracellular [Au(CN)$_2$]$^-$

The results summarized in Figure 2.1C and 2.2C reveal a pattern very different from what we have reported for TM1, TM6 and TM12 (Bai et al., 2010, 2011; Gao et al., 2013). First, previously identified internal accessibility limits reside relatively close to the middle section of the characterized TMs (e.g., L102 in TM1, S341 in TM6, and M1140 in TM12), whereas F311 in TM5 is located close to the cytoplasmic end. Second, the narrow region of the pore, defined as the segment of TMs between internal and external accessibility limits, spans approximately two or three amino acids in length in TM1 and TM6 (i.e., L102 − I106 in TM1 and S341 − T338 in TM6), but cysteines placed at 11 positions between the internally accessible F311 and the externally accessible L323 do not react to either internal or external MTSES$^-$. One possible interpretation of these surprising observations is that this long stretch of TM5 is buried in the protein core and therefore does not line the pore. However, before this conclusion is made, we considered another possibility: some of these 11 amino acids may line the pore but are not accessible because of the bulkiness of MTSES$^-$.

To exclude this possibility, we employed a channel-permeant thiol-specific reagent [Au(CN)$_2$]$^-$ to test if cysteines placed in any of these positions may react with internally applied [Au(CN)$_2$]$^-$. We reasoned that if some of these positions indeed line the narrow part of the anion permeation pathway, introducing a negatively charged adduct with [Au(CN)$_2$]$^-$ should decrease the current. Figure 2.3A and 2.3B show representative results for two different constructs, F315C and R303C. In an inside-out patch (Figure 2.3A), application of 100 µM [Au(CN)$_2$]$^-$ after F315C-CFTR channels were opened by ATP caused a decrease of the current, but the current recovered completely once [Au(CN)$_2$]$^-$

was removed, indicating a reversible blockade of the channel by $[Au(CN)_2]^-$ as reported before (Serrano et al., 2006). In contrast, a similar experimental protocol resulted in a significant decrease of the R303C-CFTR current and a simple washout of $[Au(CN)_2]^-$ did not restore the current amplitude (Figure 2.3B); however, a complete recovery was seen upon the addition of 5 mM dithiothreitol (DTT), a commonly used reducing reagent. Figure 2.3C summarizes all the results on these 11 positions plus positions 303 and 310 as positive controls. We thus conclude that these 11 amino acids do not play a role in constructing the pore-lining segment of CFTR.
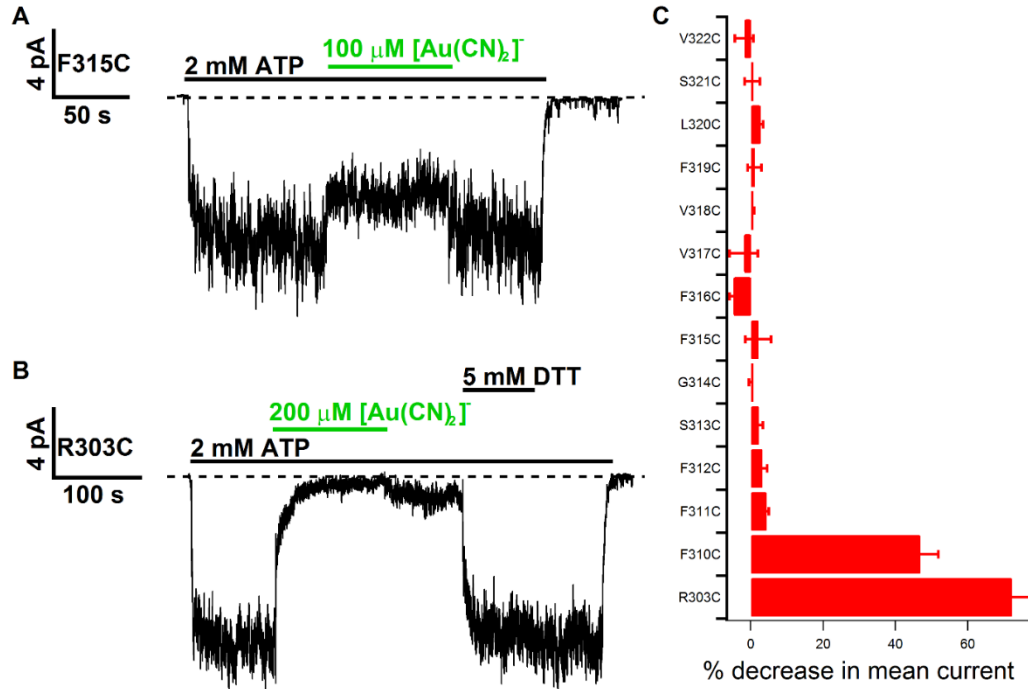
Figure 2.3. Effects of channel-permeant thiol-specific reagent [Au(CN)$_2$]$^-$ on cysteines introduced into TM5. A. A continuous current trace recorded from an inside-out membrane patch containing F315C-CFTR channels. Dashed line represents the baseline current level. Application of a saturating concentration of ATP elicited chloride currents following activation of the channels by 32 IU/mL PKA and ATP (not shown). The ATP-induced current is decreased upon the addition of intracellular [Au(CN)$_2$]$^-$, but the current completely recovered after the removal of [Au(CN)$_2$]$^-$. **B.** A representative current recording of R303C-CFTR channels under a similar experimental protocol as shown in A. The current decrease upon intracellular [Au(CN)$_2$]$^-$ treatment was not restored upon the removal of [Au(CN)$_2$]$^-$. However, the application of DTT recovered all the current, indicating that the current decrease was due to covalent modification by [Au(CN)$_2$]$^-$. **C.** Summary of the percentage decrease in macroscopic mean currents after intracellular application of [Au(CN)$_2$]$^-$ for each cysteine-substituted channel (from cytoplasmic side F311C to extracellular side V322C together with F310C and R303C as positive control). n = 3 – 5.

State dependent modification of engineered cysteines in TM5 by MTSES⁻

To further characterize those 6 positive positions identified by internal applications of MTSES⁻, we compared the modification rates measured in the presence or absence of ATP (see Materials and Methods for details). Figure 2.4A shows a representative experiment where the modification rate in the absence of ATP was obtained for N306C-CFTR. After the channels were fully activated with PKA and ATP, ATP was applied for 3 s followed by an 8-s washout. As seen in Figure 2.4A, the first two applications of ATP elicited similar macroscopic current amplitudes. However, the currents induced by subsequent pulses of ATP show a gradual reduction as MTSES⁻ was added in the washout solutions. Fitting the relationship between the relative current amplitude and cumulative washout time with a single exponential function yields a time constant for calculating the modification rate of N306C in the absence of ATP.

Figure 2.4B summarizes our results. All 6 positions are accessible to internal applications of MTSES⁻ regardless of whether the reagent is applied in the presence or absence of ATP. More interestingly, the modification rates in the absence of ATP are 2~4 folds higher than that in the presence of ATP in all 6 positions (Figure 2.4B), suggesting that these cysteines are accessible to cytoplasmic MTSES⁻ in both open and closed states. Indeed, as seen in Figure 2.S2, N306C-CFTR can be modified when the channel is locked open by PP$_i$. These results also suggest that the inner vestibule of CFTR's pore, where these 6 residues reside in, is more accessible in the closed state, a proposition consistent with previous work that shows a wider internal pore entrance in the closed state (Bai et al., 2011).
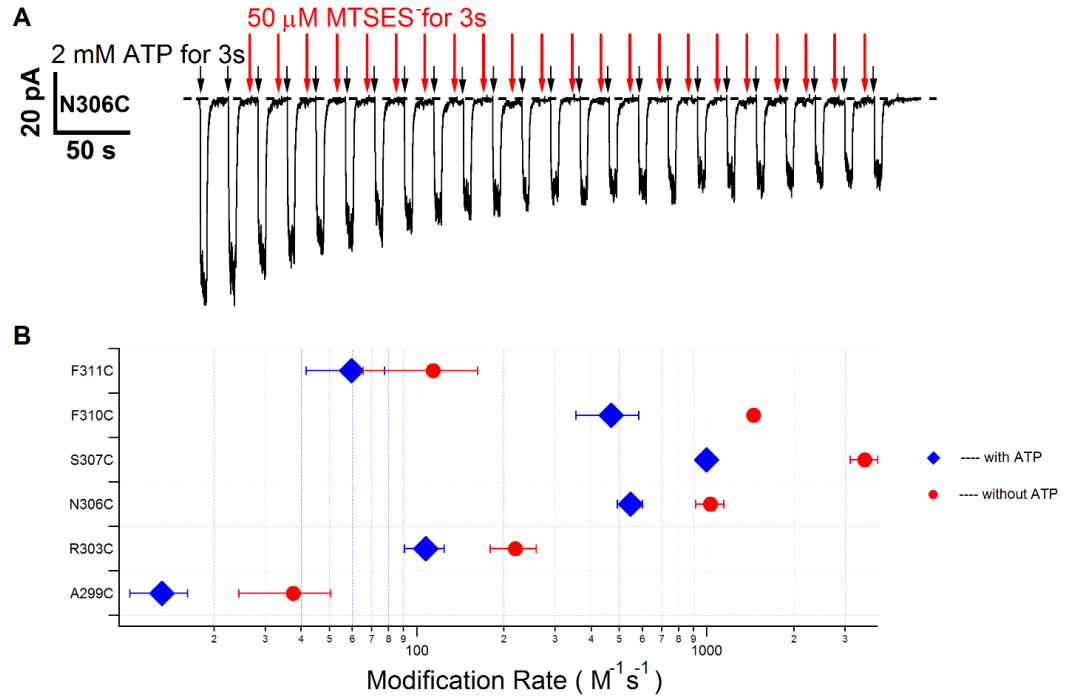
Figure 2.4. Quantitative assessments of modification rates by intracellular MTSES⁻ in the absence and presence of ATP. A. A representative result showing how the modification rate for intracellular MTSES⁻ in the absence of ATP was estimated (see Materials and Methods, and Results for details). Dashed line represents the baseline current level. **B.** A summary of MTSES⁻ modification rates in the absence and presence of ATP at all six positive positions. n = 3 − 9.

Effects of charge replacement in the inner vestibule

So far, the results shown above with macroscopic recordings allow us to identify overall 8 positions (out of 35 scanned) at which engineered cysteines react with internal or external MTSES$^-$. Two possibilities lie behind the macroscopic mean current decrease caused by MTSES$^-$ modification. One is that the introduced adduct following MTSES$^-$ modification changes the single-channel current amplitude through either physically blocking the permeation pathway or electrostatically repulsing the passing chloride ions; the other possibility is that the MTSES$^-$ modification changes CFTR gating and hence reduces the open probability. Considering seriously this latter possibility is important in the current study for the following reasons: First, our previous reports have shown clear gating effects by chemical modification of cysteine-substituted CFTR (Bai et al., 2010; Gao et al., 2013). Second, unlike what has been observed for TM1 and TM6, the single-channel current amplitude remains very constant in all cysteine-substituted CFTR mutants studied in the current report with the only exception of R303C-CFTR (Figure 2.5).
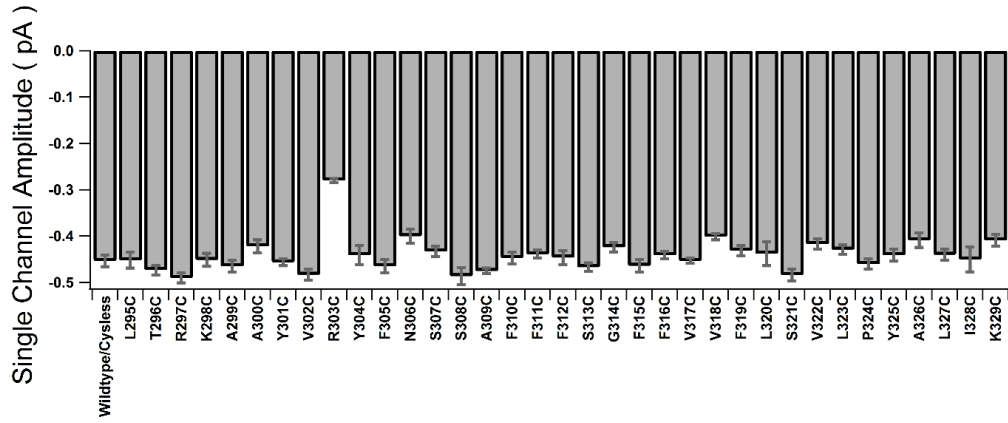
Figure 2.5. Summary of the single-channel current amplitude for WT/Cysless and all cysteine-substituted channels. The transmembrane voltage was clamped at -50 mV. The data are shown as mean ± SEM (n = 3 - 18). The only mutant that shows dramatic difference in the single-channel current amplitude is R303C-CFTR.

We therefore examined the effect of MTSES$^-$ modification at the single-channel level. Two representative single-channel recordings and their all-point histograms (Figure 2.6A) show that before the application of MTSES$^-$, the single-channel current amplitudes of both F310C- and A299C-CFTR (-0.45 ± 0.01 pA, n = 10, and -0.49 ± 0.02 pA, n = 9) are very close to that of WT/Cysless (-0.45 ± 0.01 pA, n = 5), but the single-channel current amplitudes were dramatically decreased after the treatment of MTSES$^-$. Similar reductions of the single-channel current amplitude caused by MTSES$^-$ treatment were also observed at position N306C, S307C and F311C. Figure 2.6B summarizes these microscopic studies on five cysteine-substituted constructs. The percent decrease of the single-channel current amplitude is close to the percent decrease of the macroscopic mean current, suggesting that even taking any possible gating effect of modification into consideration, most of the reduced macroscopic mean current is due to a decrease of the single-channel current amplitude (Figure 2.S3).
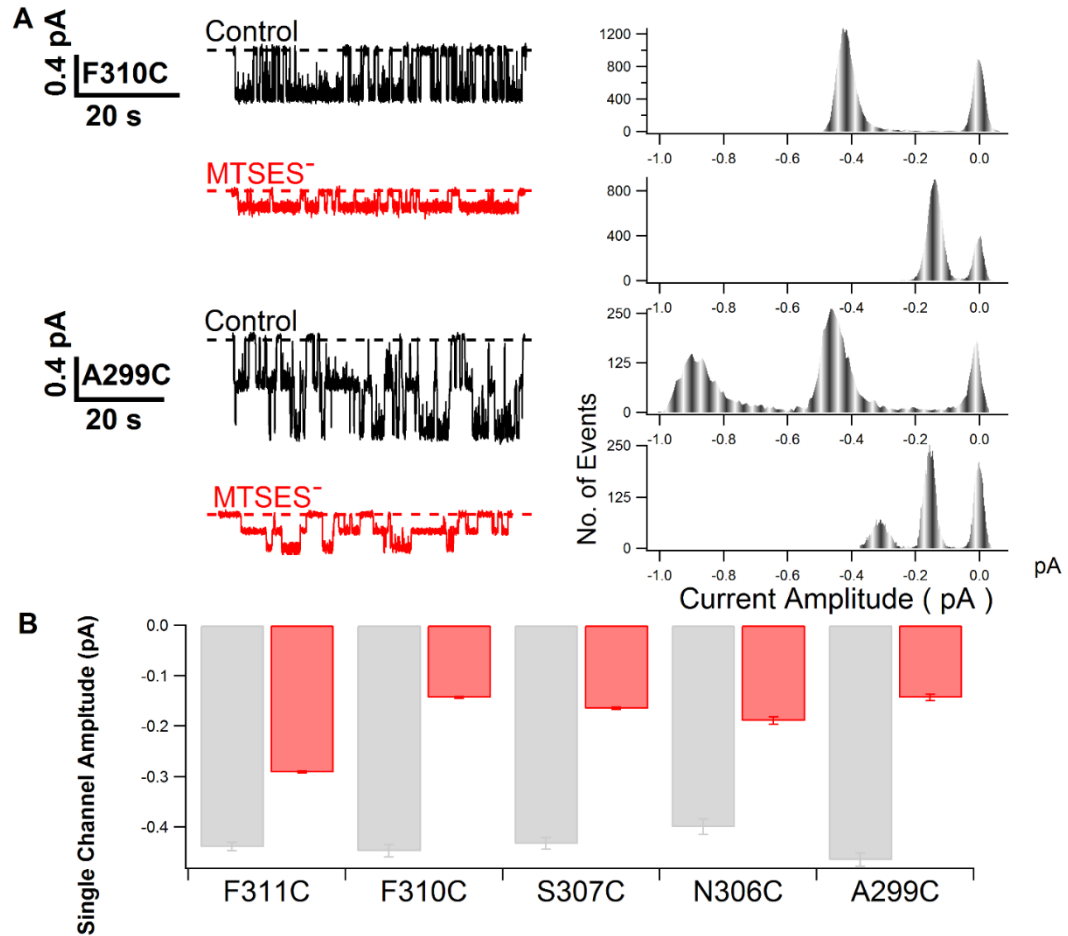
Figure 2.6. Modification by MTSES⁻ reduces the single-channel current amplitude of each reactive mutant. A. Single-channel recordings of F310C-CFTR and A299C-CFTR showing a significant decrease of the single-channel current amplitude after the treatment of MTSES⁻. Dashed line represents the closed-state current level. All-points histograms of the corresponding current traces are presented to show the decrease of single-channel current amplitudes by MTSES⁻. **B.** Summary of changes in the single-channel current amplitude before (gray) and after MTSES⁻ modification (red) at 5 reactive positions (n = 3 – 18). (The single-channel current amplitude of R303C-CFTR after MTSES⁻ modification is too small to be quantified accurately).

For R303C-CFTR, the only mutant with a reduced single-channel current amplitude (-0.28 ± 0.01pA, Figure 2.7A, 2.7C) due to the substitution of a positively charged arginine with a neural cysteine, the modification of negatively charged $MTSES^-$ further decreases the single-channel current amplitude to an unresolvable level (trace not presented). However, positively charged $MTSET^+$ or $MTSEA^+$ increases the single-channel current amplitude of R303C-CFTR to a level virtually identical to that of Cysless channels (Figure 2.7A, 2.7C). Thus, at position 303, a previously proposed pure electrostatic effect on chloride conductance seems at work (Aubin and Linsdell, 2006; Zhou et al., 2007). Furthermore, in the R303C-CFTR background, when we replaced N306, a position approximately one helical turn external to R303, with an arginine, the double mutation N306R/R303C-CFTR shows a higher single-channel current amplitude of (-0.41 ± 0.01 pA, n = 4) than R303C-CFTR (Figure 2.7A, 2.7B and 2.7C), suggesting that moving the positive charge to a presumably neighboring residue can markedly restore the permeation property of the pore. The single-channel current amplitude of N306R/R303C-CFTR was further enhanced by the application of positively charged $MTSET^+$, supporting the idea that positively charged side-chains at this region likely exerts a favorable electrostatic attraction for permeating anions. The effect of charge replacement on the single-channel current amplitude of R303C-CFTR is summarized in Figure 2.7C.

The observation that CFTR's internal vestibule can accommodate multiple positively charged side-chains (Figure 2.7 above, and also see Zhou et al., 2010) suggests that this part of the pore is fairly wide. This idea of a large internal vestibule in CFTR's anion permeation pathway is also supported by the observations that CFTR's pore can be

blocked from the cytoplasmic side of the membrane by the large glibenclamide molecule (MW 494 g/mol) (Schultz et al., 1996; Sheppard and Robinson, 1997; Zhou et al., 2002; Zhang et al., 2004; St Aubin et al., 2007). Several previous studies have also established the critical role of an electropositive internal vestibule of CFTR in attracting anionic blockers such as glibenclamide (Gupta and Linsdell, 2002; Melin et al., 2007; St Aubin et al., 2007; Bai et al., 2010, 2011). This role of positive electropotential in promoting blockade of the pore by the glibenclamide is again demonstrated by our findings that the R303C mutation significantly reduces blockade of the pore by glibenclamide (Figure 2.7D,) and this reduced block can be restored nearly to the full extent by MTSET$^+$ modification on R303C (Figure 2.7D, 2.7E). Collectively, these results of charge replacement experiments also support the notion that this part of TM5 does contribute to the ion permeation pathway.
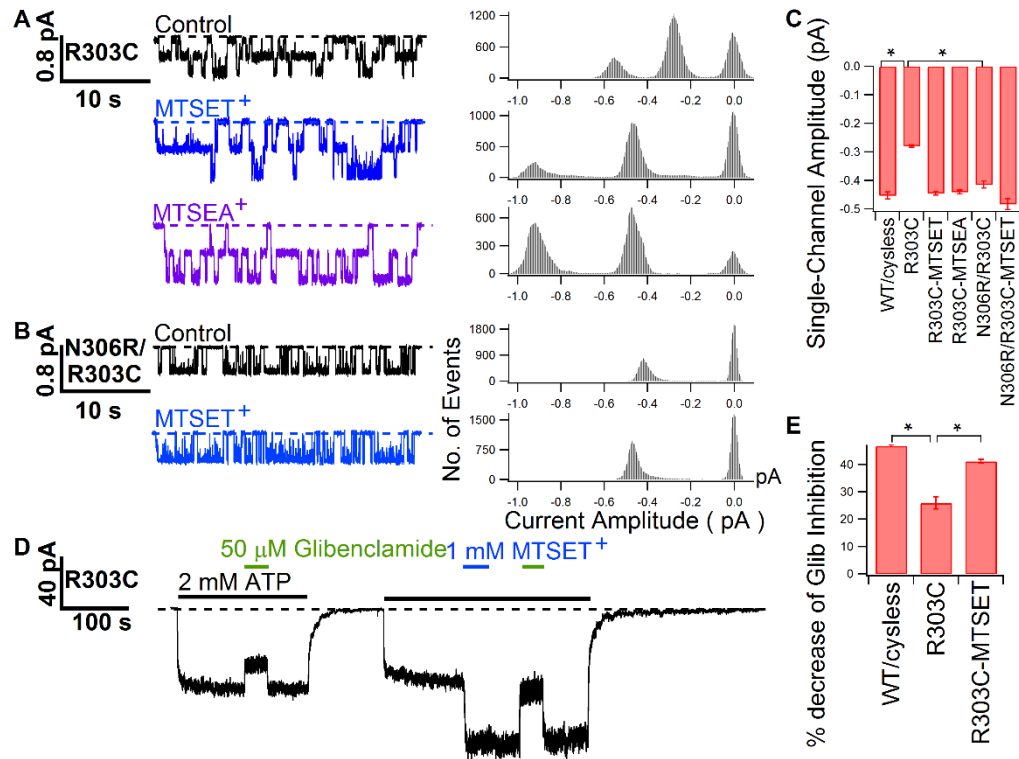
Figure 2.7. Effects of charge replacement at position 303. A. Single-channel recordings demonstrating an increase of the single-channel current amplitude of R303C-CFTR after modification by MTSET$^+$ or MTSEA$^+$. Corresponding all-point histogram is presented to the right of each current trace. **B.** Restoration of the single-channel current amplitude for R303C-CFTR by introducing a positively charged residue at position 306 (i.e., control of N306R/R303C-CFTR), and a further increase of the single-channel current amplitude by MTSET$^+$ modification. All-point histogram for each single-channel trace is also presented. **C.** Summary of the single-channel current amplitudes for R303C-CFTR, N306R/R303C-CFTR and those after modification by positively charged MTS reagents (n = 4 – 11). * marks statistically significant difference (p < 0.05). **D.** A representative macroscopic current recording showing an increase of glibenclamide block after MTSET$^+$ modification on R303C-CFTR. Dashed line represents the closed-state current level. **E.** Summary of glibenclamide block for WT/Cysless-CFTR, R303C-CFTR and MTSET$^+$-modified R303C-CFTR. Glib refers to glibenclamide. * marks statistically significant difference (p < 0.05). n = 4 – 7.

2.5. Discussion

The identification of pore-lining residues and the elucidation of relative motions of each TM during gating transitions are critical in shaping our understanding of the structural and functional properties of the CFTR chloride channel. In the present study, we focused our efforts on characterizing CFTR's TM5 (S308 - K329) and its cytoplasmic extension (L295 - S307) with SCAM. Our investigations identified six positions, i.e., A299, R303, N306, S307, F310 and F311, where the engineered cysteine could be modified by intracellularly applied thiol-specific reagent MTSES$^-$. After MTSES$^-$ modification, the single-channel current amplitude is dramatically reduced as expected for an anion channel pore following the placement of a negatively charged adduct. Furthermore, the apparent periodicity of these six positions suggests that this cytoplasmic portion of TM5 assumes an α-helix secondary structure, an observation similar to our previous reports for TM1, 6, and 12 (Bai et al., 2010, 2011; Gao et al., 2013). Since cysteines introduced at all these positions can be modified both in the presence and in the absence of ATP, we inferred that the side-chains of these six residues are exposed to the aqueous pore in both open and closed states. By comparing the modification rates of MTSES$^-$, we found that all six positions exhibit a higher rate of modification in the absence of ATP than in the presence of ATP (Figure 2.4), suggesting that these residues are more readily accessible when the channel resides in the closed state. If we accept the idea that this segment of TM5 forms part of the internal vestibule of the CFTR pore, this result is not surprising as previous SCAM studies of TM6 and TM12 implicate a widening of CFTR's internal pore entrance when the gate closes (Bai et al., 2010, 2011). Moreover, our data shows that the single-channel current amplitude of N306C can be

reduced by MTSES$^-$ during one locked-opening burst (Figure 2.S2), invalidating the extreme scenario that this cysteine at position 306 can only be modified in the closed state.

Notwithstanding above-mentioned similarities between TM5 and other TMs, the current study reveals an unexpected difference: there exists a segment of consecutive 11 amino acids (F312 - V322), enough to span 3 helical turns, where the engineered cysteine fails to respond to internal or external MTSES$^-$. We also found no evidence of any reactivity for the introduced cysteines at these 11 positions to small channel-permeant, thiol-reactive [Au(CN)$_2$]$^-$. This unique feature distinguishes TM5 from other extensively studied TMs, such as TM1 (Zhou et al., 2010; Gao et al., 2013), TM6 (Bai et al., 2010; Norimatsu et al., 2012a) and TM12 (Bai et al., 2011; Qian et al., 2011; Cui et al., 2012; Norimatsu et al., 2012a), where the accessibility limits to MTSES$^-$ from both sides of membrane are separated only by about 2 - 3 amino acid residues that are thought to form the narrowest region in the CFTR pore (Norimatsu et al., 2012a). Although we cannot completely rule out other possibilities, the simplest explanation for these results is that this segment of TM5 is not exposed to the pore (also see below). Thus, different TMs may assume different structural roles in crafting the pore of CFTR. In fact, the observation that TM1 in CFTR's TMD1, but not its corresponding TM in TMD2 (i.e., TM7), contributes to pore lining indicates a significant asymmetry between TMD1 and TMD2 in the construction of the pore (Wang et al., 2014) (Figure 2.S1).

Despite some earlier reports implicating TM5 as pore-lining (Mansoura et al., 1998; Ge et al., 2004; Aubin and Linsdell, 2006; Zhou et al., 2007; Zhou and Linsdell, 2007), this TM has not been subjected to SCAM studies extensively until recently. Following

cysteine scanning of 6 positions (F315 - L320) in TM5, Wang et al. (2014) concluded that this fraction of TM5 does not play a role in pore construction. By contrast, in the same report, positive positions including I1112, T1115 and S1118 were identified in TM11 (the equivalent TM of TM5 in TMD2), suggesting that TM11 does contribute to pore-lining, a conclusion supported by an earlier report (Fatehi and Linsdell, 2009). Of note, the regions in TM5 and TM11 Wang et al. (2014) chose for their SCAM studies were all located close to the "center" of each TM according to the originally defined topology of CFTR's TMDs (Riordan et al., 1989). That the six positions in TM5 they tested turn out negative is consistent with the current study. However, based on our previous SCAM studies of TM1 (Gao et al., 2013), we have noted that some revisions of the amino-acid assignment for CFTR's TM are necessary. In addition, the helical bundles that form the aqueous pore (or substrate translocation pathway) can easily extend beyond the traditionally defined membrane boundaries (Opella et al., 1999; Hollenstein et al., 2007; Hohl et al., 2012; Kodan et al., 2014). We thus expanded our cysteine scanning to include not only the whole putative TM5 defined by the original topological model (Riordan et al., 1989), but also positions in the originally defined "intracellular loop". Our data suggest that this extended segment may not be a disordered loop, but instead assume a secondary structure and line the internal vestibule of CFTR's pore (also see below).

Among the six residues identified as pore-lining in TM5, the positively charged R303 is perhaps the most interesting one and relatively well studied. It was shown that the substitution of this arginine with glutamic acid results in strong outward rectification while wild-type CFTR shows a linear I-V relationship under a symmetrical chloride

condition (Aubin and Linsdell, 2006). Interestingly, the degree of rectification and the change of the single-channel conductance depend on the charge status at position 303, consistent with the idea that the side-chain of this residue exerts a pure electrostatic effect on chloride permeation through the pore. The same report also shows that a cysteine introduced at position 303 could be modified by either negatively charged MTSES$^-$ or positively charged MTSET$^+$. Indeed, some of these results are confirmed by the current study in a Cysless background (Figure 2.1, 2.3 and 2.7). Further support of the role of R303 in attracting anions comes from experiments using anionic CFTR pore blockers such as suramin, arachidonic acid and tetranitroplatinate (Pt $[NO_2]_4^{2-}$). It was shown that blockade of CFTR by these reagents was significantly reduced by mutations substituting R303 with glutamine or glutamic acid (St Aubin et al., 2007; Zhou et al., 2007; Zhou and Linsdell, 2007). Thus, the importance of the positive charge at position 303 in the internal vestibule of CFTR's pore is beyond question. Here, we demonstrated that the mutation R303C in TM5 reduces glibenclamide block and modification by MTSET$^+$ almost completely restores the inhibition of glibenclamide (Figure 2.7). Taking all the experimental data together, we conclude that R303, as proposed previously (Linsdell, 2005; Aubin and Linsdell, 2006; St Aubin et al., 2007; Zhou et al., 2007; Zhou and Linsdell, 2007), plays an important role in the pore by attracting anions through a simple electrostatic effect. Then, the observation that this electrostatic role of R303 can be assumed by a positive charge introduced external to position 303 (Figure 2.7) constitutes another piece of evidence supporting that TM5 lines part of the CFTR pore. Furthermore, the observation that bearing two positive charges at positions 303 and 306 yields an even higher single-channel current amplitude (Figure 2.7B and 2.7C) supports the idea that this

part of the internal vestibule should be very spacious to avoid creating a strong anion-binding trap.

Although the high-resolution structure of the whole CFTR protein has yet to be resolved, several homology models (Mornon et al., 2008; Alexander et al., 2009; Mornon et al., 2009; Serohijos et al., 2011; Dalton et al., 2012; Norimatsu et al., 2012a; Mornon et al., 2015) have been built based on the crystal structures of ABC exporters (Dawson and Locher, 2006; Ward et al., 2007). We next decided to look into these modeled structures with the hope of gaining some structural insights into our experimental results with TM5. Interestingly, in a latest outward-facing homology model reported by Norimatsu et al. (2012a), the cytoplasmic boundary of TM5 is extended from S308 to A300, which coincides with the cytoplasmic edge in our SCAM study (i.e., A299). However, none of the pore-lining residues identified in the current work are exposed to the anion permeation pathway according to this modeled structure. On the other hand, in another outward-facing homology model meant to simulate CFTR's open state (Dawson and Locher, 2006; Mornon et al., 2008) (Figure 2.8A), we found four out of six positive positions are exposed to the channel pore with the exception of F310 buried in the protein and N306 facing the lipid bilayer. What is perhaps most intriguing to us is that in this modeled structure, the outer portion of TM5 (F312 - K329) is concealed from the pore by resting behind the outer halves of TM6 and TM7 and the lipid bilayer. Of note, an early report by Sheppard et al. (1996) that mutations at position 324 were without effect on the magnitude of cAMP-stimulated CFTR current and the anion selectivity of CFTR is consistent with this picture (Sheppard et al., 1996). Also strikingly, the cytoplasmic end (F312) of this buried segment in TM5 is identical to the internal accessibility limit

identified in the current study (Figure 2.1). Similar consistency between our data and computational predictions is also seen with another channel-like model published more recently (Dalton et al., 2012) (Figure 2.8B).
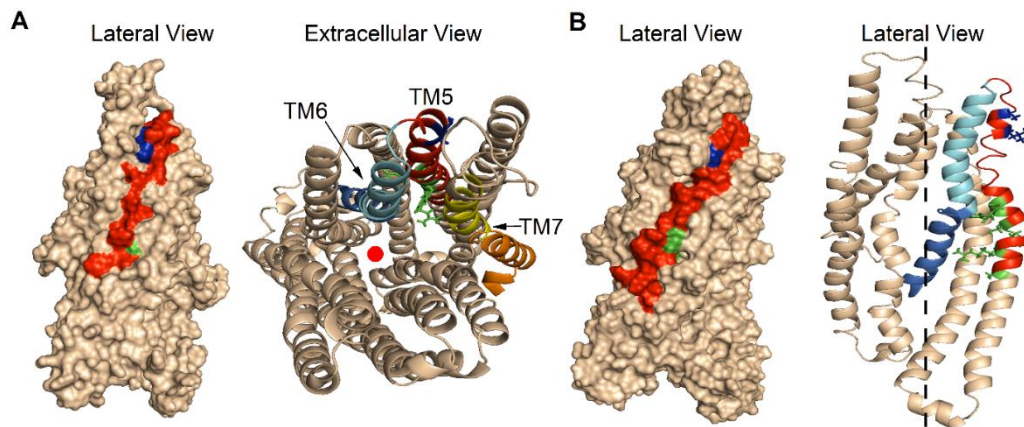
Figure 2.8. Lateral view and extracellular views of two outward-facing structural models of CFTR's TMDs, which represent the presumed open channel conformation. The models were built based on the crystal structure of a bacterial ABC transporter Sav1866. **A.** Lateral view (left) with surface representation and its extracellular view (right) with ribbon representation of the modeled structure in Mornon et al. (2008). The NBD1-RD (370-850) and NBD2-C terminal (1156-1480) are not shown in this this figure. Two TMDs of CFTR were colored in wheat. Of note, the lateral view shows that the major portion of red colored TM5 is located at the periphery of the CFTR protein and hence away from the centrally located pore. Positive hits for intracellular MTSES- are colored in green and two extracellular positive hits, L323 and A326 are colored in blue. It is shown in the extracellular view that, while L323 and A326 are away from the pore axis (red solid circle), four out of six of the intracellular positive hits (green) are pore lining with their side chains exposed to the permeation pathway. F310 is buried in other TMs and N306 is pointing to the lipid phase. Positions external to F312 are hidden behind the outer halves of TM6 (cyan) and TM7 (yellow). The cytoplasmic halves of TM6 (marine) and TM7 (orange) bended away from TM5 so that positions starting from F311 on TM5 are exposed to the pore. **B.** Lateral view (left) of two TMDs of one outward-facing, "channel-like" CFTR homology model and its lateral view (right) of TMD1 with ribbon representation developed by Dalton et al. (2012). TMD2 is removed to better view the relative positions of TM5 and other TMs. Dashed line represents the pore axis. Color codes for all residues are the same as in A. The observations from both views are similar as in **A** despite a significant difference in the arrangement of TMs in these two structures.

While the modeled structures discussed above provide some satisfactory explanations for our data, we were somewhat perplexed by the concealment of N306 and F310 from the pore in these models. As the homology models so far examined all represent "open channel conformations" of CFTR, it remains possible that these two positions may be exposed to the pore in the "closed" state. In the only homology model for CFTR's "closed channel conformation" based on the bacterial ABC lipid flippase, MsbA (Ward et al., 2007; Mornon et al., 2009), we found that all six positive hits identified in our study are well exposed into the aqueous pore and that the same outer segment of TM5 starting at F312 is obstructed by other TMs from the pore (Figure 2.9). Despite this surprisingly satisfying match between the modeled structures and our experimental data, we were not able to explain our SCAM results with L323C and A326C, two constructs responding to external MTSES⁻ (Figure 2.2) as these two positions are part of the outer segment that is protruding to other TMs or membrane lipids. These structural models also fail to provide answers to explain two puzzling results: First, none of the 21 positions tested in TM7 are positive. Second, while F311C reacts to internal MTSES⁻, [Au(CN)$_2$]⁻ has little effect (Figure 2.3). Despite these caveats, these modeled structures of CFTR do support a role of TM5 in CFTR's pore construction, and our studies serve as a reminder that computational and experimental approaches could be fruitfully complementary in our pursuit of a better understanding of the CFTR channel.
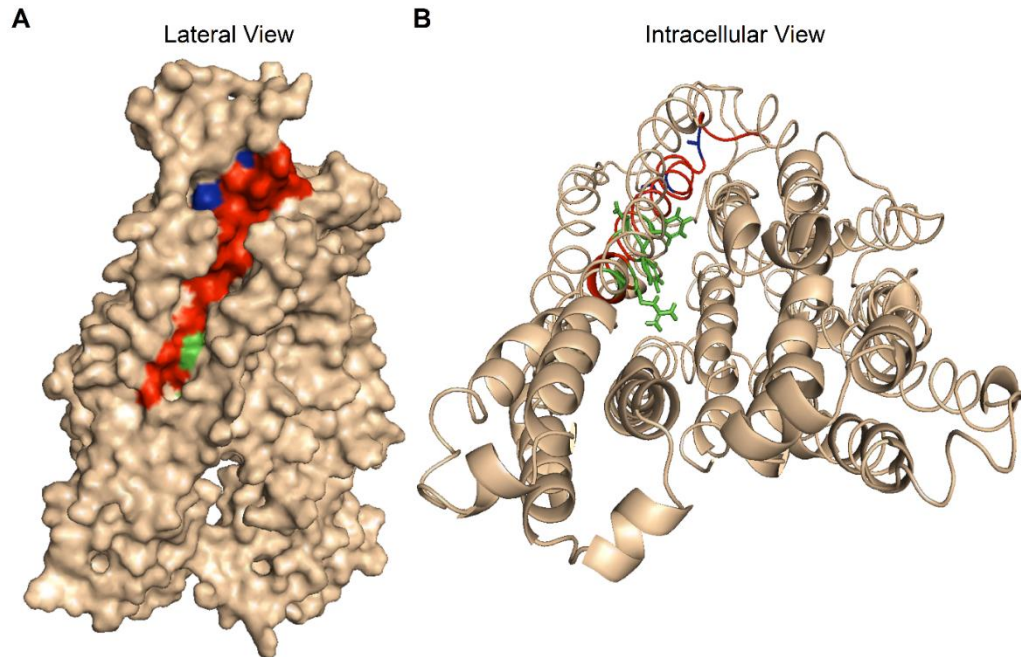
Figure 2.9. Lateral and cytoplasmic views of an inward-facing structural model representing the presumed closed conformation of CFTR. This model in Mornon et al (2009) was based on the crystal structure of a bacterial ABC lipid flippase, MsbA. Color codes are the same as in Figure 2.8. **A.** Lateral view with surface representation shows that the majority of TM5 (red) including two extracellular positive hits, L323 and A326 (blue), is located at the periphery of the CFTR protein. **B.** Intracellular view shows that all 6 positive hits with intracellular MTSES$^-$ are located on one face of TM5 where the side chains are exposed to the aqueous environment of the inner vestibule, whereas positions external to F312 (red and blue) are hidden behind other TMs.

2.6 Supporting Materials
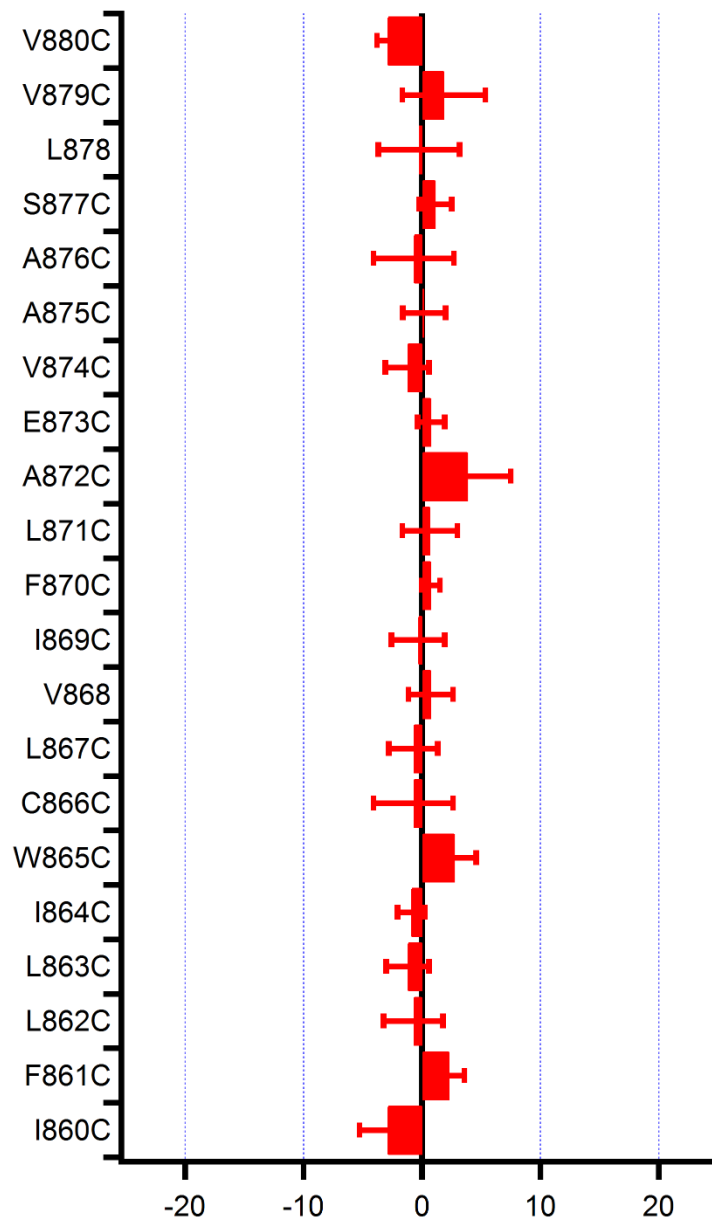
Figure 2.S1. Summary of SCAM results of TM7. All 21 residues are not accessible to intracellularly

applied MTSES$^-$. n = 3 − 7. Data points are presented as mean ± SEM.
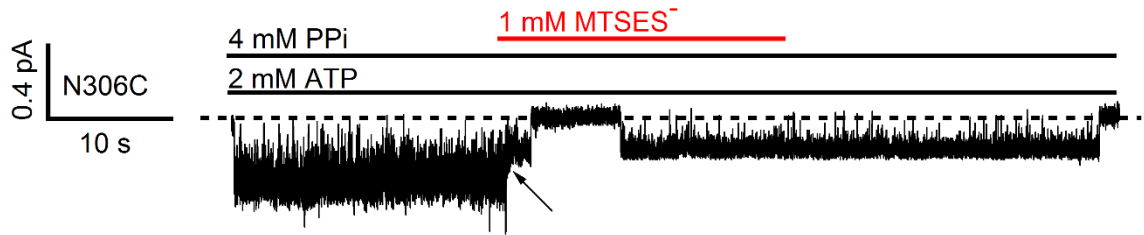
Figure 2.S2. Open state modification of N306C. In a single channel recording where N306C-CFTR was locked open by ATP plus pyrophosphate (PP_i), upon the application of MTSES$^-$, the single-channel amplitude was reduced during one opening burst. Later on, the same channel re-opened with a smaller amplitude. Arrow points to the exact time when the single-channel amplitude is reduced. Similar observations were made in three different patches. These data confirm that cysteine at position 306 can be modified in the open state and ruled out one extreme scenario that N306C can only be modified when channel is in its closed state.
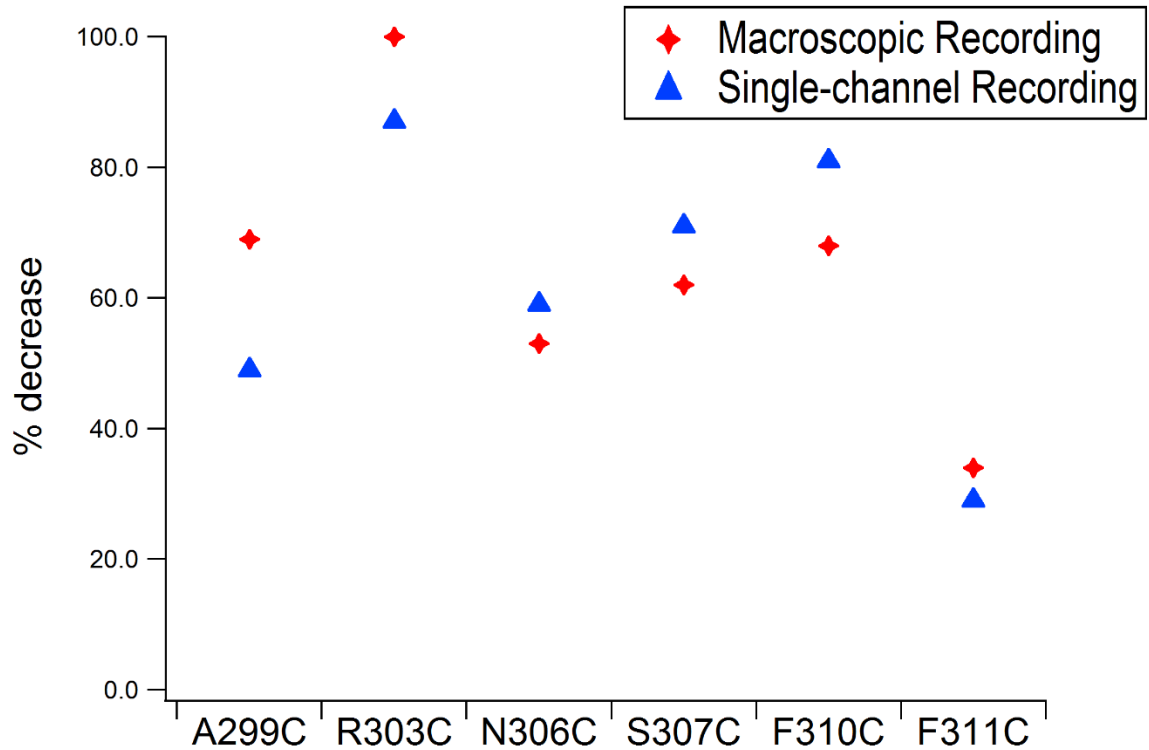
Figure 2.S3. Comparison of percent current decreases between macroscopic recordings (red stars) and single-channel analyses (blue triangles) following MTSES$^-$ modification. These results indicate that most if not all of the effects of MTSES$^-$ modification are due to a reduction of the single-channel amplitude. $n = 3 - 18$ for each data point.

2.7 References

Akabas, M.H. 1998. Channel-lining residues in the M3 membrane-spanning segment of the cystic fibrosis transmembrane conductance regulator. *Biochemistry*. 37:12233-12240.

Alexander, C., A. Ivetac, X. Liu, Y. Norimatsu, J.R. Serrano, A. Landstrom, M. Sansom, and D.C. Dawson. 2009. Cystic Fibrosis Transmembrane Conductance Regulator: Using Differential Reactivity toward Channel-Permeant and Channel-Impermeant Thiol-Reactive Probes To Test a Molecular Model for the Pore. *Biochemistry*. 48:10078-10088.

Aller, S.G., J. Yu, A. Ward, Y. Weng, S. Chittaboina, R. Zhuo, P.M. Harrell, Y.T. Trinh, Q. Zhang, I.L. Urbatsch, and G. Chang. 2009. Structure of P-Glycoprotein Reveals a Molecular Basis for Poly-Specific Drug Binding. *Science*. 323:1718-1722.

Aubin, C.N., and P. Linsdell. 2006. Positive charges at the intracellular mouth of the pore regulate anion conduction in the CFTR chloride channel. *The Journal of general physiology*. 128:535-545.

Bai, Y., M. Li, and T.C. Hwang. 2010. Dual roles of the sixth transmembrane segment of the CFTR chloride channel in gating and permeation. *The Journal of general physiology*. 136:293-309.

Bai, Y., M. Li, and T.C. Hwang. 2011. Structural basis for the channel function of a degraded ABC transporter, CFTR (ABCC7). *The Journal of general physiology*. 138:495-507.

Bear, C.E., C.H. Li, N. Kartner, R.J. Bridges, T.J. Jensen, M. Ramjeesingh, and J.R. Riordan. 1992. Purification and functional reconstitution of the cystic fibrosis transmembrane conductance regulator (CFTR). *Cell*. 68:809-818.

Chen, T.Y., and T.C. Hwang. 2008. CLC-0 and CFTR: Chloride Channels Evolved From Transporters. *Physiological reviews*. 88:351-387.

Cheung, M., and M.H. Akabas. 1997. Locating the anion-selectivity filter of the cystic fibrosis transmembrane conductance regulator (CFTR) chloride channel. *The Journal of general physiology*. 109:289-299.

Csanady, L., and B. Torocsik. 2014. Catalyst-like modulation of transition states for CFTR channel opening and closing: new stimulation strategy exploits nonequilibrium gating. *The Journal of general physiology*. 143:269-287.

Cui, G., B. Song, H.W. Turki, and N.A. McCarty. 2012. Differential contribution of TM6 and TM12 to the pore of CFTR identified by three sulfonylurea-based blockers. *Pflugers Archiv : European journal of physiology*. 463:405-418.

Cui, G., Z.R. Zhang, A.R. O'Brien, B. Song, and N.A. McCarty. 2008. Mutations at arginine 352 alter the pore architecture of CFTR. *The Journal of membrane biology*. 222:91-106.

Dalton, J., O. Kalid, M. Schushan, N. Ben-Tal, and J. Villa-Freixa. 2012. New model of cystic fibrosis transmembrane conductance regulator proposes active channel-like conformation. *Journal of chemical information and modeling*. 52:1842-1853.

Dawson, R.J.P., and K.P. Locher. 2006. Structure of a bacterial multidrug ABC transporter. *Nature*. 443:180-185.

Dawson, R.J.P., and K.P. Locher. 2007. Structure of the multidrug ABC transporter Sav1866 from Staphylococcus aureus in complex with AMP-PNP. *FEBS letters*. 581:935-938.

Dean, M., and T. Annilo. 2005. Evolution of the ATP-binding cassette (ABC) transporter superfamily in vertebrates. *Annual review of genomics and human genetics*. 6:123-142.

El Hiani, Y., and P. Linsdell. 2010. Changes in accessibility of cytoplasmic substances to the pore associated with activation of the cystic fibrosis transmembrane conductance regulator chloride channel. *The Journal of biological chemistry*. 285:32126-32140.

Fatehi, M., and P. Linsdell. 2009. Novel Residues Lining the CFTR Chloride Channel Pore Identified by Functional Modification of Introduced Cysteines. *Journal of Membrane Biology*. 228:151-164.

Gadsby, D.C., P. Vergani, and L. Csanády. 2006. The ABC protein turned chloride channel whose failure causes cystic fibrosis. *Nature*. 440:477-483.

Gao, X., Y. Bai, and T.C. Hwang. 2013. Cysteine scanning of CFTR's first transmembrane segment reveals its plausible roles in gating and permeation. *Biophys J*. 104:786-797.

Ge, N., C.N. Muise, X. Gong, and P. Linsdell. 2004. Direct comparison of the functional roles played by different transmembrane regions in the cystic fibrosis transmembrane conductance regulator chloride channel pore. *The Journal of biological chemistry*. 279:55283-55289.

Guinamard, R., and M.H. Akabas. 1999. Arg352 is a major determinant of charge selectivity in the cystic fibrosis transmembrane conductance regulator chloride channel. *Biochemistry*. 38:5528-5537.

Gupta, J., and P. Linsdell. 2002. Point mutations in the pore region directly or indirectly affect glibenclamide block of the CFTR chloride channel. *Pflugers Archiv : European journal of physiology*. 443:739-747.

Hohl, M., C. Briand, M.G. Grutter, and M.A. Seeger. 2012. Crystal structure of a heterodimeric ABC transporter in its inward-facing conformation. *Nature structural & molecular biology*. 19:395-402.

Hollenstein, K., R.J.P. Dawson, and K.P. Locher. 2007. Structure and mechanism of ABC transporter proteins. *Current Opinion in Structural Biology*. 17:412-418.

Hwang, T.C., and K.L. Kirk. 2013. The CFTR ion channel: gating, regulation, and anion permeation. *Cold Spring Harbor perspectives in medicine*. 3:a009498.

Hwang, T.C., and D.N. Sheppard. 2009. Gating of the CFTR Cl- channel by ATP-driven nucleotide-binding domain dimerisation. *The Journal of physiology*. 587:2151-2161.

Jih, K.Y., and T.C. Hwang. 2012. Nonequilibrium gating of CFTR on an equilibrium
theme. *Physiology*. 27:351-361.

Jordan, I.K., K.C. Kota, G. Cui, C.H. Thompson, and N.A. McCarty. 2008. Evolutionary
and functional divergence between the cystic fibrosis transmembrane conductance
regulator and related ATP-binding cassette transporters. *Proceedings of the
National Academy of Sciences of the United States of America*. 105:18865-18870.

Kodan, A., T. Yamaguchi, T. Nakatsu, K. Sakiyama, C.J. Hipolito, A. Fujioka, R.
Hirokane, K. Ikeguchi, B. Watanabe, J. Hiratake, Y. Kimura, H. Suga, K. Ueda,
and H. Kato. 2014. Structural basis for gating mechanisms of a eukaryotic P-
glycoprotein homolog. *Proceedings of the National Academy of Sciences of the
United States of America*. 111:4049-4054.

Li, Y., W.-P. Yu, C.-W. Lin, and T.-Y. Chen. 2005. Oxidation and Reduction Control of
the Inactivation Gating of Torpedo ClC-0 Chloride Channels. *Biophysical Journal*.
88:3936-3945.

Linsdell, P. 2005. Location of a common inhibitor binding site in the cytoplasmic
vestibule of the cystic fibrosis transmembrane conductance regulator chloride
channel pore. *The Journal of biological chemistry*. 280:8945-8950.

Liu, X., C. Alexander, J. Serrano, E. Borg, and D.C. Dawson. 2006. Variable Reactivity
of an Engineered Cysteine at Position 338 in Cystic Fibrosis Transmembrane
Conductance Regulator Reflects Different Chemical States of the Thiol. *Journal
of Biological Chemistry*. 281:8275-8285.

Mansoura, M.K., S.S. Smith, A.D. Choi, N.W. Richards, T.V. Strong, M.L. Drumm, F.S. Collins, and D.C. Dawson. 1998. Cystic fibrosis transmembrane conductance regulator (CFTR) anion binding as a probe of the pore. *Biophys J*. 74:1320-1332.

McCarty, N.A. 2000. Permeation through the CFTR chloride channel. *The Journal of experimental biology*. 203:1947-1962.

Melin, P., E. Hosy, M. Vivaudou, and F. Becq. 2007. CFTR inhibition by glibenclamide requires a positive charge in cytoplasmic loop three. *Biochimica et biophysica acta*. 1768:2438-2446.

Melis, N., M. Tauc, M. Cougnon, S. Bendahhou, S. Giuliano, I. Rubera, and C. Duranton. 2014. Revisiting CFTR inhibition: a comparative study of CFTRinh -172 and GlyH-101 inhibitors. *British journal of pharmacology*. 171:3716-3727.

Mornon, J.P., B. Hoffmann, S. Jonic, P. Lehn, and I. Callebaut. 2015. Full-open and closed CFTR channels, with lateral tunnels from the cytoplasm and an alternative position of the F508 region, as revealed by molecular dynamics. *Cellular and molecular life sciences : CMLS*. 72:1377-1403.

Mornon, J.P., P. Lehn, and I. Callebaut. 2008. Atomic model of human cystic fibrosis transmembrane conductance regulator: membrane-spanning domains and coupling interfaces. *Cellular and molecular life sciences : CMLS*. 65:2594-2612.

Mornon, J.P., P. Lehn, and I. Callebaut. 2009. Molecular models of the open and closed states of the whole human CFTR protein. *Cellular and molecular life sciences : CMLS*. 66:3469-3486.

Moskowitz, S.M., J.F. Chmiel, D.L. Sternen, E. Cheng, R.L. Gibson, S.G. Marshall, and
G.R. Cutting. 2008. Clinical practice and genetic counseling for cystic fibrosis
and CFTR-related disorders. *Genetics in medicine : official journal of the
American College of Medical Genetics*. 10:851-868.

Norimatsu, Y., A. Ivetac, C. Alexander, J. Kirkham, N. O'Donnell, D.C. Dawson, and
M.S.P. Sansom. 2012a. Cystic Fibrosis Transmembrane Conductance Regulator:
A Molecular Model Defines the Architecture of the Anion Conduction Path and
Locates a "Bottleneck" in the Pore. *Biochemistry*. 51:2199-2212.

Norimatsu, Y., A. Ivetac, C. Alexander, N. O'Donnell, L. Frye, M.S. Sansom, and D.C.
Dawson. 2012b. Locating a plausible binding site for an open-channel blocker,
GlyH-101, in the pore of the cystic fibrosis transmembrane conductance regulator.
Molecular pharmacology. 82:1042-1055.

Opella, S.J., F.M. Marassi, J.J. Gesell, A.P. Valente, Y. Kim, M. Oblatt-Montal, and M.
Montal. 1999. Structures of the M2 channel-lining segments from nicotinic
acetylcholine and NMDA receptors by NMR spectroscopy. *Nature structural
biology*. 6:374-379.

Qian, F., Y. El Hiani, and P. Linsdell. 2011. Functional arrangement of the 12th
transmembrane region in the CFTR chloride channel pore based on functional
investigation of a cysteine-less CFTR variant. *Pflugers Archiv : European journal
of physiology*. 462:559-571.

Riordan, J.R., J.M. Rommens, B. Kerem, N. Alon, R. Rozmahel, Z. Grzelczak, J.
Zielenski, S. Lok, N. Plavsic, J.L. Chou, and et al. 1989. Identification of the

cystic fibrosis gene: cloning and characterization of complementary DNA. *Science*. 245:1066-1073.

Schultz, B.D., A.D. DeRoos, C.J. Venglarik, A.K. Singh, R.A. Frizzell, and R.J. Bridges. 1996. Glibenclamide blockade of CFTR chloride channels. *The American journal of physiology*. 271:L192-200.

Serohijos, A.W., P.H. Thibodeau, and N.V. Dokholyan. 2011. Molecular modeling tools and approaches for CFTR and cystic fibrosis. *Methods in molecular biology*. 741:347-363.

Serrano, J.R., X. Liu, E.R. Borg, C.S. Alexander, C.F. Shaw, and D.C. Dawson. 2006. CFTR: Ligand Exchange between a Permeant Anion ([Au(CN)2]−) and an Engineered Cysteine (T338C) Blocks the Pore. *Biophysical Journal*. 91:1737-1748.

Sheppard, D.N., and K.A. Robinson. 1997. Mechanism of glibenclamide inhibition of cystic fibrosis transmembrane conductance regulator Cl- channels expressed in a murine cell line. *The Journal of physiology*. 503 (Pt 2):333-346.

Sheppard, D.N., S.M. Travis, H. Ishihara, and M.J. Welsh. 1996. Contribution of proline residues in the membrane-spanning domains of cystic fibrosis transmembrane conductance regulator to chloride channel function. *The Journal of biological chemistry*. 271:14995-15001.

St Aubin, C.N., J.J. Zhou, and P. Linsdell. 2007. Identification of a second blocker binding site at the cytoplasmic mouth of the cystic fibrosis transmembrane

conductance regulator chloride channel pore. *Molecular pharmacology*. 71:1360-1368.

Wang, W., Y. El Hiani, H.N. Rubaiy, and P. Linsdell. 2014. Relative contribution of different transmembrane segments to the CFTR chloride channel pore. *Pflugers Archiv : European journal of physiology*. 466:477-490.

Wang, W., and P. Linsdell. 2012a. Alternating Access to the Transmembrane Domain of the ATP-binding Cassette Protein Cystic Fibrosis Transmembrane Conductance Regulator (ABCC7). *Journal of Biological Chemistry*. 287:10156-10165.

Wang, W., and P. Linsdell. 2012b. Conformational change opening the CFTR chloride channel pore coupled to ATP-dependent gating. *Biochimica et biophysica acta*. 1818:851-860.

Ward, A., C.L. Reyes, J. Yu, C.B. Roth, and G. Chang. 2007. Flexibility in the ABC transporter MsbA: Alternating access with a twist. *Proceedings of the National Academy of Sciences*. 104:19005-19010.

Zhang, Z.R., G. Cui, S. Zeltwanger, and N.A. McCarty. 2004. Time-dependent interactions of glibenclamide with CFTR: kinetically complex block of macroscopic currents. *The Journal of membrane biology*. 201:139-155.

Zhou, J.J., M. Fatehi, and P. Linsdell. 2007. Direct and indirect effects of mutations at the outer mouth of the cystic fibrosis transmembrane conductance regulator chloride channel pore. *The Journal of membrane biology*. 216:129-142.

Zhou, J.J., M.S. Li, J. Qi, and P. Linsdell. 2010. Regulation of conductance by the number of fixed positive charges in the intracellular vestibule of the CFTR chloride channel pore. *The Journal of general physiology*. 135:229-245.

Zhou, J.J., and P. Linsdell. 2007. Molecular mechanism of arachidonic acid inhibition of the CFTR chloride channel. *European journal of pharmacology*. 563:88-91.

Zhou, Z., S. Hu, and T.C. Hwang. 2002. Probing an open CFTR pore with organic anion blockers. *The Journal of general physiology*. 120:647-662.

CHAPTER 3

Electrostatic tuning of the pre- and post-hydrolytic open states in CFTR

This chapter has been adapted from my manuscript published in J Gen Physiol 149(3): 355-372. By Jingyao Zhang, J. and Tzyh-Chang Hwang. According to their website: http://www.rupress.org/content/permissions-and-licensing, I retain the copyright for this work and am allowed to reuse this work.

3.1 Abstract

CFTR is an ion channel that couples ATP hydrolysis at its nucleotide binding domains (NBDs) to gating transitions in its transmembrane domains (TMDs). We previously reported that the charge-neutralized mutant, R352C shows two distinct open states, O_1 and O_2. The two states could be distinguished by their single-channel current amplitudes: O_1 having a smaller amplitude (representing a pre-hydrolytic open state) and O_2 having a larger amplitude (representing a post-hydrolytic open state). Here, a similar phenotype is described for two mutations of another pore-lining residue, N306D and N306E, suggesting that alterations of the net charge within CFTR's pore confer this unique conductance aberration. Because moving either of the two endogenous charges R303 and R352 to positions further along TM5 and TM6, respectively, also results in this O_1O_2 phenotype, we conclude that the position of the charged residue in the internal vestibule affects hydrolysis-dependent conductance changes. Furthermore, our data show

that the buffer and CFTR blocker MOPS$^-$ occludes the O_1 state more than it does the O_2 state when the net charge of the internal vestibule is unchanged or increased. In contrast, when the net charge in the internal vestibule is decreased, the differential sensitivity to MOPS$^-$ block is diminished. We propose a three-state blocking mechanism to explain the charge-dependent sensitivity of pre-hydrolytic and post-hydrolytic open states to MOPS$^-$ block. We further posit that the internal vestibule expands during the O_1 to O_2 transition so that mutation-induced electrostatic perturbations within the pore are amplified by the smaller internal vestibule of the O_1 state and thus result in the O_1O_2 phenotype and the charge-dependent sensitivity of the two open states to MOPS$^-$ block. Our study not only relates the O_1O_2 phenotype to the charge distribution in CFTR's internal vestibule, but also provides a toolbox for mechanistic studies of CFTR gating by ATP hydrolysis.

3.2 Introduction

The function of Cystic Fibrosis Transmembrane conductance Regulator (CFTR) as a tightly regulated anion-selective ion channel makes it a unique member of the ATP binding cassette (ABC) protein superfamily, whose members are mostly active transporters carrying a broad range of substrates across the cell membrane against their electrochemical gradients (Davidson and Maloney, 2007; Oldham et al., 2008; Kathawala et al., 2015). The ion translocation pathway, or the pore, of CFTR is proposed to be formed by its two transmembrane domains TMD1 and TMD2 (Hwang and Kirk, 2013), each of which contains six transmembrane segments (TMs), namely TM1 to TM6 and TM7 to TM12, respectively (Riordan et al., 1989; Bear et al., 1992). Opening and closing of the gate in the TMDs are mainly controlled by ATP binding/hydrolysis at CFTR's two

cytosolic nucleotide-binding domains NBD1 and NBD2 (Higgins and Linton, 2004; Vergani et al., 2005; Gadsby et al., 2006; Hwang and Sheppard, 2009; Locher, 2009; Rees et al., 2009). The two sets of TMD-NBD complexes in CFTR are linked by a unique, disordered regulatory domain (RD) (Ostedgaard et al., 2000; Ostedgaard et al., 2001; Bozoky et al., 2013), phosphorylation of which is a prerequisite for CFTR's activity (Chen and Hwang, 2008; Hwang and Sheppard, 2009).

Our understanding of the coupling mechanism between the conformational changes in CFTR's TMDs and those in NBDs is still incomplete, despite decades of biophysical and biochemical studies. It is, however, widely accepted that after phosphorylation of the RD by protein kinase A (PKA), the transition in TMDs from the closed state to the open state is linked to ATP-mediated NBD1/NBD2 dimerization in a head-to-tail configuration (Vergani et al., 2005; Sohma and Hwang, 2015). Two gating models relating the molecular motions of NBDs and TMDs have emerged recently (Csanady et al., 2010; Jih and Hwang, 2012; Jih et al., 2012). The strict coupling gating model dictates that opening of the gate in TMDs is triggered by the dimerization of NBDs; whereas gate closure is associated with hydrolysis-induced partial separation of the NBD dimer (Tsai et al., 2009; Csanady et al., 2010; Tsai et al., 2010), resulting in a one-to-one stoichiometry between the gating cycle and ATP hydrolysis cycle. On the other hand, the energetic coupling model portrays a probabilistic relationship between NBD dimerization and gate opening: NBD dimerization makes the gate more likely to open and vice versa (Jih and Hwang, 2012).

To understand the coupling mechanism of CFTR gating, it would be very helpful if the pre- and post-hydrolytic states can be captured in a single-channel recording. Gunderson and Kopito (1995) were the first to do just that; they identified two open channel levels in each opening burst (O_1 with a smaller and O_2 with a larger single-channel conductance), and found a preferred opening/closing pattern of $C \rightarrow O_1 \rightarrow O_2 \rightarrow C$ transition over $C \rightarrow O_2 \rightarrow O_1 \rightarrow C$, an observation that is consistent with the idea of a free energy input from ATP hydrolysis to drive $O_1 \rightarrow O_2$ transition (Gunderson and Kopito, 1995). However, these two conductance levels with wild-type (WT) CFTR are not consistently seen by others. Then, Ishihara and Welsh (1997) found that this observed conductance difference is due to differential sensitivity of these two open channel conformations to pore blockade by the negatively charged buffer $MOPS^-$, suggesting that there is little intrinsic difference in chloride permeation between these two open states.

Lately, we accidentally found that the mutant R352C or Q, in the absence of $MOPS^-$, exhibits two distinct open-channel conductance levels (O_1 and O_2) with a similar preferred gating pattern of $C \rightarrow O_1 \rightarrow O_2 \rightarrow C$ transition over $C \rightarrow O_2 \rightarrow O_1 \rightarrow C$ (Jih et al., 2012), where O_1 and O_2 represent respectively pre- and post-hydrolytic open states. This report raises two interesting questions: First, is this phenotype unique to mutations at position 352, a pore-lining residue in TM6? Second, what is the structural mechanism for the different conductance levels observed for the pre- and post-hydrolytic open channel conformations?

Following up our previous SCAM study of CFTR's TM5 (Zhang and Hwang, 2015), we observed two open-channel conductance levels when the N306C mutant in a Cysless background was modified by $MTSES^-$ but not by $MTSET^+$. Statistical analysis of

opening/closing transitions revealed a preferred pattern of $C \to O_1 \to O_2 \to C$ transition over $C \to O_2 \to O_1 \to C$, similar to those seen in R352C. Furthermore, the O_1O_2 phenotype observed with N306D and N306E mutations under the WT background confirmed the idea that a net subtraction of a positive charge (R352C or Q and N306D or E) in the internal vestibule of the pore is responsible for the O_1O_2 phenotype. Interestingly, even with the net charge unaltered, moving the endogenous, positively-charged side chain (R303 or R352) along TM5 or TM6 also confers this unique phenotype. We next used $MOPS^-$ to investigate the possible structural basis for the difference in conductance between O_1 and O_2. Our data shows that in most cases the O_1 state is more sensitive to the channel impermeant blocker $MOPS^-$ than the O_2 state. More interestingly, this differential sensitivity to $MOPS^-$ is itself susceptible to the net charge in the internal vestibule. An expansion movement of the TMs coupled to ATP hydrolysis and a two-step scheme for $MOPS^-$ block are proposed to explain these observations.

3.3 Materials and Methods

Mutagenesis and channel expression

CFTR mutants in this study were constructed based on two CFTR backgrounds: wild-type background or Cysless background where all 18 endogenous cysteines were replaced with serine or leucine as reported previously (Bai et al., 2010). Site-directed mutagenesis was done using the QuikChange XL kit (Agilent Technologies). All mutations were subsequently confirmed by DNA sequencing (DNA core; University of Missouri-Columbia). Together with peGFP-C3 (Takara Bio Inc.) encoding the green fluorescent protein, the cDNA constructs of CFTR were co-transfected using PolyFect

transfection reagent (QIAGEN) into CHO cells, which were grown at 37 °C in Dulbecco's modified Eagle's medium containing 10% fetal bovine serum. The transfected cells were transferred onto 35 mm tissue culture dishes containing one layer of sterilized glass chips for cells to grow on and incubated at 27 °C for 2−7 days before electrophysiological experiments were performed.

Electrophysiology

All experiments were performed in the excised inside-out configuration. Micropipettes made of borosilicate capillary glass were pulled with a two-stage vertical puller (Narishige) and then fire-polished with a homemade microforge to reach a pipet resistance of 2−5 MΩ when the pipettes were filled with a standard pipet solution (140 mM NMDG-Cl, 2 mM $MgCl_2$, 5 mM $CaCl_2$ and 10 mM HEPES, adjusted to pH 7.4 with NMDG). Glass chips with transfected cells grown on were placed into a chamber on the stage of an inverted microscope (Olympus) and continuously perfused with a bath solution (145 mM NaCl, 5 mM KCl, 2 mM $MgCl_2$, 1 mM $CaCl_2$, 5 mM glucose, 5 mM HEPES, and 20 mM sucrose, adjusted to pH 7.4 with NaOH). Immediately after a membrane patch reached a seal resistance of >40 GΩ, it was excised, and continuously perfused with a standard perfusate ($[Cl^-]$ = 154 mM) containing 150 mM NMDG-Cl, 10 mM EGTA, 10 mM HEPES, 8 mM Tris, and 2 mM $MgCl_2$, adjusted to pH 7.4 with NMDG. For $[Cl^-]$-dependent experiments in Figure 3.6, high $[Cl^-]$ pipette solution containing ($[Cl^-]$ = 374 mM) 360 mM NMDG-Cl, 2 mM $MgCl_2$, 5 mM $CaCl_2$ and 10 mM HEPES, adjusted to pH 7.4 with NMDG was used to avoid a drastic osmolarity difference across the membrane. Perfusion solutions with different concentrations of chloride ions are made with 375 mM NMDG-Cl, 10 mM EGTA, 10 mM HEPES, 8 mM

Tris, and 2 mM MgCl$_2$, adjusted to pH 7.4 with NMDG for [Cl$^-$] = 379 mM, 750 mM NMDG-Cl, 10 mM EGTA, 10 mM HEPES, 8 mM Tris, and 2 mM MgCl$_2$, adjusted to pH 7.4 with NMDG for [Cl$^-$] = 754 mM and 1125 mM NMDG-Cl, 10 mM EGTA, 10 mM HEPES, 8 mM Tris, and 2 mM MgCl$_2$, adjusted to pH 7.4 with NMDG for [Cl$^-$] = 1129 mM. The 2 mM ATP solution containing 30 mM MOPS$^-$ in Figure 3.8 was adjusted to pH=7.5 with NMDG to ensure at least two thirds of the MOPS (FisherBiotech) molecules were in its negatively charged form as MOPS$^-$, which was proposed to be the effective form for blocking CFTR (Ishihara and Welsh, 1997). Experiments were conducted at room temperature (22−24 °C). Current signals at different holding potentials (−50 mV or − 80 mV or +50 mV) as required for different experimental purposes were acquired with a patch-clamp amplifier (EPC9, HEKA), filtered at 100 Hz, digitized online at 500 Hz with Pulse software (version 8.53, HEKA), and captured onto a hard disk. Fast solution exchange was achieved with a commercial solution exchange system (SF-77B Perfusion Fast-Step, Warner Instruments).

Reagents and Cysteine Modification.

MTS reagents [MTSES$^-$, MTSET$^+$ (Toronto Research Chemicals Inc.)] were prepared as 100 mM stock solutions in distilled deionized H$_2$O (ddH$_2$O) and stored at −70 °C. A single aliquot of the stock solution was thawed immediately before use and diluted into the perfusion solution with 2 mM ATP (SigmaAldrich) to modify the mutants in the presence of ATP (Figure 3.1, 3.S2 and 3.S6). PP$_i$ was purchased from Sigma-Aldrich Co. LLC. To prevent the thiol group of engineered cysteine from undergoing spontaneous oxidation (Li et al., 2005; Liu et al., 2006), we routinely added 2.67 mM

dithiothreitol (DTT) (SigmaAldrich) to the perfusion solution containing 32 IU/mL PKA and 2 mM ATP in inside-out experiments.

Data analysis

The single-channel amplitudes of O_1 state and O_2 state for most of the mutants exhibiting a clear O_1O_2 phenotype were measured by fitting the distributions in all-points histograms with built-in multi-Gaussian function (Igor 6.3). For some mutants with a smaller difference in the single-channel amplitudes between the O_1 and O_2 states such as R352Q, S307R/R303C/Cysless, all-points histogram method is not sensitive enough to resolve two peaks. In this case, the single-channel current amplitude of each state was measured by treating each opening burst as a "macroscopic" trace. For each "macroscopic" recording, the single-channel amplitudes of the O_1 and O_2 states were calculated by subtracting the baseline current from the mean "macroscopic" current amplitudes. At least five opening events of > 8 ms duration in one patch recording were analyzed and averaged for one data point. These averaged single-channel amplitudes of O_1 and O_2 states from each trace also yield one set of the absolute and normalized differences between O_1 and O_2 states in Figure 3.6C and one set of F_b for MOPS$^-$ block of the two open states in Figure 3.9. The final mean and SEM were calculated from more than three recordings.

Statistical analyses in Figure 3.T1 and Figure 3.T2 were done using the same method employed in our previous study (Jih et al., 2012). Here we chose 8 ms as the cutoff to identify a state, which represents 5 data points at the 500 Hz sampling rate, to avoid counting non-CFTR static spikes or noises (three data points, or 4 ms, to define an event of current rise/drop). This criterion should minimally affect our topological analysis

of gating patterns since the mean burst durations of the O_1 state and the O_2 state are 116 ms and 55 ms respectively for N306D and 135 ms and 100 ms for M348R/R352Q measured by dwell-time histograms (Figure 3.S1). Current traces recorded at negative voltage were presented in all figures as upward deflections except that in Figure 3.7 and 3.8E, where positive currents were presented as upward deflections. The transmembrane segments (TM6, TM5 and TM12) in the cartoon in Figure 3.10, Figure 3.S3 and Figure 3.S4 were extracted from the open channel homology model built by Dalton et al. (2012) and rearranged for cosmetic purpose to show the proposed change in volume of the internal vestibule upon the O_1 to O_2 transition. To more accurately illustrate the relative positions among the residues of interest in Figure 3.4, we adopted the first high-resolution cryo-EM structure of CFTR published in Zhang and Chen (2016). Although this atomic structure represents zebrafish CFTR, since the current as well as previous functional studies were carried out in human ortholog, residues in this cryo-EM structure were discussed in accordance to their corresponding positions in human CFTR. All the pictures extracted from the homology model or cryo-EM structure of CFTR were prepared with PyMOL (version 1.3, Schrödinger). All results are presented as means ± SEM; N is the number of experiments.

Abbreviations used in this paper: ABC, ATP-binding cassette; CFTR, Cystic Fibrosis Transmembrane conductance Regulator; NBD, nucleotide binding domain; TMD, transmembrane domain; TM, transmembrane segments; SCAM, substituted cysteine accessibility methodology; RD, Regulatory Domain; MTS, methanethiosulfonate; $MTSES^-$, 2-sulfonatoethyl MTS; $MTSET^+$, 2-trimethylaminoethyl MTS; DTT,

dithiothreitol; WT, wild-type; PP$_i$, pyrophosphate; MOPS, 3-(N-morpholino)propanesulfonic acid; cryo-EM, electron cryo-microscopy.
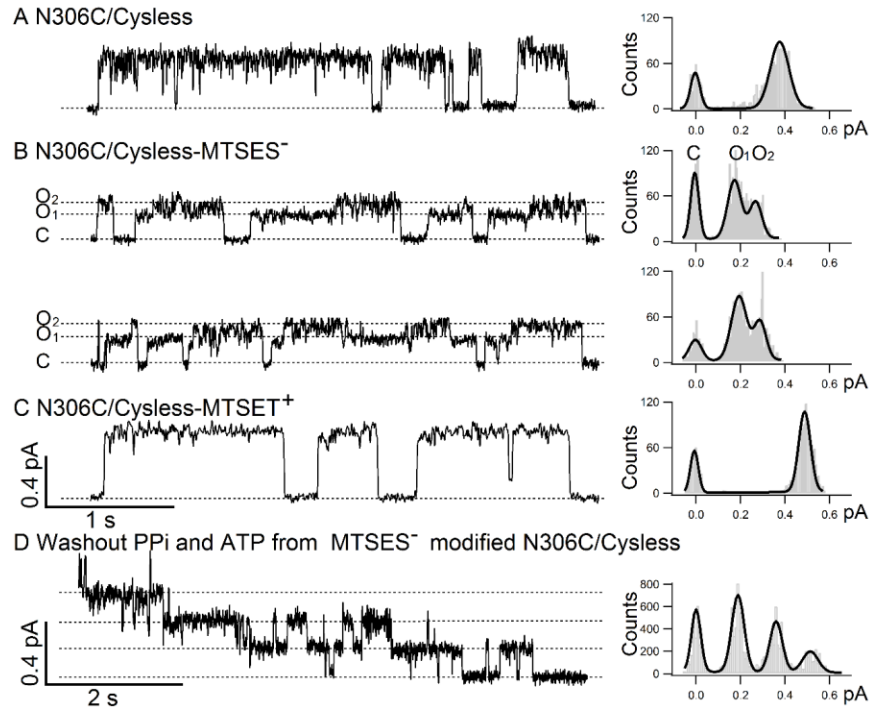
Figure 3.1. N306C/Cysless modified by MTSES⁻ shows O_1-O_2 transitions. Single-channel recordings were conducted under -50mV. **A.** Left part is a representative single-channel trace of N306C/Cysless and the all-points histogram on the right side shows only one conductance level (0.40 ± 0.02 pA, N = 14). **B.** Single-channel recordings of N306C/Cysless modified by negatively charged thiol-specific reagent MTSES⁻ show two distinct single-channel conductance levels: small one O_1 (0.19 ± 0.02, N = 3) and large one O_2 (0.30 ± 0.02, N = 3) with a preferred transition order of $C \rightarrow O_1 \rightarrow O_2 \rightarrow C$. The difference between two open-channel conductance levels is clearly differentiated in the all-points histogram on the right. **C.** In contrast, N306C/Cysless modified by positively charged thiol-specific reagent MTSET⁺ shows a single and yet larger open-channel current amplitude (0.49 ± 0.02, N = 4) compared with the one before modification in panel A. **D.** A representative recording of the washout phase of a macroscopic current trace using ATP-free perfusion solution from a patch containing multiple MTSES⁻ modified N306C/Cysless channels locked open by PP_i and ATP. The stepwise closing of each channel is shown in the trace on the left and the long burst duration in the absence of ATP before channels close is indicative of these channels being locked open by PP_i and ATP into an open channel conformation with two NBDs in a head-to-tail dimeric configuration. The single-channel amplitude (0.19 ± 0.01, N = 4) measured in the all-points histogram on the right is identical to the single-channel amplitude of the O_1 state in panel B.

3.4 Results

Adding one negative charge at position 306 of CFTR's TM5 results in two distinct open channel conductance levels: O_1 and O_2

In our previous cysteine scanning study on the 5th transmembrane segment (TM5) of CFTR, we have identified six pore-lining residues along this TM (Zhang and Hwang, 2015). All six pore-lining residues, A299, R303, N306, S307, F310 and F311, are proposed to form part of the internal vestibule of CFTR's pore as they are only accessible to thiol-specific reagent such as MTSES$^-$ and MTSET$^+$ from the intracellular side of the membrane. While the modification of the cysteine residue introduced at each of the positions mentioned above with negatively charged MTSES$^-$ reduced the single-channel amplitude (Zhang and Hwang, 2015), a closer inspection of the MTSES$^-$ modified single-channel data revealed an unexpected finding: two distinct open channel levels were seen in MTSES$^-$ modified N306C/Cysless. As shown in Figure 3.1A, the single-channel trace of N306C/Cysless before MTSES$^-$ modification exhibits a uniform current amplitude (0.40 ± 0.02 pA, N = 14). However, once modified by MTSES$^-$, opening bursts with two distinct conductance levels were observed (Figure 3.1B): a smaller O_1 (0.19 ± 0.02 pA, N = 3) and a larger O_2 (0.30 ± 0.02 pA, N = 3), a phenotype akin to that of the mutant R352C or R352Q we have characterized previously (Jih et al., 2012). In contrast, for the same mutant N306C/Cysless, the modification by positively charged MTSET$^+$ does not yield multiple conductance levels (Figure 3.1C), but it does increase slightly the single-channel amplitude to 0.49 ± 0.02 pA (N = 4).

Statistical analysis on the gating behavior of the MTSES$^-$ modified N306C/Cysless channels in Figure 3.T1 revealed a preferred pattern of C$\rightarrow$O$_1$$\rightarrow$O$_2$$\rightarrow$C transition over C$\rightarrow$O$_2$$\rightarrow$O$_1$$\rightarrow$C, similar to those seen in R352C (Jih et al., 2012), suggesting a violation

of microscopic reversibility that requires a free energy input to drive CFTR gating in a circular manner. To further test whether the O_1 and O_2 states in MTSES$^-$ modified N306C/Cysless channels also label pre-hydrolytic and post-hydrolytic states, we applied 4 mM pyrophosphate (PP$_i$), a poorly hydrolyzable phosphate analog, with 2 mM ATP together to lock-open MTSES$^-$ modified channels, and subsequently washed out all the ligands. As seen in Figure 3.1D, the locked-open channels close one at a time, resulting in a staircase pattern of current drop. All-points histogram analysis of this part of the recording (Figure 3.1D, right panel) reveals the single-channel amplitude of each locked-open channel as 0.19 ± 0.01 pA (N = 4), which is virtually identical to the single-channel amplitude of the O_1 state shown in Figure 3.1B. The observation that PP$_i$ can lock the MTSES$^-$ modified N306C/Cysless channels into the O_1 state supports the idea that O_1 state and O_2 state in MTSES$^-$ modified N306C/Cysless channels indeed represent respectively the pre- and post-hydrolytic open states since PPi, like the non-hydrolyzable ATP analog (Adenylyl-imidodiphosphate) AMP-PNP, was proposed to lock the channel into an open conformation with a dimerized NBD where its nucleotide binding site 2 and site 1 were occupied by PPi and ATP respectively (Tsai et al., 2009).

To test the hypothesis that the observed difference in single-channel amplitudes between O_1 and O_2 states caused by MTSES$^-$ modification is due to the introduced negative charge other than any unusual properties of this reagent or Cysless CFTR, we engineered a negative charge directly into WT CFTR at position 306 by making N306D and N306E mutations. Figure 3.2 shows representative single-channel traces of N306D and N306E, both of which exhibit similar two open channel states that are indistinguishable from those of the MTSES$^-$ modified N306C/Cysless channels: O_1 =

0.18 ± 0.01 pA and $O_2 = 0.24 \pm 0.01$ pA, N = 3, for N306D; $O_1 = 0.19 \pm 0.01$ pA and O_2 $= 0.27 \pm 0.01$ pA, N = 3, for N306E. Note in Figure 3.2B showing the expanded openings marked in Figure 3.2A, we could also discern a preferred gating pattern of $C \rightarrow O_1 \rightarrow O_2 \rightarrow C$, which is confirmed by statistical analyses of these traces (Figure 3.T2). These results support the notion that it is the negative charge introduced to position 306 in the internal vestibule of CFTR's pore that causes the appearance of two sub-conductance levels O_1 and O_2 in an opening burst with preferred O_1 to O_2 transitions, namely, the O_1O_2 phenotype.

Gating topology	O_1-O_2	O_1	O_2	O_2-O_1	$(O_1$-$O_2)^n$	Total
No. of Events	730	480	119	15	148	1492
Percentage	(49%)	(32%)	(8%)	(1%)	(10%)	(100%)

Figure 3.T1. Summary of opening events by different gating patterns in N306C/Cysless modified by MTSES⁻. Five categories of gating topologies are illustrated on the top of the table. The number of events and percentage for each topology are displayed. Bursts were categorized as described in Materials and Methods. Data in this table show that C→O_1→O_2→C is the preferred gating pattern and a considerable amount of events with more than one O_1→O_2 transition were observed in the MTSES⁻ modified N306C/Cysless. Of note, because of the intrinsic instability of the O_2 state, the analysis method employed inevitably overestimates the number of events in the second category and underestimates those in the rest of the categories.

N306D-CFTR	O_1-O_2	O_1	O_2	O_2-O_1	$(O_1$-$O_2)^n$	Total
No. of Events	491	207	104	13	217	1032
Percentage	(48%)	(20%)	(10%)	(1%)	(21%)	(100%)

Figure 3.T2. Summary of opening events by different gating patterns in N306D. Data in this table show that C→O_1→O_2→C (first category) is the preferred gating topology in N306D.
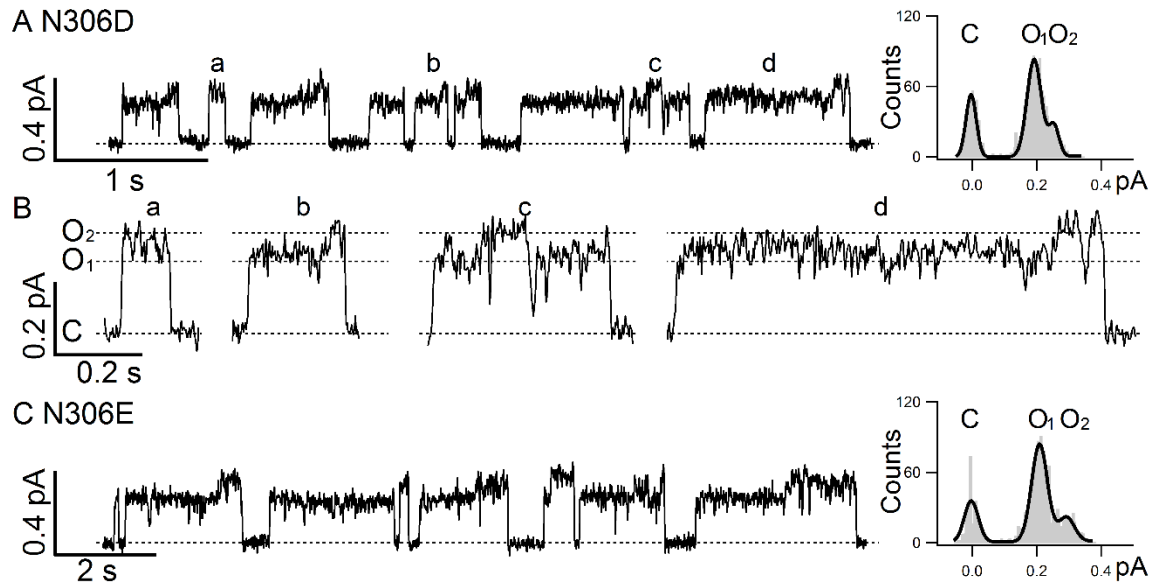
Figure 3.2. N306D/E channels present clear O_1O_2 phenotype. A. A representative single-channel recording of N306D in the wild-type background shows characteristic O_1O_2 phenotype, supporting the idea that it is the negative charge introduced at position 306 that accounts for the O_1O_2 phenotype displayed in N306D and in MTSES$^-$ modified N306C/Cysless. Single-channel amplitudes of O_1 (0.18 ± 0.01, N = 3) and O_2 (0.24 ± 0.01, N = 3) states can be measured in the all-points histogram on the right. **B.** Expanded opening bursts show details of each opening events as marked in panel A. **C.** A representative single-channel recording of N306E in the wild-type background further confirms the role of a negative charge at position 306 in conferring the O_1O_2 phenotype. All-points histogram shows distinct single-channel amplitudes of the O_1 (0.19 ± 0.01, N = 3) and O_2 states (0.27 ± 0.01, N = 3).

The position of charge also determines the O_1O_2 phenotype

As reported previously (Jih et al., 2012), this O_1O_2 phenotype is a distinct characteristic of R352C or Q. We noted here that R352 in TM6 is at a similar topological location as N306 in TM5 (Riordan et al., 1989). Recent computer modeling of CFTR's pore also placed these two residues at the same level in the internal vestibule of CFTR (Dalton et al., 2012; Mornon et al., 2015), a picture confirmed lately by the first high-resolution cryo-EM structure of the whole CFTR protein (Zhang and Chen 2016; also see Figure 3.4 below). It is also interesting to note that the neutralization of the positively charged arginine at position 352 and the introduction of a negative charge side chain at position 306 cause a similar electrostatic effect in the internal vestibule of the pore—a net decrease of a positive charge. The experiments in Figure 3.3 demonstrate that this decrease of the positive potential in the internal vestibule, as happened in R352C or Q and N306D or E, is not the only factor that determines the O_1O_2 phenotype. Figure 3.3A shows a representative single-channel trace of R352Q, recorded at the same voltage (-50 mV) as that in Figure 3.1 and Figure 3.2. As reported before (Jih et al., 2012), the conductance of R352Q is smaller compared to that of WT channels, and hence the difference between O_1 and O_2 states is barely discernable. (The difference in single-channel amplitude only becomes apparent when [Cl$^-$] is increased; see Jih et al., 2012 for details.) However, although introducing a positively charged arginine to position 348 in the R352Q background (M348R/R352Q double mutation) increased single-channel current amplitudes for each open state presumably because of partial restoration of the positive potential in the pore, the O_1O_2 phenotype remained (Figure 3.3B). Interestingly, while the absolute difference ($i_{O2} - i_{O1}$) in current amplitude between the O_1 and O_2 state

becomes larger with the introduction of an arginine at position 348, the relative difference $((i_{O2} - i_{O1})/i_{O1})$ is unchanged (55.6 + 5.0 % for R352Q, n = 4; 50.1 + 4.0 % for M348R/R352Q, n = 4), suggesting that the arginine at position 348 increases the single-channel amplitude proportionally for both states. As a control, Figure 3.3C shows a single-channel trace of M348R which displays only one single open state with an amplitude of 0.35 ± 0.01 pA (N = 4) just like WT channels despite one additional positive charge engineered into the pore (Bai et al., 2010; Zhou et al., 2010). Thus, the occurrence of the O_1O_2 phenotype for R352Q is not solely because of a change of the net charge in the internal vestibule; instead, we conclude that the position of the charged residue(s) in TM6 in the internal vestibule of CFTR's pore plays a critical role in determining the O_1O_2 phenotype.
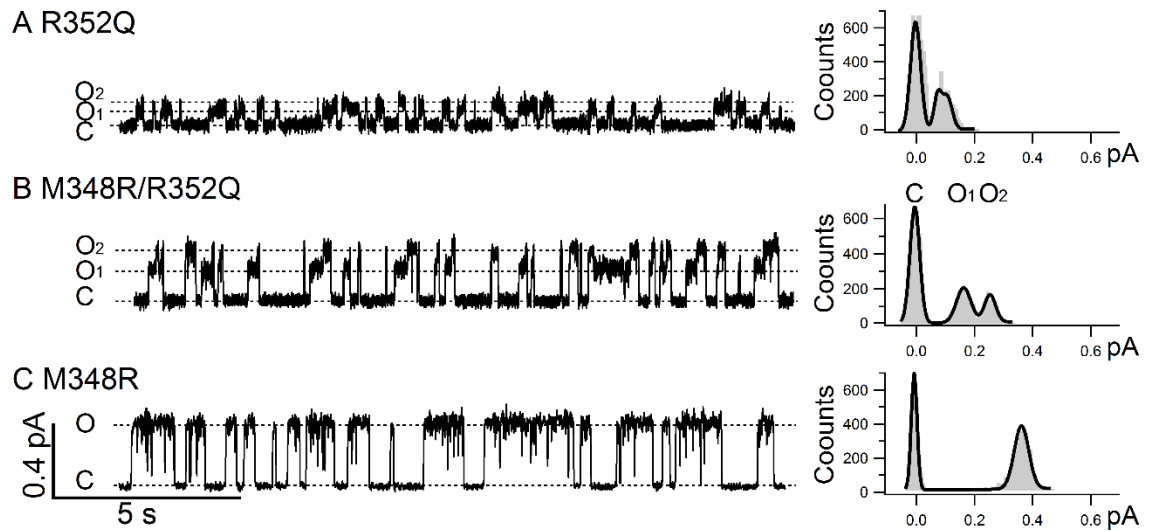
Figure 3.3. O_1O_2 phenotype revealed by charge displacement in TM6. A. A representative recording of R352Q barely shows two conductance levels because the single-channel amplitudes of both O_1 state (0.09 ± 0.01, N = 4) and O_2 state (0.13 ± 0.01, N =4) are dramatically reduced due to the neutralization of arginine 352 in the internal vestibule of CFTR. The two peaks in the all-points histogram on the right are mostly coalesced into a single peak. **B.** A representative recording of the double mutant M348R/R352Q also displays O_1O_2 phenotype with much higher single-channel amplitudes for both O_1 state (0.17 ± 0.01, N = 4) and O_2 state (0.25 ± 0.01, N = 4) as measured in the all-points histogram on the right. **C.** A representative recording of M348R with a single-channel amplitude of 0.35 ± 0.01 (N = 4) and the corresponding all-points histogram on the right.

The results shown in Figure 3.3 implicate the importance of the location of positive charges in the internal vestibule in deciding the O_1O_2 phenotype. Inspecting the pore-lining residues of TM5, we also found an arginine at position 303, mutations of which have been shown to decrease the single-channel conductance (Aubin and Linsdell, 2006; Zhou and Linsdell, 2007; Zhang and Hwang, 2015). In both the homology model of CFTR's open channel conformation and the cryo-EM structure of CFTR's pre-phosphorylated closed conformation (Dalton et al., 2012; Zhang and Chen, 2016), R352, M348 and N306 are spatially close to each other, all residing in the internal vestibule of CFTR's pore (Figure 3.4). Furthermore, R303 is just one helical turn internal to N306. The idea that the location of the positively charged residues in TM6 in the internal vestibule plays a critical role in conferring the O_1O_2 phenotype suggests that moving this arginine along TM5 may also result in the O_1O_2 phenotype. Unlike R352C/Cysless, the single mutation R303C/Cysless of neutralizing the arginine at position 303, does not show the O_1O_2 phenotype (Figure 3.8D). However, just like M348R/R352Q, moving the arginine from position 303 to several other pore-lining positions including 307, 310 and 311 resulted in O_1O_2 phenotype (Figure 3.5). Interestingly, the larger the distance between the moved arginine and position 303, the higher the difference of the single-channel amplitude between O_1 and O_2 is. For example, a visual distinction of O_1 and O_2 in the S307R/R303C mutant is only possible in high-quality recordings with an exceedingly stable baseline (Figure 3.5A), although corresponding all-points histogram fails to clearly dissect two conductance levels. However, Figure 3.5B and 3.5C show respectively discernable O_1O_2 phenotype for F311R/R303C/Cysless and F310R/R303C/Cysless. These representative single-channel traces as well as expanded individual opening bursts

in Figure 3.5D show telltale signs of irreversible gating (i.e., predominant $C\rightarrow O_1\rightarrow O_2\rightarrow C$). The O_1O_2 phenotype displayed here with the double mutants is not due to the addition of arginine at positions 307, 310 and 311, since simple addition of a positive charge at these positions does not yield the O_1O_2 phenotype (Figure 3.S2). The existence of the O_1O_2 phenotype requires simultaneous neutralization of the arginine at position 303. Collectively, the data from the arginine swap experiments in Figure 3.5 suggest that, like R352 in TM6, the *position* of this positively-charged side chain of TM5 in the internal vestibule of CFTR's pore is critical in imparting the O_1O_2 phenotype.

A Cross-Eye Stereo Lateral View of TMDs
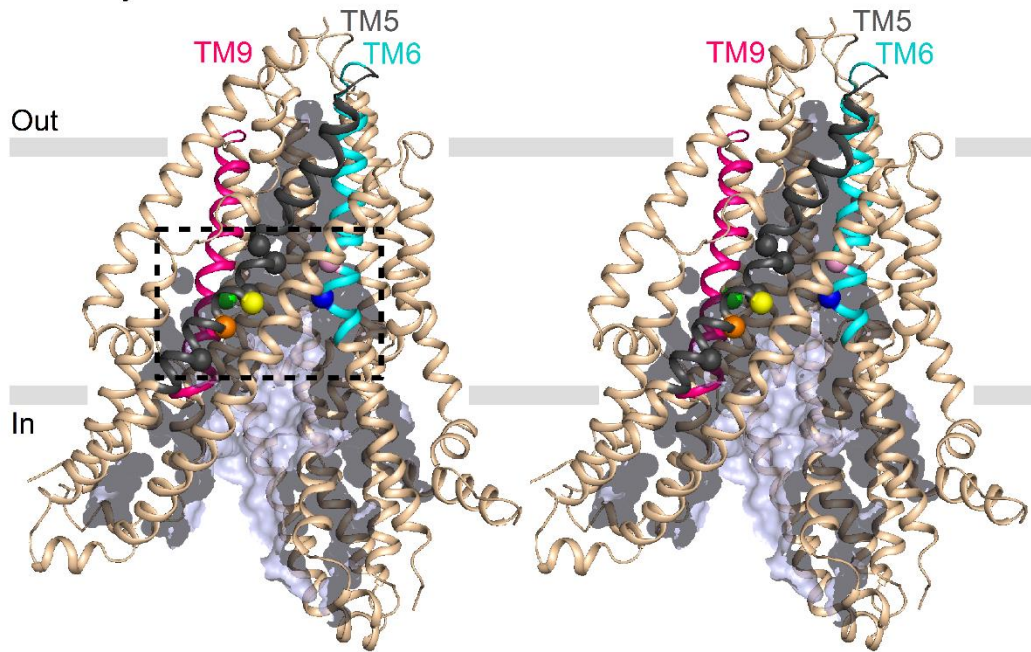
B Enlarged View of Squared Region in A
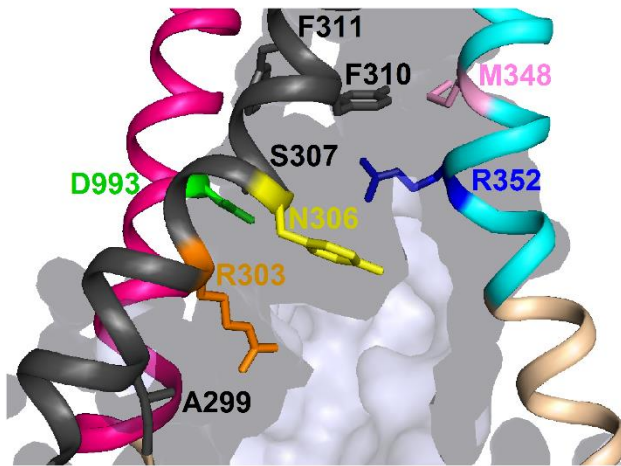
C Top View of TM5, 6 and 9
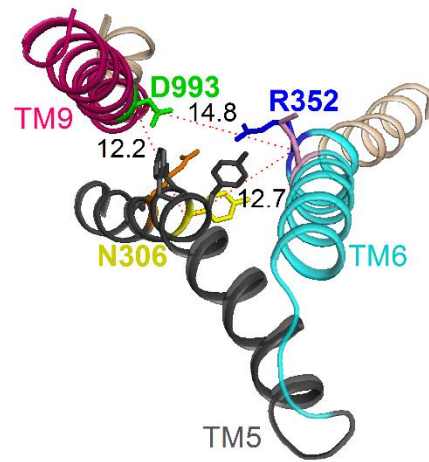
Figure 3.4. Pore-lining residues along TM5 located spatially close to R352 on TM6. A. A Cross-Eye

stereo lateral view of CFTR's two TMDs based on the cryo-EM structure of CFTR (Zhang and Chen,

2016). The whole TMDs is colored in wheat. TM6 is colored in cyan, TM9 in magenta and TM5 in black.

The pore-lining residues R352 and M348 in TM6 are colored in blue and pink respectively, the pore-lining

residues R303 and N306 along TM5 are colored in orange and yellow respectively, while A299, S307,

F310 and F311 along TM5 are colored in black. D993 in TM9 is colored in green. The surface of the

internal vestibule is shown with its aqueous side in light blue and back side in light blue shadow. From this

lateral view, R352 and D993 reside at a critical location where the internal vestibule tapers down to the narrow region. **B.** Enlarged view of the squared region in A. If we use R352/D993 as a reference plane, pore-lining M348, F310 and F311 lie slightly above, whereas N306 lies below, this plane. In contrast, R303 and A299 reside at a more internal and spacious region of the internal vestibule. **C.** Top view of TM5, 6 and 9. Distances between the residues were measured in Angstrom (Å).
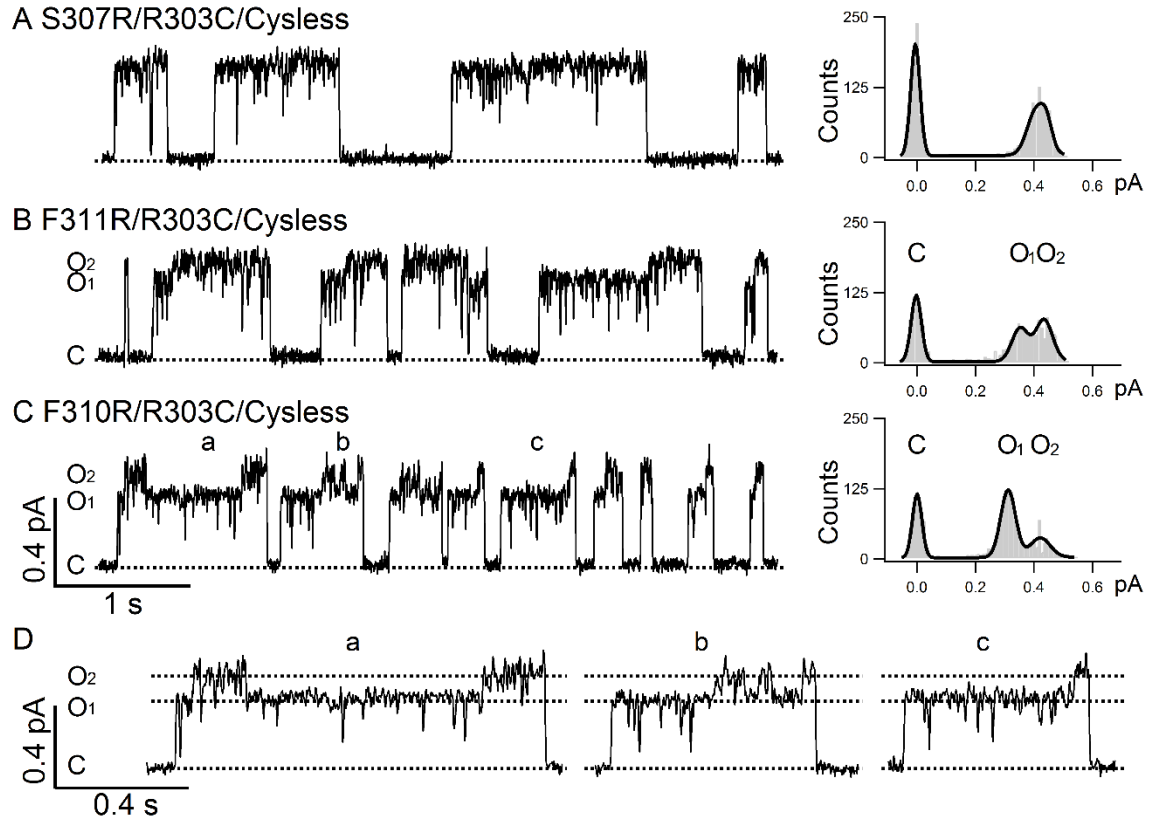
Figure 3.5. The position of arginine in TM5 plays a role in determining the current amplitudes of O_1 and O_2 states. A. A representative recording of S307R/R303C/Cysless shows a slight and barely discernible difference between the O_1 and O_2 states. But the all-points histogram fails to distinguish these two states. **B.** Clear resolution of the O_1 and O_2 states in F311R/R303C/Cysless in both single-channel trace (left) and all-points histogram (right). **C.** A representative recording of F310R/R303C/Cysless on the left shows clearly resolvable two open states reflected as two distinct peaks in the all-points histogram on the right. **D.** Expanded opening bursts marked in panel **C** to show detail transitions in a gating cycle. The burst marked c shows a prototypical gating topology of C→O_1→O_2→C.
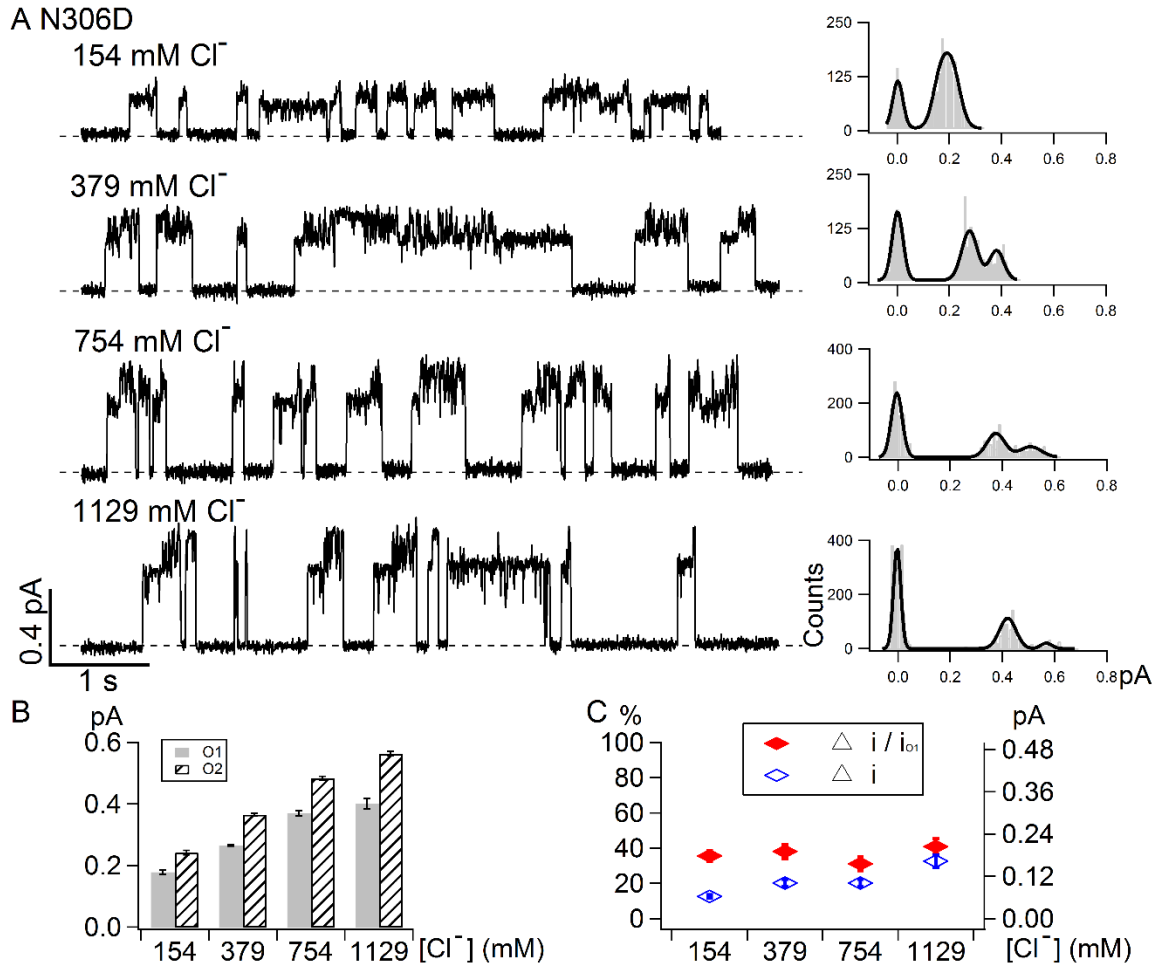
Figure 3.6. Effects of cytoplasmic [Cl⁻] on the current amplitudes of the O_1 and O_2 states in N306D. A. Representative single-channel opening events of N306D under different intracellular chloride concentrations as marked with the corresponding all-points histograms on the right. The current amplitudes of both O_1 state and O_2 state are increased with increasing chloride concentrations but the difference between these two open states remains measureable even at the highest concentration tested (1129 mM). **B.** Summary of single-channel amplitudes of N306D at different cytoplasmic chloride concentrations. **C.** Summary of normalized difference ($\Delta i/i_{O1}$, red closed diamond, left vertical axis) and absolute difference (Δi, blue open diamond, right vertical axis) between O_1 and O_2 states under different chloride concentrations.
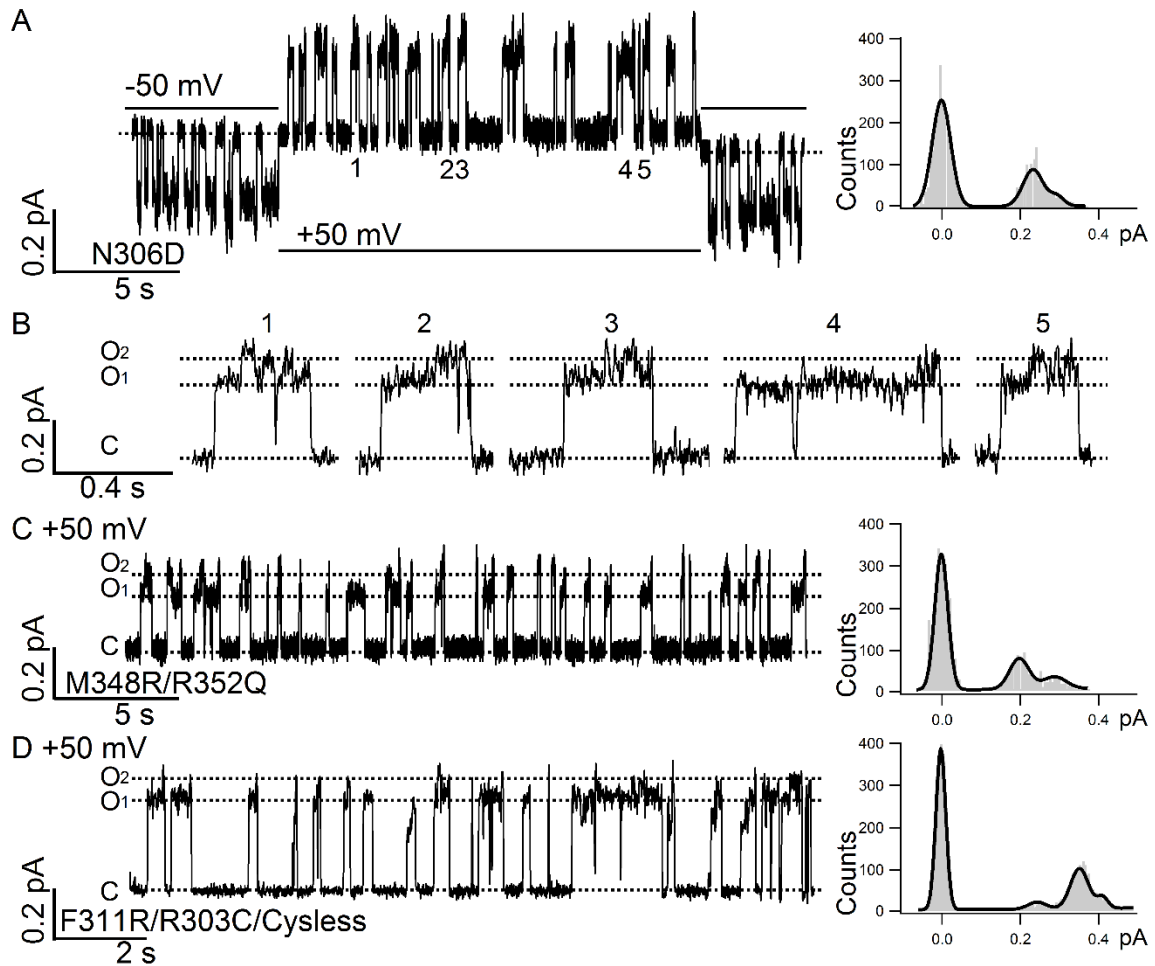
Figure 3.7. Effects of membrane potentials on the O_1O_2 phenotype. A. A real-time single-channel recording of N306D upon voltage change from - 50 mV (opening: downward deflections) to + 50 mV (opening: upward deflections) showing the presence of clearly resolvable O_1 and O_2 states at ± 50 mV. The all-points histogram for the recording at + 50 mV shows discernable two open states. **B.** Opening bursts recorded at + 50 mV indicated in panel **A**. Note the preferred gating topology of $C \rightarrow O_1 \rightarrow O_2 \rightarrow C$ is also seen at + 50 mV. **C.** A representative recording and its all-points histogram showing the existence of the O_1O_2 phenotype at + 50 mV for M348R/R352Q. **D.** The O_1O_2 phenotype at + 50 mV and its all-points histogram for F311R/R303Q/Cysless. A third peak representing a smaller subconductance state is detected in the all-points histogram, which is also observed in all other CFTR mutations including wild-type CFTR occasionally. However, the overall gating topology is still dominated by the O_1 and O_2 states. As described in the Materials and Methods, for a clearer data presentation, all single-channel traces recorded at negative

membrane potentials were inverted except traces in this figure and Figure 3.8E where conventional

presentations were adopted.

Effects of membrane potentials and cytoplasmic [Cl⁻] on O_1O_2 phenotype

It has been proposed that the positively charged residues (arginine/lysine) in the internal and external vestibules of CFTR's pore play important roles in concentrating the charge carrier chloride from the surrounding solutions, and hence facilitate high chloride conductance through surface charge effects (Aubin and Linsdell, 2006; Cui et al., 2008; Bai et al., 2010; El Hiani and Linsdell, 2012). As many of our molecular manipulations alter the net charge (e.g., R352Q, N306D), we wonder if the difference in single-channel amplitudes between the O_1 and O_2 states can be attributed to possible different surface charge effect exerted by the charged side chain. We therefore tested if increasing [Cl⁻] can alter the difference in single-channel amplitudes between the O_1 and O_2 states. Left panel in Figure 3.6A shows representative single-channel opening events of N306D at different concentrations of cytoplasmic chloride ions. The all-points histograms (Figure 3.6A right) show that both O_1 and O_2 states are clearly discernable within the experimental chloride range. Figure 3.6B summarizes the single-channel amplitudes of the O_1 and O_2 states for N306D under the indicated conditions. Figure 3.6C shows the absolute difference in single-channel amplitudes between the O_1 and O_2 states (blue open diamond) and the normalized difference ($\Delta i/i_{O1}$) in single-channel amplitudes between the O_1 and O_2 states (red closed diamond). Within the range of [Cl⁻] tested, neither the absolute difference nor the normalized difference between the O_1 and O_2 states is very sensitive to the changes of [Cl⁻]. This result together with the observation that the specific location of the charge plays a major role in deciding the O_1O_2 phenotype suggest that the surface charge effect unlikely accounts for our observations. Instead, it is more likely that the pre- and post-hydrolytic states assume different pore structures, and the functional

consequence—chloride permeation through the pore—of this structural difference is exaggerated by our mutations.

The idea of different pore structures is consistent with the observation that the O_1O_2 phenotype also exists at positive voltage when the chloride ions flow in an opposite direction. Figure 3.7A shows a continuous recording of a single N306D channel at $\pm$ 50 mV. In Figure 3.7B, the expanded view of the numbered opening bursts in panel A shows two distinct open states and the preferred open transitions of C→O_1→O_2→C. The existence of the O_1O_2 phenotype at positive voltage is also seen in mutants with net charge unaltered, e.g., M348R/R352Q (TM6, Figure 3.7C) and F311R/R303C/Cysless (TM5, Figure 3.7D). Thus, we propose that, upon ATP hydrolysis, CFTR's pore undergoes some conformational changes that affect the ion permeation properties; while this functional alteration may not be large enough to become discernable in WT channels, our mutations, by changing charge locations in the internal vestibule, exacerbate the functional consequence of hydrolysis-driven conformational changes in the pore and thus make possible the visualization of the O_1 and O_2 states. Since our mutations are all located in the internal vestibule of the pore, these conformational changes following ATP hydrolysis may mostly happen in this part of the ion permeation pathway (see Discussion for detailed elaboration).

O_1 and O_2 states show different responses to MOPS$^-$ block

To get a glimpse of possible structural differences between the O_1 and O_2 states, we employed anionic channel blockers MOPS$^-$, to probe these two open states. We reasoned

that the bulky part of MOPS$^-$ is too large to pass the narrow region of the pore; thus, structural changes in the internal part of the pore during O_1 to O_2 transition may confer differential sensitivity of these two states to MOPS$^-$ block as reported for WT channels (Ishihara and Welsh, 1997).
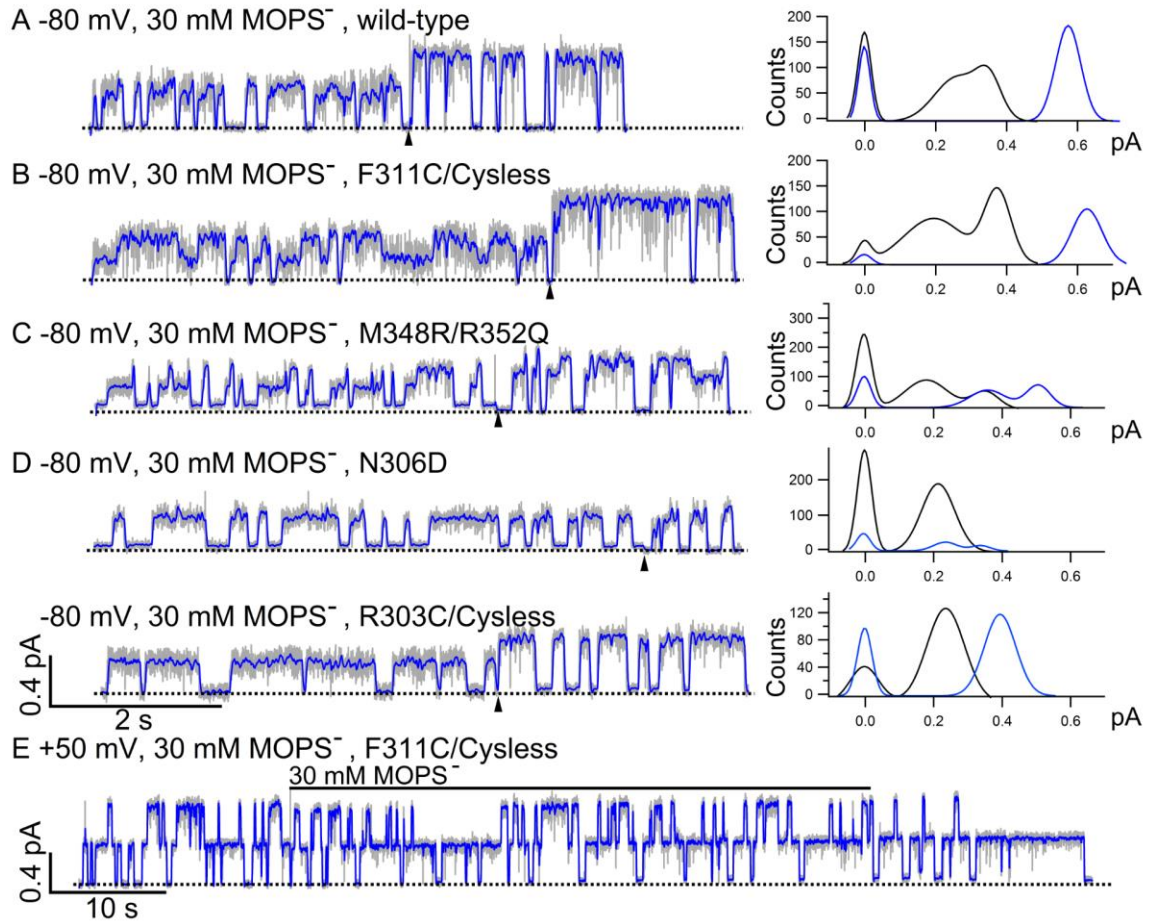
Figure 3.8. O_1 and O_2 states exhibit differential sensitivity to channel-impermeant blocker MOPS⁻.

Current traces filtered at 100 Hz are shown as a gray background whereas the same traces filtered at 10 Hz are colored in blue and super-positioned. For the traces in panel **A** to **F**, 30 mM MOPS⁻ were applied in the presence of 2 mM ATP in the early part of the recordings and then removed from the ATP-containing solution at the time point indicated by the arrow heads. The all-points histogram for the traces in the absence of MOPS⁻ are shown as solid blue curves and the histogram for the traces in the presence of MOPS⁻ are shown as solid black curves. Dashed lines represent the baselines. **A.** A representative trace of WT CFTR in the presence or absence of MOPS⁻. As reported previously (Ishihara and Welsh, 1997), two distinct open channel conductance levels are clearly discerned once the data are filtered at 10 Hz. **B.** Similar to WT CFTR that has only one resolvable open channel conductance level in the presence of ATP, F311C/Clysess also shows two distinct open channel conductance levels once blocked by MOPS⁻. **C.** Amplification of the difference in single-channel amplitude between O_1 and O_2 states by MOPS⁻ in

M348R/R352Q, which itself exhibits the O_1O_2 phenotype. The normalized difference ($\Delta i/i_{O1}$) is $51 \pm 2\%$, without MOPS$^-$ (N = 9) but $101 \pm 2\%$ with MOPS$^-$ (N = 4). **D.** Effects of net charge in the internal vestibule on the differential sensitivity of O_1 and O_2 states to MOPS$^-$ block. Contrary to the results in panels **A**, **B** and **C**, N306D with one additional negative charge in the internal vestibule displays O_1O_2 phenotype in the presence of ATP, but its O_1 and O_2 states show similar sensitivity to MOPS$^-$ block. The O_2 states of N306D in the presence of MOPS$^-$ could not be resolved by the all-points histogram due to its small single-channel amplitude and the brief open time of O_2 state. Similar to N306D, R303C/Cylsess also has one net charge deducted from the internal vestibule of CFTR's pore. For this mutant, however, only one open channel level is seen in the absence or presence of MOPS$^-$. **E.** Compared with the result in panel **B**, the representative trace of F311C/Cysless recorded at $+ 50$ mV in the presence of 2 mM ATP shows negligible MOPS$^-$ block.

Figure 3.8A shows WT-CFTR current trace in the presence or absence of MOPS$^-$. Indeed, two distinct current levels can be seen at 10 Hz filtering. This differential sensitivity to MOPS$^-$ block is even more prominent with the mutant F311C/Cysless (Figure 3.8B). While WT and F311C/Cysless constructs possess no additional charge in the internal vestibule, the mutant A299R with a net increase of one charge in the internal vestibule also exhibits two conductance levels in the presence of MOPS$^-$, indicative of differential blockade of the O_1 and O_2 states by MOPS$^-$ (raw trace not shown but see data in Figure 3.9). Interestingly, even for M348R/R352Q where the single-channel amplitudes of O_1 and O_2 states are already clearly discernible in the absence of MOPS$^-$, the O_1 state is as well blocked more by MOPS$^-$ compared with the O_2 state, resulting in an enlarged difference between the single-channel amplitudes of two open states (Figure 3.8C). However, this differential blocking effect of MOPS$^-$ is diminished for mutants with an additional negative charge in the internal vestibule. When we tested MOPS$^-$ on two mutants N306D and R303C/Cysless, where the internal vestibule loses one net charge, a uniform reduction of the current amplitude by MOPS$^-$ was observed as if O_1 and O_2 states of these two mutants show the same sensitivity to MOPS$^-$ (Figure 3.8D and Figure 3.9). Unlike WT and F311C/Cysless that have only one conductance without MOPS$^-$ but show the O_1O_2 phenotype once blocked by MOPS$^-$, R303C/Cysless with net charge of minus one shows no O_1O_2 phenotype with or without MOPS$^-$, which means both O_1 state and O_2 state are equally blocked by MOPS$^-$. The voltage-dependent nature of MOPS$^-$-induced block is demonstrated here with the example that no discernable changes of the single-channel amplitude were observed when 30 mM MOPS$^-$ was applied at +50 mV to the patch containing F311C/Cysless channels (Figure 3.8E). Figure 3.9

summarizes this series of experiments demonstrating an intriguing effect of the net change of charge in the internal vestibule on the sensitivity of the O_1 and O_2 states to MOPS$^-$ block. In the *Discussion*, we will attempt to propose a simple structural alteration during O_1 to O_2 transition to explain most, if not all, these seemingly perplexing observations.
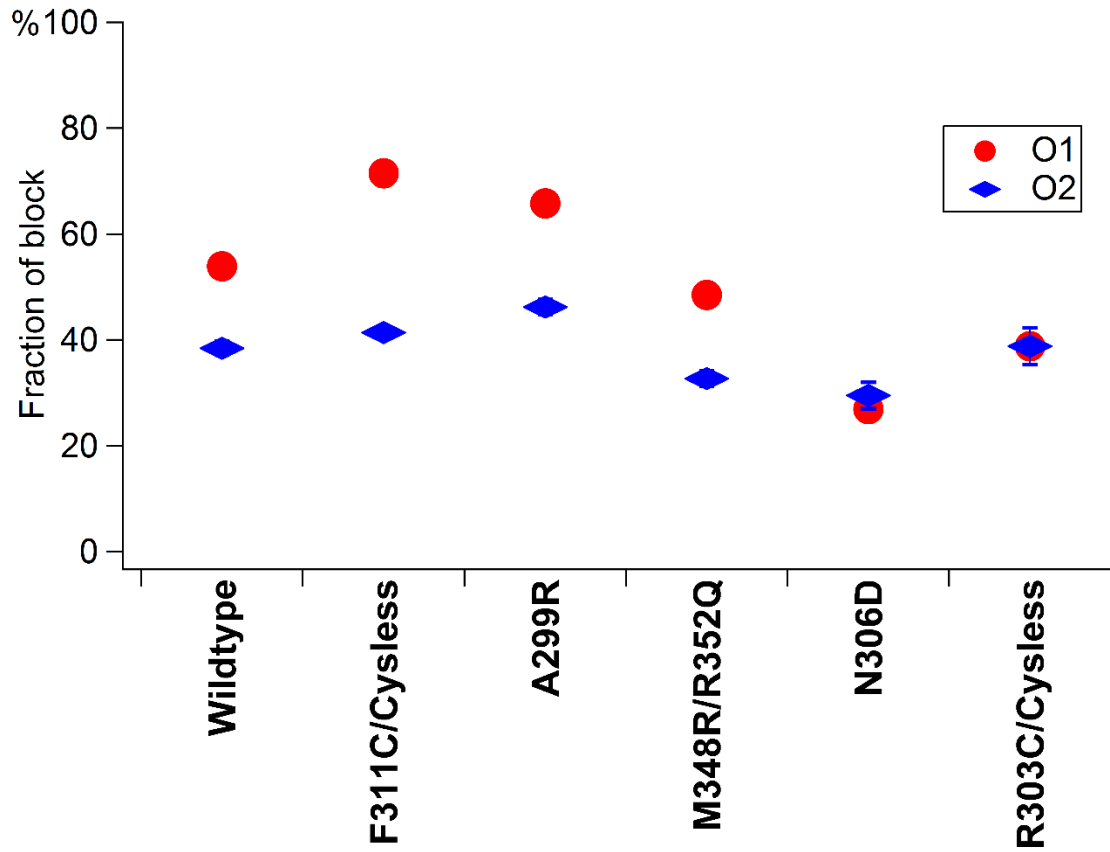
Figure 3.9. Summary of the fraction of block by MOPS⁻ at -80 mV for data presented in Figure 3.8.

The O_1 state (red closed circles) is more sensitive to MOPS⁻ than the O_2 state (blue closed diamonds) for mutants with the net charge in the internal vestibule unaltered or positive one added. Using WT channels as a control, it appears that these mutations increase MOPS⁻ block of the O_1 state not of the O_2 state. But for mutants with the net charge of minus one (N306D and R303C/Cysless), the O_1 and O_2 states are equally sensitive to MOPS⁻. For some data points, the error bars are smaller than the symbol due to small SEM. N = 3 - 4.

3.5 Discussion

O_1 and O_2 states are two conformations with distinct pore architectures

Decades of biophysical and biochemical studies have unveiled the intricate relationship between ATP acting on CFTR's two NBDs and gate opening/closing in its TMDs (Sohma and Hwang, 2015). In short, the opening of CFTR's gate is facilitated by ATP-induced dimerization of the two NBDs (Vergani et al., 2005). Since one ATP molecule can stay bound for tens of seconds in the catalysis-incompetent site (or site 1 composed of the head subdomain of NBD1 and the tail subdomain of NBD2), each observed closing following gate opening does not require dissociation of this tightly bound ATP at the dimer interface (Tsai et al., 2009; Csanady et al., 2010; Tsai et al., 2010). Instead, closure of the channel is promoted by a partial separation of the NBD dimer following ATP hydrolysis at the catalysis-competent Site (or site 2 formed by the head subdomain of NBD2 and the tail subdomain of NBD1) (Vergani et al., 2003; Bompadre et al., 2005; But, cf.,Chaves and Gadsby, 2015). Although it remains debated if the gating cycle is strictly coupled to ATP hydrolysis cycle or not (Jih and Hwang, 2012), the molecular motion taking place in NBDs has to be transmitted to the gate in TMDs as demonstrated lately (Sorum et al., 2015).

In this paper, we have identified several mutations/chemical modifications that result in channels exhibiting two distinct single-channel conductance levels O_1 and O_2 representing respectively the pre- and post-hydrolytic open states of CFTR. Echoing our previous report (Jih and Hwang, 2012) that neutralizing the positively charged arginine at position 352 in TM6 creates channels (i.e., R352C or Q) with this characteristic behavior, here we found that introducing a negatively charged side chain to position 306 (i.e.,

N306D or E) in TM5 begets a similar O_1O_2 phenotype. As both N306 and R352 residues are located in the internal vestibule of CFTR's anion permeation pathway (Aubin and Linsdell, 2006; Bai et al., 2010; Zhang and Hwang, 2015; El Hiani et al., 2016; Zhang and Chen, 2016), our data suggest that a decrease of the number of net charge in these particular loci is important in establishing the conductance difference between the pre- and post-hydrolytic conformational states of CFTR. Furthermore, unlike R352C on TM6, the data that mutation R303C (Figure 3.8D) itself does not display the O_1O_2 phenotype suggest that in addition to the number of net charges, the location of the charge is also critical in controlling the conductance level of each open state. The O_1O_2 phenotype observed when changing the location of the endogenously charged residues along TM6 (R352) or TM5 (R303) while maintaining the same net charge together with the data in Figure 3.S2 showing that simply adding one positive charge at other pore-lining residues (MTSET$^+$ modified S307C/Cysless, F310C/Cysless and F311C/Cysless,) does not yield the O_1O_2 phenotype further confirmed the importance of the charged position in imparting this characteristic gating/permeation behavior. Collectively, these results suggest that there is a conformational change of the open channel at the TMDs upon ATP hydrolysis at the NBDs. Thus, as proposed by Ishihara and Welsh (1997), the O_1 and the O_2 states represent two distinct conformations with different pore structures even for WT channels that do not show discernible differences in the single-channel conductance. Then, what could be the conformational change upon ATP hydrolysis?

The internal vestibule expands upon O_1 to O_2 transition

While the gating motions in NBDs upon ATP binding and hydrolysis have been elucidated to some extent, our understanding of the conformational changes in TMDs

during gating is limited. Our recent studies employing SCAM suggest some rearrangements of CFTR's TMs during each gating cycle (Bai et al., 2010, 2011; Gao et al., 2013). Notably, the current study shows that manipulating the number of the net charge as well as the position of the charged residues in the internal vestibule of the pore results in channels with clear differences in single-channel conductance between the O_1 and the O_2 states. In contrast, although numerous mutations have been made on residues comprising the external vestibule or the narrow region of CFTR's pore (Zhou et al., 2008; Cui et al., 2014), none confer the O_1O_2 phenotype. We thus argue for a major conformational change in the internal vestibule of the CFTR's pore upon ATP hydrolysis.
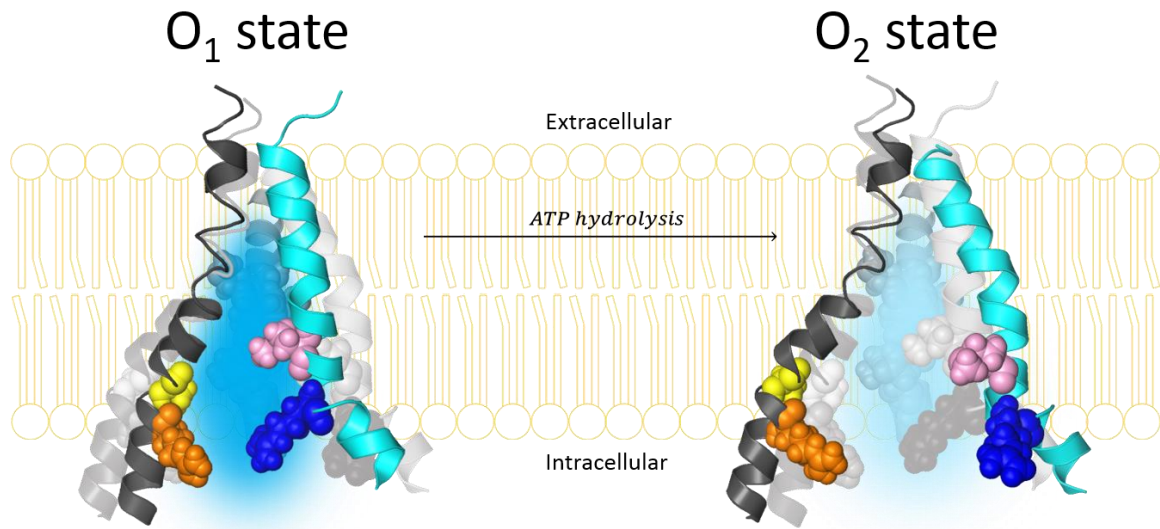
Figure 3.10. Hypothetical expansion of the internal vestibule in CFTR's pore upon ATP hydrolysis-driven O_1 to O_2 transition. TM6 (cyan), TM5 (black) and TM12 (dark gray) extracted from the homology model proposed by Dalton et al. (2012) are displayed in ribbon and rearranged purely for cosmetic purpose to illustrate a change of dimension in the internal vestibule of CFTR's pore in a cartoon style. In homology models or the cryo-EM structure of CFTR, the pore-lining TM5 and TM6 are not located at the exact opposite sides of the pore. Also, the depicted expansion of the internal vestibule by no means represents the real molecular motion during O_1 (left) to O_2 (right) transition. Pore-lining residues M348, R352, N306 and R303 are labeled in spherical illustration with the same color code applied in Figure 3.4. TM12 (dark gray) extracted from the same homology model is also displayed here along with the pore-lining residues (Bai et al., 2011) in spherical illustration. From a macroscopic point of view, as the volume of the internal vestibule increases upon transition to the O_2 state, local dielectric constant increases with the space filled with more water molecules. The electric field (both favorable and unfavorable) sensed by $MOPS^-$ is expected to dissipate more readily for the O_2 state. Differences in the local electric field between the O_1 and O_2 states subsequently result in different docking kinetic parameters for $MOPS^-$ block. To qualitatively depict the local electric field difference between the O_1 and O_2 states, we chose different densities of the positive electric field as an example (blue shadow of the internal vestibule): the darker the blue, the more positive the electric field. (Details are elaborated in Discussion and Supporting Materials).

Interestingly, compared to the open state, CFTR's closed channel conformation paradoxically assumes a wider internal entrance and perhaps a more expanded internal vestibule of the ion permeation pathway (Bai et al., 2011; Zhang and Hwang, 2015). Of note, the recently solved cryo-EM structure of zebrafish CFTR in a pre-phosphorylated closed conformation indeed shows a wide internal entrance between TM4 and TM6 (Zhang and Chen, 2016). This idea of a larger internal entrance is also consistent with the proposed molecular motions for ABC exporters, who share the evolutionary path with CFTR (Chen and Hwang, 2008; Gadsby, 2009; Rees et al., 2009). Specifically, because the NBD dimer of an ABC exporter is physically connected to its TMDs through the so-called coupling helices (Hollenstein et al., 2007), once ATP is hydrolyzed in NBDs, the separation of NBD dimer may initiate the expansion of the helix bundle forming the "internal gate"—the structural equivalent to CFTR's internal entrance of the pore—of the transporter. Since the post-hydrolytic O_2 state chronologically lies between the pre-hydrolytic O_1 state and the closed state, we propose that the geometrical dimension of the internal vestibule is smaller in the O_1 state than that of the O_2 state, if we accept the simplistic idea of a continuum of molecular motions of the internal vestibule upon transitions from open to closed states (Figure 3.10).

There are two possible consequences from the proposed smaller internal vestibule of the O_1 state: First, the residing charges are more densely packed and a smaller space of the internal vestibule containing fewer water molecules to screen the electrostatic interactions between the positively charged vestibule and inhabiting anions, in theory, could smooth down the dissipation of the electric field given out by the charged residues and subsequently magnify the electrostatic effect of charge manipulations in the internal

vestibules where the negatively charged MOPS$^-$ will be attracted to; Second, a more restricted geometry of the pore implies a closer and stronger contact between the channel wall and the residing MOPS$^-$. In the following section, we will try to use these changes in physical properties during O_1 to O_2 transition to explain the differential sensitivity to MOPS$^-$ block in mutants with the net change of charges of positive one or zero, such as WT, F311C/Cysless, A299R, and M348R/R352Q, but an equal sensitivity in mutants with a net change of charges of minus one, such as N306D and R303C. Due to limited space, here we only provide semi-quantitative explanations for these seemingly perplexing results. Readers are referred to the Supporting Materials for a more mathematical treatment of the same issue.

Amplified electrostatic effect in the O_1 state determines the differential sensitivity between the O_1 and O_2 states to MOPS$^-$ block

As a channel-impermeant blocker, MOPS$^-$ cannot penetrate deep through the narrow region of the pore due to its bulky size of 13 Å × 7 Å × 5.5 Å (Ishihara and Welsh, 1997). While Scheme 3.1 depicts the simplest model for MOPS$^-$-induced block, we prefer a three-state model (Scheme 3.2) by introducing a "docking" process representing the diffusion of MOPS$^-$ from the bulk solution into the internal vestibule before the blocker traverses deeper into CFTR's pore. In this scheme, the *O* state is the only conductive state. (See Figure 3.S3 and 3.S4 in the Supporting Materials for more extensive explanations.) Of note, this three-state blocking theme has been successfully employed to account for the blocking mechanism of CLC-0 chloride channels as well as the "ball-and-chain" inactivation mechanism of potassium channels (Zhou et al., 2001; Zhang and Chen, 2009; Zhang et al., 2009; Zhang et al., 2010).

$$O \underset{k_{off}}{\overset{[X]\ k_{on}}{\rightleftharpoons}} O_{blocked}$$

Scheme 3.1

$$O \underset{k_{-1}}{\overset{[X]k_1}{\rightleftharpoons}} O_{dock} \underset{k_{-2}}{\overset{k_2}{\rightleftharpoons}} O_{blocked}$$
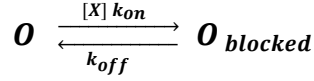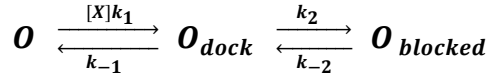
Scheme 3.2

Mathematically, Scheme 3.2 yields the following formula for quantitatively describing the fraction of unblock (F_{ub}) for the blocker MOPS⁻ (indicated as [X]):

$$F_{ub} = \frac{1}{1+\left[1+\left(\frac{k_2}{k_{-2}}\right)\right]\cdot\left(\frac{k_1\cdot[X]}{k_{-1}}\right)}$$

Equation 3.1

Being a negatively charged blocker, MOPS⁻ enters the internal vestibule of CFTR's pore through a fast diffusion-like process with the docking (k_1) and undocking (k_{-1}) rates influenced by the electrostatic potential of the internal vestibule, which in this case is partly determined by the number of the net effective charge in the internal vestibule. Then the blocker leaves the docking site and moves deeper into the internal vestibule to form a direct contact with the wall of the pore perhaps with the charged group lodged in the narrow region or the selectivity filter to account for the high voltage dependence of the blockade. The rate of this blocking step (k_2) is not only expected to be slow and partially determined by the stability of MOPS⁻ in the internal vestibule whose net charge is a deciding factor, but also determined by the geometry and chemistry of the pore. And the rate of the reverse process (k_{-2}), the presumed rate-limiting dissociation process of MOPS⁻ from the O_{block} state, is mostly determined by the direct interactions between

MOPS⁻ and the wall in the deeper part—including perhaps the selectivity filter—of the pore.

For Scheme 3.2 that includes a docking step followed by a blocking step, the proposed larger geometrical dimension in the internal vestibule of the O_2 state results in a smaller blocking constant $\left(\frac{k_2}{k_{-2}}\right)$ than that of the O_1 state because of a reduced contact between the blocker and the wall of the channel in the O_2 state (a larger k_{-2}). This blocking step is relatively insensitive to the net charge in the internal vestibule, which mainly affects the docking constant $\left(\frac{k_1 \cdot [X]}{k_{-1}}\right)$. For mutants with a net change of charges of plus one or zero in the internal vestibule that favors the docking step for MOPS⁻, the smaller dimension in the O_1 state provides a stronger electrostatic attractive force to yield a larger $\left(\frac{k_1 \cdot [X]}{k_{-1}}\right)$. Thus, mathematically the O_1 state is blocked more by MOPS⁻ than the O_2 state as both docking and blocking constants are higher for the O_1 state. In contrast, for those mutants with a net decrease of charges in the internal vestibule, e.g., N306D, and R303C/Cysless, the electrostatic potential in the internal vestibule does not favor the docking step, and this "repulsive" force is stronger in the O_1 state because of the smaller size of the internal vestibule. Thus, in a way, the larger blocking constant $\left(\frac{k_2}{k_{-2}}\right)$ for the O_1 state is effectively neutralized by the smaller docking constant $\left(\frac{k_1 \cdot [X]}{k_{-1}}\right)$ of the O_1 state for these mutants, accounting for an indistinguishable sensitivity to MOPS⁻ block between the O_1 and O_2 states. Even if there might be a small difference in the final F_{ub} between the O_1 and the O_2 state, this difference would be too small to be resolved given the reduced single-channel amplitudes for mutants with one additional negative charge. (See

Supporting Materials for detailed elaborations and a set of kinetic simulation parameters that actually fits our experimental observation.)

Normal chloride permeation requires crosstalk among multiple residues in the internal vestibule.

What has been elaborated in the last section offers a simplified—admittedly over-simplified—picture of the expansion movement in CFTR's pore upon ATP hydrolysis to explain the effects of MOPS$^-$. Now we attempt to employ the molecular insights out of the atomic structure of zebrafish CFTR (Zhang and Chen, 2016) to explain why WT channels show no obvious conductance difference between the O_1 and O_2 states when chloride ion is the charge carrier, whereas those mutations such as N306D, M348R/R352Q and F310R/R303C/Cysless do.

Unlike measuring equilibrium block by the bulky impermeant MOPS$^-$, the single-channel amplitude reflects a non-equilibrium condition when a net anion flux occurs through the pore. From the free-energy point of view, the whole ion translocation process, from entering the cytoplasmic mouth, passing along the internal vestibule, and finally penetrating through the selectivity filter, has to be energetically favored and well balanced. This process will involve the crosstalk among multiple residues from different TMs by a short-range cooperation among local residues, solvent, water molecules and other chloride ions or a long range coupling mechanism, through which the perturbation at a large distance also modifies the local free energy surface (Lauger, 1979; Berneche and Roux, 2001).

We do not know the exact details determining the free energy profile for chloride permeation in the O_1 and O_2 states. However, the aforementioned idea based on changes in the electrostatics of the internal vestibule may be also responsible for the different single-channel amplitudes seen with the O_1 and O_2 states, since this particular phenotype is conferred by a change of the charge location in TM5 or TM6. Of note, the cryo-EM structure of zebrafish CFTR suggests several candidate local charge networks in CFTR's internal vestibule. The one that draws our attention is the network between R352 (TM6) and D993 (TM9). Specifically, this network between R352 and D993 lines right at the shoulder of the internal vestibule where the internal vestibule starts to taper down to a narrower region according the cryo-EM structure (Zhang and Chen, 2016, Figure 4A). Although the cryo-EM study caught the CFTR in a pre-phosphorylated closed state, this salt bridge between R352 and D993 is likely also present in the open state (Cui et al., 2008; Jordan et al., 2008). This critical location of R352/D993 charge network in the ion permeation path may explain why the electronegative potential caused by mutation-induced subtraction of a positive charge (e.g., R352Q) decreases the single-channel conductance. Furthermore, the same electronegative potential will exert a larger effect on chloride permeation in the O_1 state with a smaller dimension as proposed in the current study, than the O_2 state (i.e., the O_1O_2 phenotype). The same concept of precise charge balance between R352 and D993 may also explain why M348R/R352Q still exhibits the O_1O_2 phenotype albeit a high single-channel conductance compared to that of R352Q; after all, M348 is farther from D993 than R352 (Figure 3.4B). This idea of balanced local charge network also leads us to reason that the characteristic O_1O_2 phenotype seen in N306D and N306E mutants is caused by a disruption of the same network, as N306 is

located in the vicinity of R352 and D993 with the following distances in between: 12.7 Å (R352 and N306), 12.2 Å (N306 and D993) and 14.8 Å (D993 and R352) (Zhang and Chen, 2016, Figure 4C). This hypothesis predicts a superposition of electric fields produced by the charges at D306 and D993. Consistent with this idea, neutralizing D993 under the N306D background (N306D/D993N, Figure 3.S5) increases the single-channel amplitudes of both O_1 and O_2 states and decreases the difference in single-channel amplitude between these two states.

How moving the endogenous positive charge at position 303 along TM5 confers the O_1O_2 phenotype is a more difficult question to answer, since neutralization of R303, though does decrease the single-channel conductance, fails to yield different open states. Interestingly, however, the cryo-EM structure of CFTR does reveal several charged amino acids near R303: R248 (12.5 Å), R251 (15.4 Å), D985 (11.7 Å), D984 (14.5 Å) (Zhang and Chen, 2016). In addition, contrary to the positions of R352 and D993 where the internal vestibule starts to taper down to the narrow region of the pore, R303 is positioned more cytoplasmically in the more spacious region of the internal vestibule (Figure 3.4B). Perhaps a wider space lessens the electrostatic effect of dimensional changes during O_1 to O_2 transition. Furthermore, as different regions of the internal vestibule show different charge distributions as well as physical contours (Figure 3.4B, Zhang and Chen, 2016), it seems not surprising that perturbations of local electrostatics may exhibit different O_1O_2 phenotypes (Figure 3.1, 3.2, 3.3, 3.5, 3.S5 and 3.S6).

In short, we speculate that a detailed balance of the charge network between R352 and D993 (and likely also other charge networks), which the permeating chloride will

encounter at a fairly narrow region of the pore, accounts for a lack of the O_1O_2 phenotype in WT channels. On the contrary, once this charge network is perturbed by mutations and/or chemical modifications, the unbalanced electrostatic potential profile in this region will exert effects on the incoming/exiting chloride ions. Just like the mechanism we have elaborated for $MOPS^-$ block, the magnitude of this electrostatic effect will depend on the physical dimension of the internal vestibule. Once the atomic structure of CFTR's open state is solved, one can start to explore the biophysical function of charged networks in chloride permeation through CFTR.

The coupling mechanism of CFTR gating and the conformational changes during gating transitions are among the most interesting topics in the CFTR field. Apparently many more experiments are needed to bequeath us a deeper understanding of this subject. Although we may be still far from getting a close glimpse of the crystal structure of CFTR, the current study provides insights into the role of charged residues and their positions in determining anion permeation in the pore of CFTR. Furthermore, a larger toolbox for the mechanistic studies of CFTR gating by ATP hydrolysis is now becoming available.

3.6 Supporting Materials
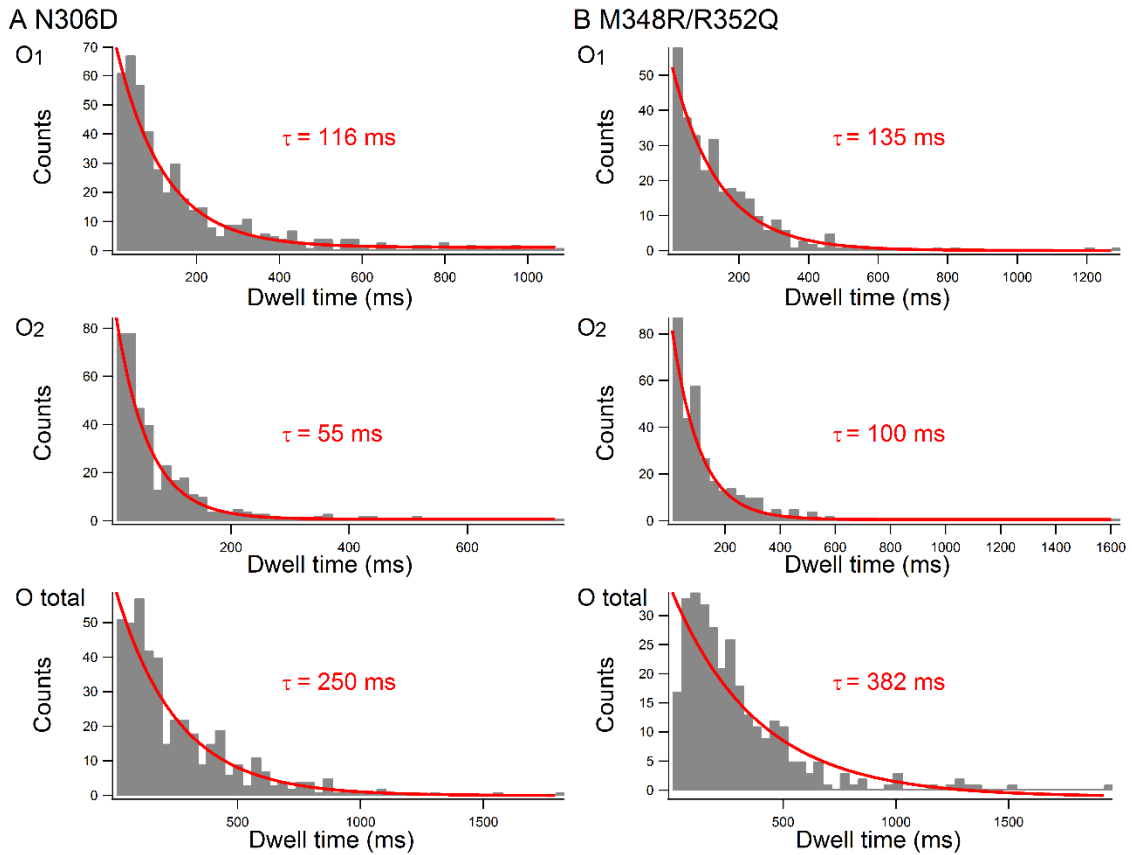
Figure 3.S1. Dwell-time histograms for O_1 state, O_2 states and opening burst in N306D (panel A) and M348R/R352Q (panel B). All histograms can be fitted well with a single-exponential function (time constants indicated). As the time constants for the O_2 state are several fold larger than the 8-ms cutoff used to identify a state, missed events are not a major problem in our statistical analysis of the gating topology.
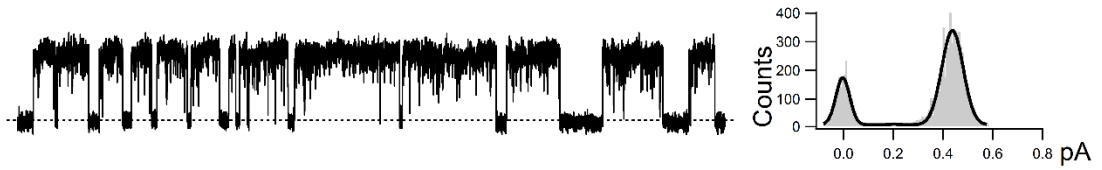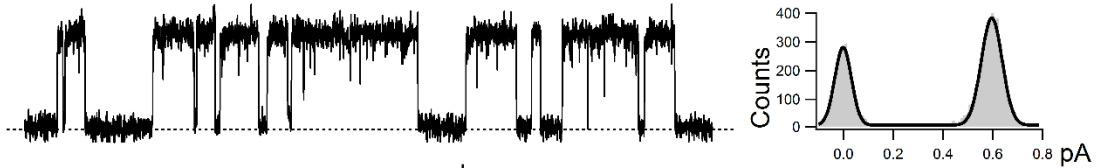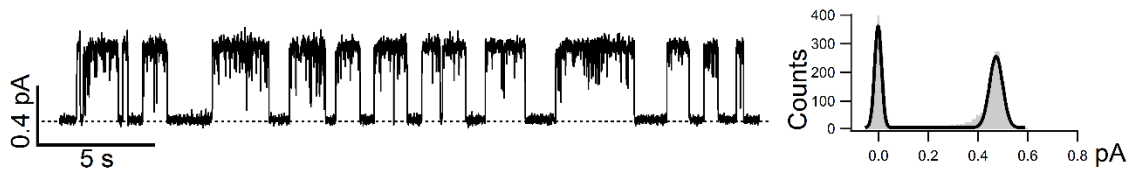
Figure 3.S2. S307C/Cysless (panel A), F310C/Cysless (panel B) and F311C/Cysless (panel C)

modified by MTSET+ show only one single-channel conductance level. Each all-point histogram of the open-channel level can be fitted with a single Gaussian function. Compared with Figure 3.5, the data here suggest that adding one additional positive charge at the S307 or F3110 or F311 doesn't not yield the O_1O_2 phenotype; the simultaneous neutralization of R303 is also required for the presence of the O_1O_2 phenotype, supporting the critical role of the position of charges in determining the O_1O_2 phenotype.
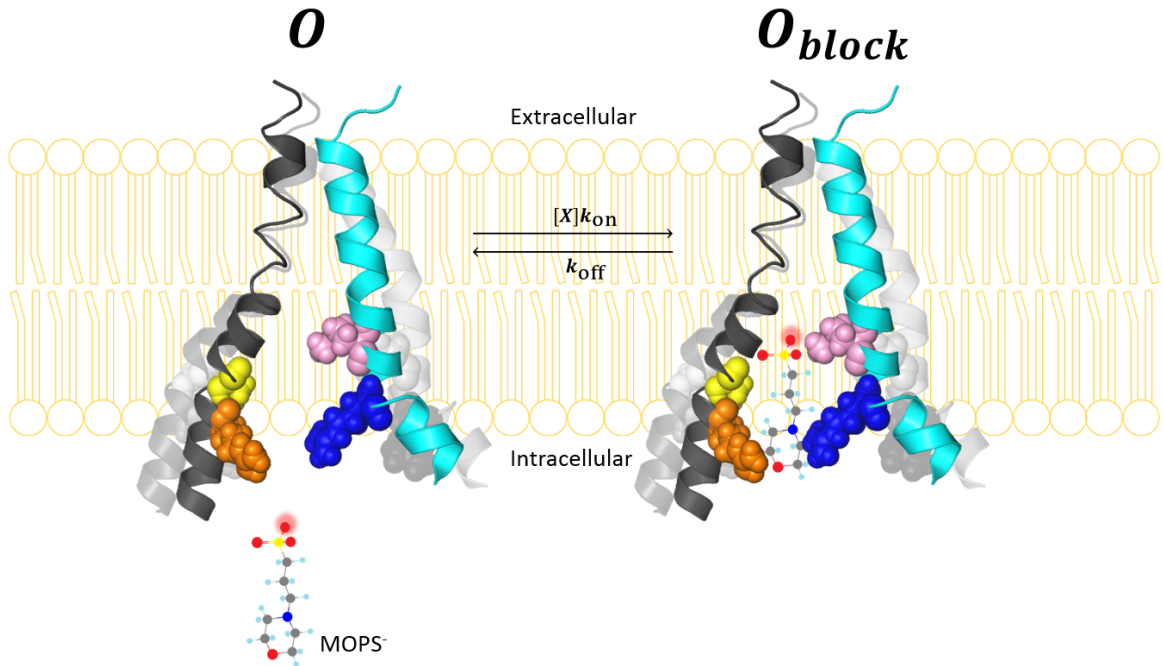
Figure 3.S3. Two-state model for differential MOPS⁻ block between the O_1 and O_2 states. Color code is the same as that in Figure 3.10. The negative head of MOPS⁻ is highlighted with red shadow. The transmembrane segments in this figure and Figure 3.S4 are extracted from the homology model published by Dalton et al. (2012). The mechanism behind the charge-dependent differential sensitivities of O_1 state and O_2 state to the application of channel-impermeant blocker MOPS⁻ can be explained by a simple canonical one-step blocking scheme.

$$O \underset{k_{off}}{\overset{[X]\,k_{on}}{\rightleftharpoons}} O_{blocked}$$
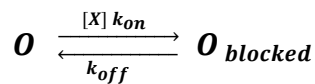
Scheme 3.1

$$F_{ub} = \frac{1}{1 + \left(\dfrac{k_{on}}{k_{off}}\right)[X]}$$

Equation 3.S1

According to Scheme 3.1, the fraction of unblock is calculated with **Equation 3.S1**, where [X] represents the concentration of MOPS⁻. For this two-state model, the binding

constant $\left(\frac{k_{on}}{k_{off}}\right)$ is the sole determinant deciding the degree of block at a fixed

concentration of MOPS⁻. Therefore, for the mutants with a net charge unaltered (0) or

positive one (1), as long as this ratio $\left(\frac{k_{on}}{k_{off}}\right)$ is larger for the O_1 state than that of the O_2

state, the O_1 state will be more sensitive to MOPS⁻ block. One can propose that an

expansion of the internal vestibule during O_1 to O_2 transition decreases the electrostatic

attraction of the pore for MOPS⁻, and hence less blockade for the O_2 state. However, for

the mutants with a net charge of minus one (-1), volume expansion during O_1 to O_2

transition will decrease the electrostatic "repulsion", resulting in a larger $\left(\frac{k_{on}}{k_{off}}\right)$ for the O_2

state, compared with that of the O_1 state. At first glance, this prediction contradicts our

experimental observation that O_1 and O_2 exhibit equal sensitivity to MOPS⁻ for these

mutants. But if we consider that for mutants with a net charge of minus one, the binding

constants $\left(\frac{k_{on}}{k_{off}}\right)$ for both the O_1 and O_2 states are much smaller than those of WT so that

the difference in F_{ub} between the O_1 and O_2 states is too small to be resolved given a

dramatic reduction of the single-channel amplitudes of both states (Figure 3.2 and 3.8D),

we can still find proper parameters to fit our data with Scheme 3.1. However, this model

lacks the physical details describing the assigned parameters and is oversimplified for not

considering the direct contact interaction between MOPS⁻ and the wall of the pore.

Furthermore, Scheme 3.1 also implies that the blocking site for MOPS⁻ is in the internal

vestibule. However, the generally held view of a wide space in the internal vestibule

argues against a high voltage dependence of the block observed experimentally. After

some reckoning, we decided to add one nonconductive docked state for MOPS⁻ block

(Scheme 3.2 and Figure 3.S4).
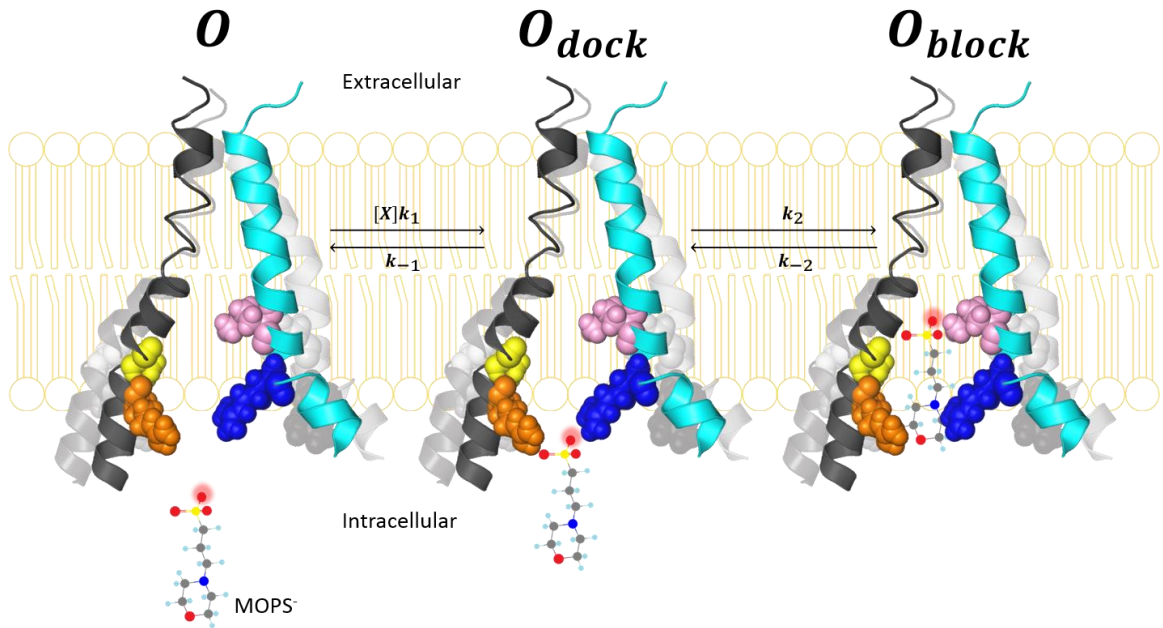
Figure 3.S4. Three-state model for MOPS⁻ block. Color code is the same as that in Figure 3.10.

To better explain our data with MOPS⁻, a "docking" step was introduced into Scheme 3.1 to derive Scheme 3.2:

$$O \; \underset{k_{-1}}{\overset{[X]k_1}{\rightleftarrows}} \; O_{dock} \; \underset{k_{-2}}{\overset{k_2}{\rightleftarrows}} \; O_{block}$$

Scheme 3.2

This two-step blocking model is based on the following ideas: First, previous studies using gigantic probes (Zhou et al., 2002; Bai et al., 2011) suggest a wide the internal vestibule in CFTR'S pore. Thus, if the final destiny for MOPS⁻ is in this vestibule, the block should not show such high voltage dependence (Figure 3.8) that implicates a residence of the charged head of MOPS⁻ in a region exhibiting a large voltage drop. Second, the observation that charge manipulations in the internal vestibule do affect MOPS⁻ block suggests an involvement of the electric field of the internal vestibule in determining MOPS⁻ block. Third, that part of MOPS⁻ may be lodged in the deeper part of

125

the internal vestibule is supported by the observation that the F311C mutation, closest

pore-lining residue to the narrow region of the CFTR's pore on TM5 from cytoplasmic

side, increases MOPS⁻ block (Figure 3.8 and 3.9). Fourth, this two-step blocking scheme

has been successfully used to explain the block of CLC-0 chloride channels by organic

anions (Zhang and Chen, 2009; Zhang et al., 2009)

The fraction of block based on Scheme 3.2 is described with Equation 3.1:

$$F_{ub} = \frac{1}{1 + \left[1 + \left(\frac{k_2}{k_{-2}}\right)\right] \cdot \left(\frac{k_1 \cdot [X]}{k_{-1}}\right)}$$

Equation 3.1

Based on this two-step model, kinetic simulations were conducted. One set of parameters

that can quantitatively explain the differential responses of our mutants to MOPS⁻ block

are presented in Figure 3.TS1. Of note, these parameters represent simply one example of

results that successfully describe the experimental data from each of the mutation

categories. Different sets of parameters can also successfully fit our data as long as

$\left(\frac{k_1}{k_{-1}}\right)[X]$ and $\left(\frac{k_2}{k_{-2}}\right)$ are not changed drastically.
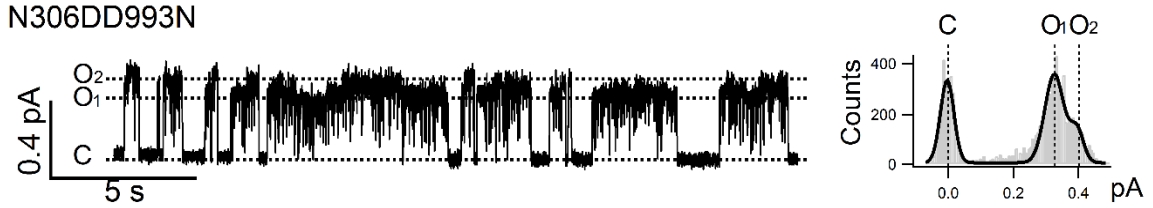
Figure 3.S5. Neutralization of D993 affects the O_1O_2 phenotype in N306D. A representative single-channel trace (left) shows the double mutant N306D/D993N displaying two distinct open-channel current amplitudes: O_1 (0.32 ±0.01 pA, N = 3) and O_2 (0.39 ± 0.01 pA, N = 3). Corresponding all-points histogram (right) barely shows an additional peak to the right of the main peak of the O_1 state. Compared with the single mutant N306D (O_1: 0.18 ± 0.01, N = 3 and O_2: 0.24 ± 0.01, N = 3), neutralizing the aspartate at position 993 under the N306D background increases the single-channel amplitudes of both O_1 and O_2 states but decreases the relative difference in single-channel amplitude between these two states as if D306 can partially replace the function of D993. These results are consistent with the idea that there's a superposition of electric fields produced by the charge at positions 306 and 993 presumably because of a physical proximity.

A S307RR303C/Cysless modified by MTSES⁻

B

C A299RR303C/Cysless modified by MTSET⁺

D

128
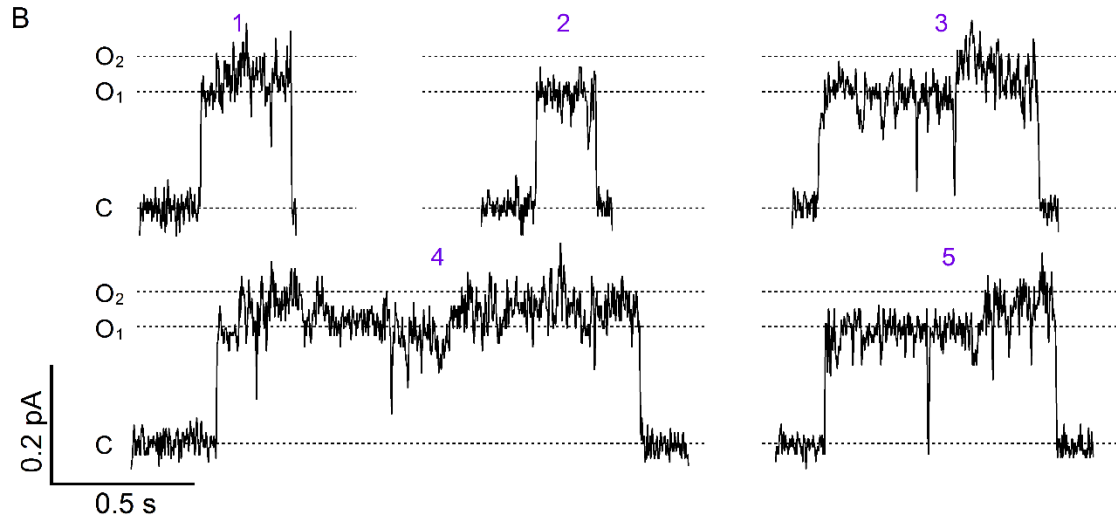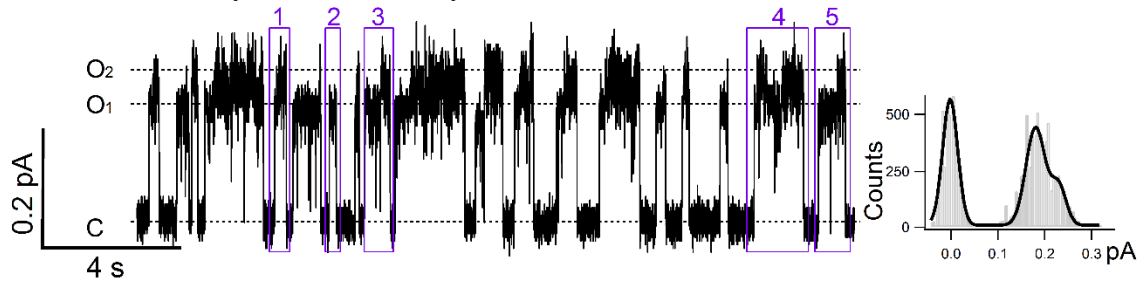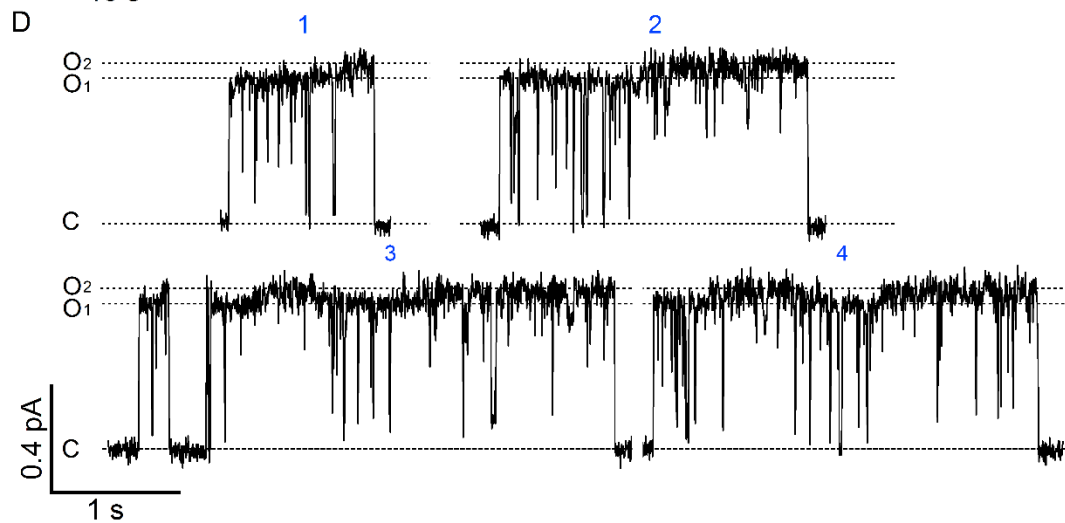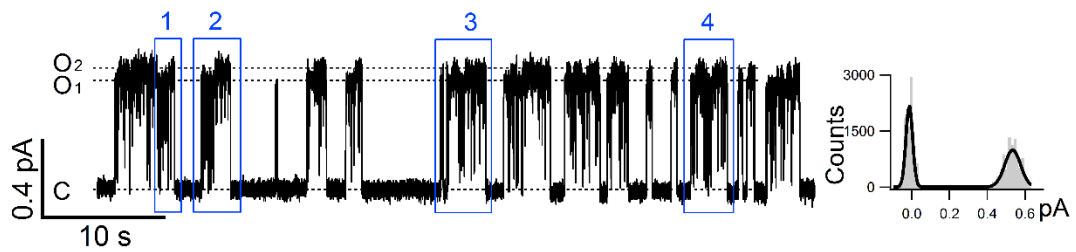
Figure 3.S6. Modification of S307R/R303C/Cysless and A299R/R303C/Cysless changes their phenotype. A. S307R/R303C/Cysless modified by negatively charged thiol-specific reagent MTSES⁻ displays clear O_1O_2 phenotype (O_1: 0.17 ± 0.01, N = 3 and O_2: 0.23 ± 0.01, N = 3) whereas the S307R/R303C/Cysless itself (Figure 3.5A) does not show clear difference in single-channel amplitudes between its O_1 and O_2 states. **B.** Expanded bursts marked in panel **A** show details of each opening burst and the preferred gating transition of C→O_1→O_2→C for bursts 3, 4 and 5. The single-channel behaviors of S307R/R303C/Cysless before (Figure 3.5) and after MTSES⁻ modification support the ideas that ion permeation through the internal vestibule of CFTR's pore has to be delicately tuned through the cooperation among multiple pore-lining residues placed at each specific locations such as 303, 306, 307, 352, 348, and that the functional perturbations caused by mutations at these positions are amplified in the O_1 state resulting in the O_1O_2 phenotype. **C.** A299R/R303C/Cysless modified by positively charged thiol-specific reagent MTSET⁺ displays clear O_1O_2 phenotype although with small difference between two open states (O_1: 0.47 ± 0.02, N = 4 and O_2: 0.52 ± 0.02, N = 4). **D.** Expanded bursts marked in **C** show details of O_1 to O_2 transitions.

Net charge	State	$[X]\cdot k_1$	k_{-1}	k_2	k_{-2}	F_{ub}
0, +1 (WT, A299R,	O_1	100000	120000	200	50	0.19
F311C/Cysless)	O_2	80000	140000	300	200	0.41
-1 (N306D,	O_1	40000	600000	400	50	0.63
R303C/Cysless)	O_2	50000	400000	600	200	0.67
Electro-positivity order in the internal vestibule (from positive of negative): $$O_{1(0,+1)} > O_{2(0,+1)} > O_{2(-1)} > O_{1(-1)}$$						
Order of $[X]\cdot k_1$: $O_{1(0,+1)} > O_{2(0,+1)} > O_{2(-1)} > O_{1(-1)}$						
Order of k_{-1} : $O_{1(0,+1)} < O_{2(0,+1)} < O_{2(-1)} < O_{1(-1)}$						
So that the order of $[X]\cdot k_1/k_{-1}$: $O_{1(0,+1)} > O_{2(0,+1)} \gg O_{2(-1)} > O_{1(-1)}$						

Figure 3.TS1 A set of kinetic parameters simulating the two-step model of MOPS$^-$ block.

 Importantly, this two-step model of MOPS$^-$ block (Scheme 2) can not only

quantitatively explain our experimental data through simulations (Figure 3.TS1), but also

give each parameter its physical meaning, the change of which is accountable by our

hypothetic molecular motions of the pore during O_1 to O_2 transition. As described in the

main text, we propose an expansion of the internal vestibule as part of the conformational

changes from O_1 to O_2 state upon ATP hydrolysis. This expansion could in theory

weaken the interaction between MOPS$^-$ and the wall of the pore at its blocking site; hence

$k_{-2\,(O2)} \gg k_{-2\,(O1)}$. On the other hand, k_2 is not as sensitive to the size of the pore; hence k_2

$_{(O2)} > k_{2\,(O1)}$. For the docking rate constants, k_1 and k_{-1}, since the docking step reflects

diffusion of MOPS$^-$ back and forth between the bulk solution and the internal vestibule,

its kinetic constant must be several orders of magnitude higher than those of the blocking

step (i.e., k_2 and k_{-2}). However, the exact values of k_1 and k_{-1} will be a function of the

electric potential in the internal vestibule: higher k_1 and lower k_{-1} for a favorable potential (0 and +1 in Figure 3.TS1) relative to the corresponding parameters in an unfavorable condition (-1 in Figure 3.TS1). Finally, the smaller size of the internal vestibule at the O_1 state will amplify both the favorable and the unfavorable electric potential; for the former, $k_{1\,(O1)} > k_{1\,(O2)}$, $k_{-1\,(O1)} < k_{-1\,(O2)}$; for the latter, the reverse order or $k_{1\,(O1)} < k_{1\,(O2)}$, $k_{-1\,(O1)} > k_{-1\,(O2)}$.

In short, Scheme 3.2 (or Equation 3.1) predicts that the degree of MOPS$^-$ block is decided by both docking kinetics (k_1 and k_{-1}) and blocking kinetics (k_2 and k_{-2}). When the electric potential in the internal vestibule is favorable for MOPS$^-$ to dock (0 and +1 in Figure 3.TS1), both docking and blocking are favored in the O_1 state (and hence a higher degree of block). In contrast, when the electric potential in the internal vestibule is unfavorable for docking of MOPS$^-$ (-1 in Figure 3.TS1), this disfavored electric potential is exaggerated in the O_1 state and the resulting dampened docking kinetics effectively cancels out the favorable blocking kinetics of the O_1 state.

3.7 References

Aubin, C.N., and P. Linsdell. 2006. Positive charges at the intracellular mouth of the pore regulate anion conduction in the CFTR chloride channel. *The Journal of general physiology*. 128:535-545.

Bai, Y., M. Li, and T.C. Hwang. 2010. Dual roles of the sixth transmembrane segment of the CFTR chloride channel in gating and permeation. *The Journal of general physiology*. 136:293-309.

Bai, Y., M. Li, and T.C. Hwang. 2011. Structural basis for the channel function of a degraded ABC transporter, CFTR (ABCC7). *The Journal of general physiology*. 138:495-507.

Bear, C.E., C.H. Li, N. Kartner, R.J. Bridges, T.J. Jensen, M. Ramjeesingh, and J.R. Riordan. 1992. Purification and functional reconstitution of the cystic fibrosis transmembrane conductance regulator (CFTR). *Cell*. 68:809-818.

Berneche, S., and B. Roux. 2001. Energetics of ion conduction through the K+ channel. *Nature*. 414:73-77.

Bompadre, S.G., J.H. Cho, X. Wang, X. Zou, Y. Sohma, M. Li, and T.C. Hwang. 2005. CFTR gating II: Effects of nucleotide binding on the stability of open states. *The Journal of general physiology*. 125:377-394.

Bozoky, Z., M. Krzeminski, R. Muhandiram, J.R. Birtley, A. Al-Zahrani, P.J. Thomas, R.A. Frizzell, R.C. Ford, and J.D. Forman-Kay. 2013. Regulatory R region of the CFTR chloride channel is a dynamic integrator of phospho-dependent intra- and

intermolecular interactions. *Proceedings of the National Academy of Sciences of the United States of America*. 110:E4427-4436.

Chaves, L.A., and D.C. Gadsby. 2015. Cysteine accessibility probes timing and extent of NBD separation along the dimer interface in gating CFTR channels. *The Journal of general physiology*. 145:261-283.

Chen, T.Y., and T.C. Hwang. 2008. CLC-0 and CFTR: Chloride Channels Evolved From Transporters. *Physiological reviews*. 88:351-387.

Csanady, L., P. Vergani, and D.C. Gadsby. 2010. Strict coupling between CFTR's catalytic cycle and gating of its Cl- ion pore revealed by distributions of open channel burst durations. *Proceedings of the National Academy of Sciences of the United States of America*. 107:1241-1246.

Cui, G., K.S. Rahman, D.T. Infield, C. Kuang, C.Z. Prince, and N.A. McCarty. 2014. Three charged amino acids in extracellular loop 1 are involved in maintaining the outer pore architecture of CFTR. *The Journal of general physiology*. 144:159-179.

Cui, G., Z.R. Zhang, A.R. O'Brien, B. Song, and N.A. McCarty. 2008. Mutations at arginine 352 alter the pore architecture of CFTR. *The Journal of membrane biology*. 222:91-106.

Dalton, J., O. Kalid, M. Schushan, N. Ben-Tal, and J. Villa-Freixa. 2012. New model of cystic fibrosis transmembrane conductance regulator proposes active channel-like conformation. *Journal of chemical information and modeling*. 52:1842-1853.

Davidson, A.L., and P.C. Maloney. 2007. ABC transporters: how small machines do a big job. *Trends in Microbiology*. 15:448-455.

El Hiani, Y., and P. Linsdell. 2012. Tuning of CFTR chloride channel function by location of positive charges within the pore. *Biophys J*. 103:1719-1726.

El Hiani, Y., A. Negoda, and P. Linsdell. 2016. Cytoplasmic pathway followed by chloride ions to enter the CFTR channel pore. *Cellular and molecular life sciences : CMLS*. 73:1917-1925.

Gadsby, D.C. 2009. Ion channels versus ion pumps: the principal difference, in principle. *Nature reviews. Molecular cell biology*. 10:344-352.

Gadsby, D.C., P. Vergani, and L. Csanády. 2006. The ABC protein turned chloride channel whose failure causes cystic fibrosis. *Nature*. 440:477-483.

Gao, X., Y. Bai, and T.C. Hwang. 2013. Cysteine scanning of CFTR's first transmembrane segment reveals its plausible roles in gating and permeation. *Biophys J*. 104:786-797.

Gunderson, K.L., and R.R. Kopito. 1995. Conformational states of CFTR associated with channel gating: the role ATP binding and hydrolysis. *Cell*. 82:231-239.

Higgins, C.F., and K.J. Linton. 2004. The ATP switch model for ABC transporters. *Nature Structural & Molecular Biology*. 11:918-926.

Hollenstein, K., R.J.P. Dawson, and K.P. Locher. 2007. Structure and mechanism of ABC transporter proteins. *Current Opinion in Structural Biology*. 17:412-418.

Hwang, T.C., and K.L. Kirk. 2013. The CFTR ion channel: gating, regulation, and anion permeation. *Cold Spring Harbor perspectives in medicine*. 3:a009498.

Hwang, T.C., and D.N. Sheppard. 2009. Gating of the CFTR Cl- channel by ATP-driven nucleotide-binding domain dimerisation. *The Journal of physiology*. 587:2151-2161.

Ishihara, H., and M.J. Welsh. 1997. Block by MOPS reveals a conformation change in the CFTR pore produced by ATP hydrolysis. *The American journal of physiology*. 273:C1278-1289.

Jih, K.Y., and T.C. Hwang. 2012. Nonequilibrium gating of CFTR on an equilibrium theme. *Physiology*. 27:351-361.

Jih, K.Y., Y. Sohma, and T.C. Hwang. 2012. Nonintegral stoichiometry in CFTR gating revealed by a pore-lining mutation. *The Journal of general physiology*. 140:347-359.

Jordan, I.K., K.C. Kota, G. Cui, C.H. Thompson, and N.A. McCarty. 2008. Evolutionary and functional divergence between the cystic fibrosis transmembrane conductance regulator and related ATP-binding cassette transporters. *Proceedings of the National Academy of Sciences of the United States of America*. 105:18865-18870.

Kathawala, R.J., P. Gupta, C.R. Ashby, Jr., and Z.S. Chen. 2015. The modulation of ABC transporter-mediated multidrug resistance in cancer: a review of the past decade. *Drug Resist Updat*. 18:1-17.

Lauger, P. 1979. A channel mechanism for electrogenic ion pumps. *Biochimica et biophysica acta*. 552:143-161.

Li, Y., W.-P. Yu, C.-W. Lin, and T.-Y. Chen. 2005. Oxidation and Reduction Control of the Inactivation Gating of Torpedo ClC-0 Chloride Channels. *Biophysical Journal*. 88:3936-3945.

Liu, X., C. Alexander, J. Serrano, E. Borg, and D.C. Dawson. 2006. Variable Reactivity of an Engineered Cysteine at Position 338 in Cystic Fibrosis Transmembrane Conductance Regulator Reflects Different Chemical States of the Thiol. *Journal of Biological Chemistry*. 281:8275-8285.

Locher, K.P. 2009. Structure and mechanism of ATP-binding cassette transporters. *Philosophical Transactions of the Royal Society B: Biological Sciences*. 364:239-245.

Mornon, J.P., B. Hoffmann, S. Jonic, P. Lehn, and I. Callebaut. 2015. Full-open and closed CFTR channels, with lateral tunnels from the cytoplasm and an alternative position of the F508 region, as revealed by molecular dynamics. *Cellular and molecular life sciences : CMLS*. 72:1377-1403.

Oldham, M.L., A.L. Davidson, and J. Chen. 2008. Structural insights into ABC transporter mechanism. *Current Opinion in Structural Biology*. 18:726-733.

Ostedgaard, L.S., O. Baldursson, D.W. Vermeer, M.J. Welsh, and A.D. Robertson. 2000. A functional R domain from cystic fibrosis transmembrane conductance regulator is predominantly unstructured in solution. *Proceedings of the National Academy of Sciences of the United States of America*. 97:5657-5662.

Ostedgaard, L.S., O. Baldursson, and M.J. Welsh. 2001. Regulation of the Cystic Fibrosis Transmembrane Conductance Regulator Cl- Channel by Its R Domain. *Journal of Biological Chemistry*. 276:7689-7692.

Rees, D.C., E. Johnson, and O. Lewinson. 2009. ABC transporters: the power to change. *Nature Reviews Molecular Cell Biology*. 10:218-227.

Riordan, J.R., J.M. Rommens, B. Kerem, N. Alon, R. Rozmahel, Z. Grzelczak, J. Zielenski, S. Lok, N. Plavsic, J.L. Chou, and et al. 1989. Identification of the cystic fibrosis gene: cloning and characterization of complementary DNA. *Science*. 245:1066-1073.

Sohma, Y., and T.C. Hwang. 2015. Cystic fibrosis and the CFTR anion channel. *In* Handbook of Ion Channels. Taylor & Francis Group, LLC. Boca Taton. FL. 627.

Sorum, B., D. Czege, and L. Csanady. 2015. Timing of CFTR Pore Opening and Structure of Its Transition State. *Cell*. 163:724-733.

Tsai, M.F., M. Li, and T.C. Hwang. 2010. Stable ATP binding mediated by a partial NBD dimer of the CFTR chloride channel. *The Journal of general physiology*. 135:399-414.

Tsai, M.F., H. Shimizu, Y. Sohma, M. Li, and T.C. Hwang. 2009. State-dependent modulation of CFTR gating by pyrophosphate. *The Journal of general physiology*. 133:405-419.

Vergani, P., S.W. Lockless, A.C. Nairn, and D.C. Gadsby. 2005. CFTR channel opening

    by ATP-driven tight dimerization of its nucleotide-binding domains. *Nature*.

    433:876-880.

Vergani, P., A.C. Nairn, and D.C. Gadsby. 2003. On the mechanism of MgATP-

    dependent gating of CFTR Cl- channels. *The Journal of general physiology*.

    121:17-36.

Zhang, J., and T.C. Hwang. 2015. The Fifth Transmembrane Segment of Cystic Fibrosis

    Transmembrane Conductance Regulator Contributes to Its Anion Permeation

    Pathway. *Biochemistry*. 54:3839-3850.

Zhang, X.D., and T.Y. Chen. 2009. Amphiphilic Blockers Punch through a Mutant CLC-

    0 Pore. *The Journal of general physiology*. 133:59-68.

Zhang, X.D., P.Y. Tseng, W.P. Yu, and T.Y. Chen. 2009. Blocking Pore-open Mutants of

    CLC-0 by Amphiphilic Blockers. *The Journal of general physiology*. 133:43-58.

Zhang, X.D., W.P. Yu, and T.Y. Chen. 2010. Accessibility of the CLC-0 pore to charged

    methanethiosulfonate reagents. *Biophys J*. 98:377-385.

Zhang, Z., and J. Chen. 2016. Atomic Structure of the Cystic Fibrosis Transmembrane

    Conductance Regulator. *Cell*. 167:1586-1597 e1589.

Zhou, J.J., M. Fatehi, and P. Linsdell. 2008. Identification of positive charges situated at

    the outer mouth of the CFTR chloride channel pore. *Pflugers Archiv : European

    journal of physiology*. 457:351-360.

Zhou, J.J., M.S. Li, J. Qi, and P. Linsdell. 2010. Regulation of conductance by the number of fixed positive charges in the intracellular vestibule of the CFTR chloride channel pore. *The Journal of general physiology*. 135:229-245.

Zhou, J.J., and P. Linsdell. 2007. Molecular mechanism of arachidonic acid inhibition of the CFTR chloride channel. *European journal of pharmacology*. 563:88-91.

Zhou, M., J.H. Morais-Cabral, S. Mann, and R. MacKinnon. 2001. Potassium channel receptor site for the inactivation gate and quaternary amine inhibitors. *Nature*. 411:657-661.

Zhou, Z., S. Hu, and T.C. Hwang. 2002. Probing an open CFTR pore with organic anion blockers. *The Journal of general physiology*. 120:647-662.

CHAPTER 4

Mechanistic insights revealed from unexpected functional properties of zebrafish CFTR

This chapter has been adapted from a manuscript that will be submitted by Jingyao Zhang, Jiunn-Tyng Yeh, Han-I Yeh and Tzyh-Chang Hwang in July, 2018.

Right after I published my second article (Chapter 3) that reveals the subtle electrostatic tuning and conformational changes of CFTR's pore within an open channel burst, the ground-breaking cryo-EM structure of unphosphorylated zebrafish CFTR was published (Zhang and Chen, 2016). This cryo-EM structure is highly consistent with the data of the pore-lining residues we published (Zhang and Hwang, 2015, 2017). However, our data unraveling the electrostatic tuning of the pore also highlight that subtle structural differences, such as site mutations or charge manipulations may result in obvious, if not dramatic, functional differences in gating or permeation properties. Thus, although zebrafish CFTR shares 55% sequence identity with human CFTR, without solid functional data of zebrafish CFTR, it is unsafe to conclude that zebrafish CFTR also shares large functional similarity with human CFTR. This lack of zebrafish CFTR functional data severely restricts the utilization and interpretation of the high-resolution zebrafish CFTR structure to globally interpret the large amount of human CFTR structural/functional data for novel insights. Thus at this very time point with the first high-resolution (zebrafish) CFTR structure available, a thorough functional characterization of zebrafish CFTR becomes urgent and is conducted and elaborated in this chapter.

4.1 Abstract:

CFTR, the culprit behind the genetic disease cystic fibrosis, is a phosphorylation-activated, but ATP-gated anion channel. Copious biochemical/biophysical studies of human CFTR over the past two decades have provided an in-depth understanding of how CFTR works as an ion channel despite its structural resemblance to ABC transporters, whereas recently-solved cryo-EM structures of unphosphorylated human and zebrafish CFTR (hCFTR and zCFTR), as well as phosphorylated ATP-bound zebrafish CFTR offer an unprecedented opportunity to understand CFTR's function at a molecular level. Interestingly, despite millions of years of phylogenetic distance between human and zebrafish, the structures of unphosphorylated zCFTR and hCFTR exhibit remarkable similarities. These two orthologs also assume a similar ATP hydrolysis rate (0.37 $s^{-}1$ for hCFTR; 0.66 s^{-1} for zCFTR). In the current study, we characterized biophysical and pharmacological properties of zCFTR with the patch-clamp technique, and showed surprisingly very different functional properties between these two orthologs. First, while hCFTR has a single-channel conductance of ~8 pS with a linear I-V curve, zCFTR shows an inwardly-rectified I-V relationship with a single-channel conductance < 4 pS. Second, single-channel gating behaviors of phosphorylated zCFTR are very different from those of hCFTR, featuring a very low P_o (0.03 ± 0.02, vs ~0.50 fo hCFTR) with an exceedingly long interburst duration (~3 s vs ~480 ms for hCFTR). In addition, unlike hCFTR where each open burst is clearly defined with few sort-lived flickery closures, the open bursts of zCFTR are interrupted by clearly resolvable closed events. Third, the responses of zCFTR to ATP analogs such as 2'-deoxy-ATP and N^6-phenylethyl ATP, phosphate analog pyrophosphate and gating inhibitor $CFTR_{inh}$-172 are also distinctly different from

that of hCFTR. Lastly, although abolishing ATP hydrolysis by replacing the catalytic glutamate with glutamine (i.e., E1372Q) drastically prolongs the open bursts in zCFTR, the P_o within a lock-open burst of E1372Q-zCFTR is only ~ 0.35 (vs. P_o > 0.94 in E1371Q-hCFTR). This latter result suffices to account for the unexpected closed-state structure of phosphorylated E1372Q-zCFTR that is equipped with a canonical ATP-bound dimer of the nucleotide binding domains (NBDs). Moreover, two new insights into the molecular mechanism of CFTR gating emerge: First, the data that zCFTR and hCFTR exhibit very different gating kinetics but similar ATP hydrolysis rate suggest that, contrary to conventional thinking, the closed state of zCFTR can hydrolyze ATP. Second, since ATP hydrolysis for ABC transporters occurs at the NBD dimer interface, this hydrolysis-competent closed state may resemble the cryo-EM structure of the closed conformation of zCFTR with dimerized NBDs. Collectively, these high temporal resolution functional data of zCFTR, when interpreted in the context of high spatial resolution structures, could definitively shed new light on the molecular mechanism of this medically important protein.

4.2 Introduction

As a major breakthrough in cystic fibrosis research, three high-resolution cryo-EM structures of CFTR (unphosphorylated human and zebrafish CFTR, and phosphorylated ATP-bound zebrafish CFTR) were published recently (Zhang and Chen, 2016; Liu et al., 2017; Zhang et al., 2017). These structures have provided not only unprecedented insights for the interpretations of functional data accumulated over the years, but also exquisite guides for future structural and functional interrogations of CFTR. Consistent

with the basic architecture of CFTR proposed since the identification of the *cftr* gene (Riordan et al., 1989), all three structures show two Transmembrane Domain (TMD) - Nucleotide Binding Domain (NBD) complexes, linked by a disordered Regulatory Domain (RD) mostly unresolved with the cryo-EM technique. These structures support a model established previously for CFTR function as an ion channel (Welsh et al., 1992; McCarty, 2000; Gadsby, 2009; Hwang and Sheppard, 2009; Martin et al., 2018): After multiple serines/threonines in RD are phosphorylated by Protein Kinase A (PKA), ATP molecules, serving as a molecular glue, join two NBDs together to form a tight head-to-tail NBD dimer. This NBD dimerization is coupled to the opening of the gate in the TMDs (Vergani et al., 2005). Specifically, the unphosphorylated apo-forms of human and zebrafish CFTR (hCFTR and zCFTR respectively) show two widely separated NBDs and an anion permeation pathway crafted by the TMDs with a closed external gate (Zhang and Chen, 2016; Liu et al., 2017). Detailed comparisons of the structures of these two CFTR orthologs show remarkable similarities between zCFTR and hCFTR at a molecular level, despite a far-flung evolutionary distance and divergent living environments between these two species (Bose et al., 2015; Hwang et al., 2018). Moreover, the phosphorylated, ATP-bound structure of zCFTR shows a head-to-tail NBD dimer with two ATP molecules sandwiched at the dimer interface (Zhang et al., 2017) as predicted from functional studies of human CFTR (Mense et al., 2006).

Another structural insight bearing evolutionary significance also emerges from these elegant cryo-EM studies. These structures virtually confirm that CFTR, although the only ion channel in the ATP-binding cassette (ABC) transporter superfamily, retains not only the overall architecture of a typical ABC exporter in its TMDs, but also the

highly conserved chemistry in the ATP binding pockets shared by all ABC transporters. For ABC exporters, it is generally thought that ATP binding-induced NBD dimerization provides the "power stroke" to convert the resting inward-facing conformation to an outward-facing conformation of TMDs to release the bound cargo to the extracellular solution; subsequently, the free energy of ATP hydrolysis is used to separate the NBD dimer to reset the system so that the now inward-facing TMDs can accept another substrate (Locher, 2009; Seeger and van Veen, 2009; Szollosi et al., 2017). Gating of CFTR is believed to follow a similar scheme: ATP binding-induced NBD dimerization and hydrolysis-triggered separation of the NBD dimer are coupled respectively to the opening and closing of CFTR's gate in TMDs (Liu et al., 2017; cf. Jih et al., 2017). Thus, mutations that abolish ATP hydrolysis (e.g., E1371Q in hCFTR) can keep the gate open for minutes, resulting in a channel with an open probability (P_o) close to unity (Vergani et al., 2003; Bompadre et al., 2005b; cf. Zhang et al., 2017). This strategy of stabilizing NBDs in a dimerized form to acquire the open channel conformation of CFTR was adopted by Zhang et al. (2017) in their latest ground-breaking cryo-EM work on zCFTR. Although the solved atomic structure of zCFTR with the E1372Q mutation indeed shows prototypical NBDs in a dimerized form, the TMDs unexpectedly assume a nonconductive conformation (Zhang et al., 2017). The authors proposed that this nonconductive state represents a "post-open" closed state that is embedded within an opening burst. To explain the fact that this closed state must be quite stable to become the dominant conformations in their preparation, but at the same time "invisible" during hCFTR electrophysiological recording, the authors further speculated that high frequency transitions between the open state and this presumed "intra-burst" closed states were

mostly filtered out due to a limited bandwidth of recording. However, these interpretations of zCFTR structure were based on data collected from electrophysiological studies of hCFTR. It should be noted that a high degree of structural similarities between unphosphorylated apo-forms of hCFTR and zCFTR (55% sequence identity) does not guarantee that these two orthologs must behave similarly after phosphorylation activation and ATP binding. Indeed, despite as high as 76% homology between human and mouse CFTR (Tata et al., 1991; Yorifuji et al., 1991), their gating behaviors and responses to some pharmacological reagents differ drastically (Lansdell et al., 1998; Ostedgaard et al., 2007; Van Goor et al., 2009; Dong et al., 2012; Hadida et al., 2014; Bose et al., 2015; Cui and McCarty, 2015; Cui et al., 2016). Thus, our mechanistic understanding of this important zCFTR structure with dimerized NBDs as well as future exploitations of the cryo-EM CFTR structures at large hinges on an urgent need for functional data with zCFTR.

In the current study, we characterized zCFTR expressed in CHO cells with the patch-clamp technique. We demonstrated that similar to hCFTR, zCFTR is activated by PKA-dependent phosphorylation. Phosphorylated zCFTR is gated by ATP with a similar sensitivity to ATP as hCFTR. At the single-channel level, however, zCFTR assumes a very low P_o (0.03± 0.02; cf. ~0.50 for hCFTR in Yeh et al., 2015) with exceptionally long interburst (~3 s), and brief open burst duration (~120 ms) and frequent irregular sub-conductance states. Introducing the E1372Q mutation indeed stabilized the open burst state to tens of seconds, but contrary to hCFTR under the same condition (Po > 0.94; Yu et al., 2016), the P_o within a burst in E1372Q-zCFTR is ~0.35 with abundant long intra-burst closures. The observation that the closed state of zCFTR, even when the NBDs are

145

in a dimerized form (E1372Q-zCFTR), is more stable than the open state, suffices to account for the dominance of a closed channel conformation in the cryo-EM preparations of two zCFTR structures. Different gating kinetics between zCFTR and hCFTR from our results when compared with published comparable ATPase activities grant two new insights into the molecular mechanism of zCFTR gating: First, the closed state of zCFTR can hydrolyze ATP. Second, since ATP hydrolysis for ABC transporters occurs at the NBD dimer interface, this hydrolysis-competent closed state may resemble the cryo-EM structure of the closed conformation of zCFTR with dimerized NBDs.

4.3 Method and Materials

Mutagenesis and channel expression

Codon optimized zebrafish CFTR was provided by Dr. Jue Chen (Rockefeller University). The native form of zebrafish CFTR was a gift from Dr. Michel Bagnat's lab at Duke University. Site-directed mutagenesis was done by PCR mutagenesis using the Pfu Ultra II (Agilent Technologies). All constructs were confirmed by DNA sequencing (DNA core; University of Missouri-Columbia) and amplified using Invitrogen Plasmid Miniprep Kit. CHO cells were grown at 37 °C in Dulbecco's modified Eagle's medium containing 10% fetal bovine serum. The cDNA constructs of CFTR were co-transfected with peGFP-C3 (Takara Bio Inc.) encoding the green fluorescent protein using PolyFect transfection reagent (QIAGEN) into CHO cells. The transfected cells were transferred into 35 mm tissue culture dishes containing one layer of sterilized glass chips for cells to grow on. The transfected cells were incubated at 27 °C for 2−7 days before experiments were performed.

146

Reagents and electrophysiology

All patch-clamp experiments were carried out in the excised inside-out configuration. Micropipettes made of borosilicate capillary glass were pulled with a two-stage vertical puller (Narishige) and then fire-polished with a homemade microforge to reach a pipet resistance of 2−7 MΩ when the pipettes were filled with a standard pipet solution (140 mM NMDG-Cl, 2 mM $MgCl_2$, 5 mM $CaCl_2$ and 10 mM HEPES, adjusted to pH 7.4 with NMDG). A glass chip with transfected cells grown on was placed into a chamber on the stage of an inverted microscope (Olympus) and continuously perfused with a bath solution (145 mM NaCl, 5 mM KCl, 2 mM $MgCl_2$, 1 mM $CaCl_2$, 5 mM glucose, 5 mM HEPES, and 20 mM sucrose, adjusted to pH 7.4 with NaOH). Immediately after a membrane patch reached a seal resistance of >40 GΩ, it was excised and continuously perfused with a standard perfusate (150 mM NMDG-Cl, 10 mM EGTA, 10 mM HEPES, 8 mM Tris, and 2 mM $MgCl_2$, adjusted to pH 7.4 with NMDG). Experiments were conducted at room temperature (22−24 °C). Current signals at different holding potentials as required were acquired with a patch-clamp amplifier (EPC9, HEKA), filtered at 100 Hz, digitized online at 500 Hz with Pulse software (version 8.53, HEKA) and captured onto a hard disk. Fast solution exchange was achieved with a commercial solution exchange system (SF-77B Perfusion Fast-Step, Warner Instruments).

ATP (SigmaAldrich) containing solutions were made with the perfusion solution to different concentrations as indicated in Figure 4.1 for ATP dose-response measurement. 10 mM GLPG1837 (Galapagos) stock solution was stored -20 °C and then diluted into the indicated concentrations as required in Figure 4.S8A. To keep the reducing

environment for PKA (SigmaAldrich), we routinely added 2.67 mM dithiothreitol (DTT) (SigmaAldrich) to the perfusion solution containing 32 IU/mL PKA and 2 mM ATP. 2′-deoxy-ATP (d-ATP), and pyrophosphate (PP_i) was purchased from Sigma-Aldrich Co. LLC. N^6-Phenylethyl-ATP (P-ATP) was purchased from Biology Life Science Institute (Bremen, Germany). GlyH-101 and $CFTR_{inh-172}$ (Inh-172) were kindly provided by Dr. Robert Bridges (Department of Physiology and Biophysics, Rosalind Franklin University, Chicago, IL) with support from the Cystic Fibrosis Foundation Therapeutics. Forskolin was purchased from Enzo Life Sciences, Inc.

Data analysis

Current traces recorded at negative voltage were presented in all figures as upward deflections for the sake of clear presentation except for those in Figure 4.2A, where positive currents were presented as upward deflections. The single-channel amplitudes were measured by fitting the distributions in all-points histograms with built-in multi-Gaussian function (Igor 6.3). In addition, in the all-points histograms, the model-independent P_o was calculated by dividing the area under open curve by the overall areas under both the open and closed curves with the midpoint of the two curve peaks as the cutoff to define open events. Single-channel dwell-time analysis was conducted using a home-made program (Bompadre et al., 2005a; Bompadre et al., 2005b) with the same cutoff to define open events as used in the all-points histograms. All results are presented as means ± SEM; N is the number of experiments.

4.4 Results

To characterize the functional properties of zCFTR, we expressed zCFTR in CHO cells and recorded the current in inside-out patches. Not surprisingly, zCFTR is a PKA-activated, but ATP-gated chloride channel. Figure 4.1A shows a real-time recording of zCFTR channel currents: Just like its human counterpart (Figure 4.S1), very small currents were elicited by 2 mM ATP alone prior to the addition of PKA (expanded in the dashed box). The application of PKA and ATP cocktail dramatically increased the currents which dissipated in seconds once the PKA and ATP cocktail was washed out, but a reapplication of ATP without PKA promptly restored the currents. This ATP-dependent gating of phosphorylated zCFTR was reaffirmed in Figure 4.1B showing that the currents of phosphorylated zCFTR in the presence of 10 μM ATP are only about 7% of that at 2 mM ATP. Plotting the fraction of currents from phosphorylated zCFTR channels at different [ATP], we obtained [ATP] dose response relationships for both the codon optimized and the native form of zCFTR (Figure 4.1C). Compared to that of hCFTR (Zhou et al., 2006), the sensitivity of zCFTR to changes of [ATP] is nearly the same.
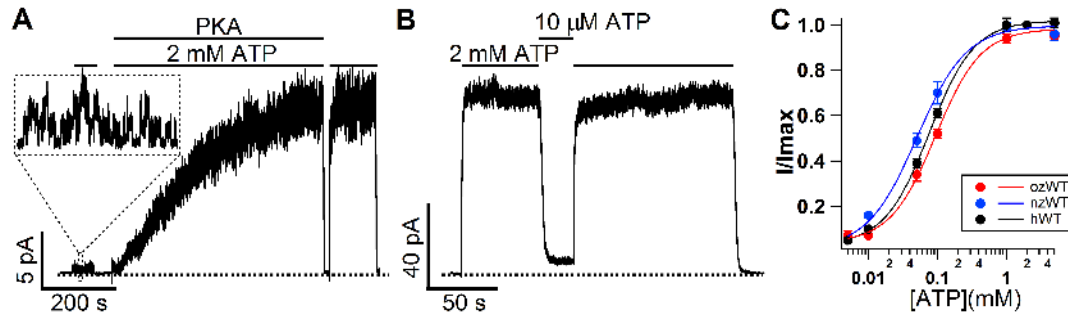
Figure 4.1. zCFTR is PKA phosphorylation activated and ATP-gated channel with similar sensitivity to ATP compared with hCFTR. A. PKA phosphorylation activation and ATP dependence of zCFTR. Right after patch excision, the application of 2 mM ATP only shows tiny amount of channel activity (expanded in dashed square) and is eliminated completely upon ATP washout. The application of PKA in addition to 2 mM ATP robustly increases the current. After washing out PKA and ATP cocktail once the current reaches the steady state (fully phosphorylated), reapplication of 2 mM ATP alone is able to open the channels with high activity to the same level as PKA and ATP combined. **B.** A representative current trace showing the [ATP]-dependence of zCFTR. The channel activities in the presence of 10 μM ATP are only about 7% of that at 2 mM ATP. **C.** Normalized ATP dose-response relationships for codon optimized zCFTR, native form zCFTR and hCFTR. Solid lines (red: codon optimized zCFTR, blue: native form zCFTR, black: hCFTR) represent fits of the data with the Hill equation. The $K_{1/2}$ for codon optimized zCFTR and native form zCFTR are 0.09 mM (Hill co-efficient = 1.3) and 0.05 mM (Hill co-efficient = 1.2) respectively. The K1/2 for hCFTR data is 0.076 mM (Hill co-efficient = 1.3 with data from Zhou et al., 2006).
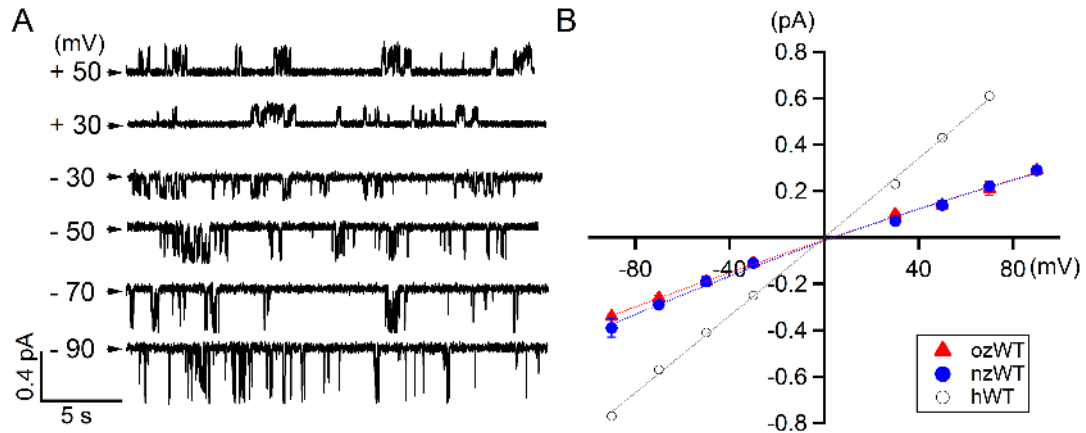
Figure 4.2. Single-channel recording of zCFTR shows smaller channel conductance levels with clear inward-rectification. A. Single channel recordings of zCFTR recorded at different membrane potentials from + 50 mV to - 90 mV. In addition to smaller channel conductance, multiple sub-conductance levels were often observed. **B.** Single-channel I-V relationship of zCFTR shows smaller conductance and inward-rectification. The single-channel I-V relationship of hCFTR (Yu et al., 2016) is shown in circles as a reference. The I-V relationships of both codon optimized (ozWT, red triangle) zCFTR and native form zCFTR (nzWT, blue dot) are nearly identical.

Given the macroscopic data presented in Figure 4.1, it seems that zCFTR is functionally similar to hCFTR. However, the single-channel recordings of zCFTR reveal immensely different functional properties. First, unlike hCFTR with clear, readily discernible opening and closing events that last for tens to hundreds of milliseconds (e.g., Figure 4.3A below), the single-channel recording of zCFTR shows very different patterns (more details in Figure 4.3 below and in Figure 4.S2). In addition, compared to hCFTR, the single-channel conductance of zCFTR is smaller. Figure 4.2A presents single-channel traces of zCFTR at different holding potentials. Moreover, the single-channel I-V curves of zCFTR (both codon-optimized and native form) in Figure 4.2B show a clear inward-rectification. Interestingly, sequence comparison between zCFTR and hCFTR shows that most of the reported pore-lining charged residues in hCFTR, such as K95, E92, K190, R248 (K in zCFTR), R251 (K in zCFTR), R303, R352, D363, K370, D993, K1041 and R1048 are conserved in zCFTR (Aubin and Linsdell, 2006; Wang et al., 2011; Norimatsu et al., 2012; Gao et al., 2013; El Hiani and Linsdell, 2015; Zhang and Hwang, 2015; El Hiani et al., 2016; Zhang and Hwang, 2017). Thus, the observed smaller single-channel amplitudes and the inward-rectification suggest that the TMDs especially the pore architecture of zCFTR should also bear some structural differences from that of hCFTR despite the high structural similarities between two unphosphorylated closed conformations of these orthologues (Zhang and Chen, 2016; Liu et al., 2017).
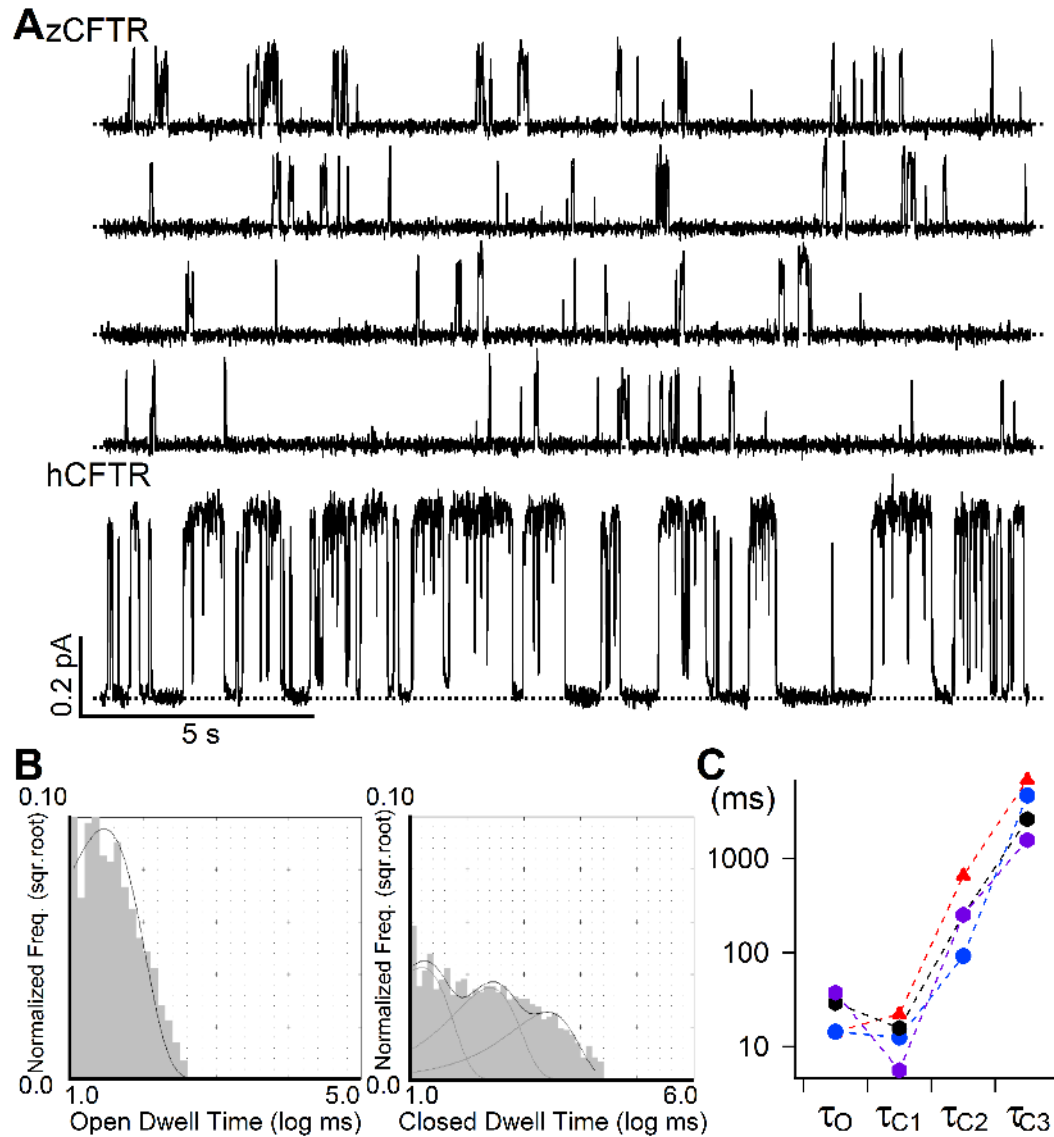
Figure 4.3. Single-channel behavior and dwell-time analysis of zCFTR. A. Continuous single-channel recording of zCFTR showing brief openings and long closures, in stark contrast to well defined opening bursts and interburst closures seen in hCFTR. **B.** Dwell-time analysis of zCFTR resolved one component for the opening events and three populations for closures. **C.** Time constants extracted from panel B reveals two stable closed states with time constants of 314 ms (τ_{C2}) and 3933 (τ_{C3}) ms in addition to a short-lived closure (τ_{C1} = 14 ms).

As described above, the gating properties of zCFTR are very different from that of hCFTR. Figure 4.3A shows an 80-s real-time continuous single-channel recording of phosphorylated zCFTR in the presence of 2 mM ATP (A short segment of single-channel recording of hCFTR is displayed for comparison). Unlike hCFTR, the opening events are mostly very brief; some of the openings are so brief that the full opening is not resolved because of filtering. While the bursting behavior of hCFTR has been well described (hundreds of milliseconds bursts with short-lived intra-burst closure of ~5 ms in duration in Yu et al., 2016), it is difficult to define a burst for zCFTR. In addition, many closed events that last longer than 1 s were easily seen. Thus, the P_o of zCFTR must be much lower than that of hCFTR. In light of this unusual gating behavior of zCFTR, we first generated all-points histograms, which yields a model-independent P_o of 0.03 ± 0.02 (n = 4), 15-fold lower than that of hCFTR. Subsequently, we used single-channel opening and closing events to construct dwell-time histograms (Figure 4.3B): While the open time histogram can be well fitted with a single exponential function ($\tau_O = 24 \pm 6$ ms, N = 4), three populations of the closed events are observed ($\tau_{C1} = 14 \pm 4$ ms, $\tau_{C2} = 314 \pm 122$ ms, $\tau_{C3} = 3933 \pm 1167$ ms, N = 4). In a latest report (Yu et al., 2016), we employed similar analysis for hCFTR and obtained $\tau_O = 200$ ms and $\tau_{C1} = 5$ ms and $\tau_{C2} = 502$ ms. Figure 4.3C summarizes the results from this dwell time analysis in four different patches. Although we observed significant variations, it is safe to conclude that zCFTR strongly prefers the closed state even in the presence of saturating [ATP]. Collectively, the data in Figure 4.2 and 4.3 suggest that although zCFTR and hCFTR show similar [ATP] sensitivity, their gating behaviors are dramatically different.

To eliminate the brief closures that are traditionally considered as events not related to ATP-dependent gating (Winter et al., 1994; Vergani et al., 2003), we carried out burst analysis by setting a delimiter (79 ms) between the first two peaks of the closed time histogram, and obtained an open burst duration of 120 ms with the two closed time constants of 257 ms and 2649 ms respectively. Thus a whole burst should be at least 2769 ms. Of note, similar analysis of WT-hCFTR yielded a whole burst around 866 ms (τ_{burst} = 386 ms and $\tau_{interburst}$ = 480 ms reported in Yu et al., 2016). Thus, quite different from hCFTR, even under a saturating concentration of ATP, in addition to a much shortened opening burst, WT-zCFTR can stay closed for seconds without sojourning to an open state.
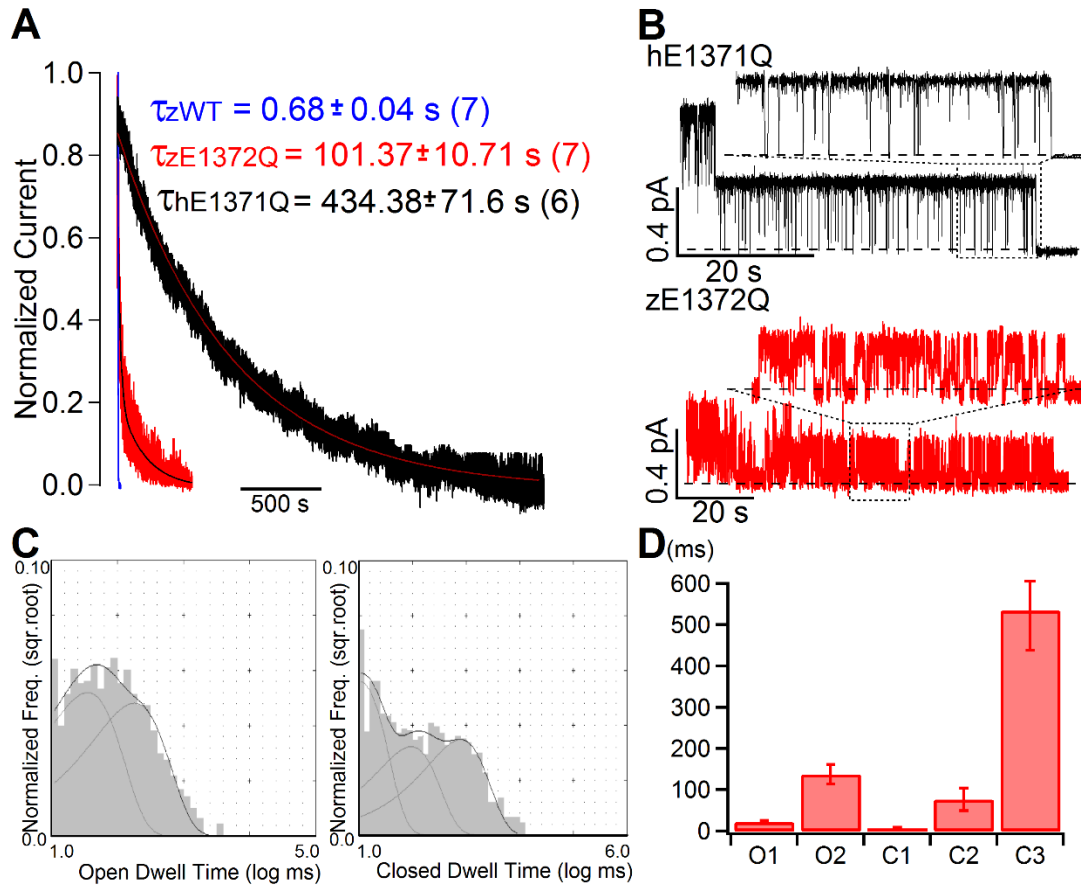
Figure 4.4. Effects of ATP hydrolysis on zCFTR gating. A. Normalized current relaxations upon ATP

removal for WT-zCFTR (blue), E1372Q-zCFTR (red) and E1371Q-hCFTR (black). The relaxation time

constant for each construct is presented. A drastic increase of the relaxation time constant in E1372Q-

zCFTR suggests that ATP hydrolysis plays a role in zCFTR gating. Of note, the time constant for E1372Q-

zCFTR is much smaller than that for E1371Q-hCFTR. **B.** Representative microscopic current traces of

E1371Q-hCFTR and E1372Q-zCFTR contrasting the gating behavior within a prolonged opening burst.

The upper trace shows an expanded view of the last locked-open channel of E1371Q-hCFTR, in which the

channel stays in the open states for tens of seconds with only transient intra-burst closures. However,

although the E1372Q-zCFTR channel (lower trace) also stays in the open-burst states for tens of seconds,

the burst is intersected by not only short-lived closures but also stably closed events. A model-independent

P_o within the locked-open burst of E1372Q-zCFTR generated with all-points histograms yields a P_o of 0.35

± 0.05, (N = 9). **C.** Representative dwell-time histograms for E1372Q-zCFTR suggest two open time

constants and three closed time constants. **D** Kinetic parameters extracted from dwell-time analysis on 5 patches: τ_{O1}: 22 ± 4 ms and τ_{O2}: 137 ± 23 ms; τ_{C1}: 6 ± 3 ms, τ_{C2}: 77 ± 28 ms, τ_{C3}: 535 ± 97 ms (N = 5).

Despite the drastic differences in gating kinetics between hCFTR and zCFTR, ATP hydrolysis does play a similar role in controlling CFTR gating for these two orthologs. Figure 4.4A shows a dramatic prolongation of the current relaxation upon removal of ATP by introducing the hydrolysis-deficit mutation (E1372Q) into zCFTR. However, we also noted a quantitative difference in the current relaxation time constants between human and zebrafish constructs (101 s in E1372Q-zCFTR vs. 434 s in E1371Q-hCFTR). More striking difference resides in the detailed gating kinetics in a locked-open burst of E1372Q-zCFTR (Figure 4.4B). While a P_o close to unity within the locked-open burst of E1371Q-hCFTR, E1372Q-zCFTR shows more frequent and long closures within one locked-open burst. Quantitatively, a model-independent P_o within the locked-open burst generated with all-points histograms yields a P_o of 0.35 ± 0.05, (N = 9), suggesting that E1372Q-zCFTR prefers the closed state even with dimerized NBDs. Figure 4.4C shows representative dwell-time histograms with the open time histogram best fitted with two components and the closed time histogram with three components (Figure 4.4D). It is worth noting that this low P_o is not due to previously proposed voltage-dependent blockade of the pore by small molecules in the cytoplasmic solution (Zhou et al., 2001; Zhang and Hwang, 2017), since similar frequent intra-burst closures are also observed in recordings at a positive voltage (Figure 4.S3). Collectively, the preference for closed states in E1372Q-zCFTR over open states explains why a non-conductive state with dimerized NBDs is captured as the dominant conformation in the cryo-EM study (Zhang et al., 2017). The drastic differences in gating behavior between hCFTR and zCFTR— hydrolysis intact or not—also suggest the necessity to revisit the interpretation of the structures of zCFTR with only functional data of hCFTR.

4.5 Discussion

In the current study, we characterized the electrophysiological properties of zCFTR, and found many biophysical and pharmacological features of zCFTR distinct from its human brethren, although zCFTR channels, like its human ortholog, are activated by PKA-dependent phosphorylation and gated by ATP. Notwithstanding the remarkable similarities between hCFTR and zCFTR in their apo structures (Zhang and Chen, 2016; Liu et al., 2017), the single-channel conductance of zCFTR is smaller than that of hCFTR with a clear inward rectification (Figure 4.2B), suggesting the open states of these two constructs bear significant differences in their respective anion permeation pathway. More strikingly, despite a nearly identical sensitivity to ATP, gating of phosphorylated zCFTR at a saturating [ATP] is greatly subdued with an open probability more than 15-fold lower than that of hCFTR ($P_o = 0.03$ for zCFTR in Figure 4.3 versus $P_o = 0.50$ for hCFTR in Yeh et al., 2015). Detailed kinetic analysis revealed that this low P_o is mostly due to extremely long closed events in the range of seconds (τ_{C3} in Figure 4.3) intersecting the bursts of openings that are disrupted by visible intra-burst closures as long as 300 ms lifetime (τ_{C1} and τ_{C2} in Figure 4.3). Without referring to any gating model, we can conclude that zCFTR strongly prefers the closed channel conformation rather than the open state even in the presence of 2 mM ATP that is sufficient to saturate the ATP binding at NBDs (Figure 4.1C). However, zCFTR seems to retain the capacity of using ATP hydrolysis to terminate its opening bursts as mutating the catalytic glutamate (E1372) drastically prolongs the current relaxation upon removal of ATP (current relaxation time constant τ in Figure 4.4 from 0.68 s to 101 s). Most interestingly, unlike human E1371Q-CFTR whose P_o is close to unity (Vergani et al., 2003; Bompadre et al.,

2005b), E1372Q-zCFTR shows a much lower P_o of 0.35 (Figure 4.4). Hence, even when ATP hydrolysis is eliminated, the closed state of zCFTR is still more stable than the open state. This latter observation nicely explains why the cryo-EM structure of E1372Q-zCFTR assumes a closed channel conformation despite with a characteristic NBD dimer (Zhang et al., 2017). Moreover, although with a high degree of conservation in the NBDs, compared to hCFTR, zCFTR responds to ATP and phosphate analogues poorly (see details in Supporting Materials), suggesting some functional differences in NBDs and/or in the coupling between NBDs and the gate in TMDs. In the following text, we will first focus our discussion on the potential mechanistic insights derived from these data. By elucidating the salient functional differences between structurally similar human and zebrafish CFTR, we underscore the importance of integrating both structural and functional approaches to attain a comprehensive understanding of the molecular physiology of CFTR.

In stark contrast with hCFTR, our single-channel recordings of both WT-zCFTR and E1372Q-zCFTR are predominated by long closed events (Figure 4.3 and 4.4). Thus, not surprisingly, the cryo-EM structure of E1372Q-zCFTR solved recently turns out to be a non-conductive conformation (Zhang et al. 2017). As the closed state with dimerized NBDs is considered a transition state (Vergani et al., 2005; Csanady et al., 2010), Zhang et al. (2017) proposed that this non-conductive conformation of E1372Q-zCFTR represents a "post-open" closed state (named C_2 thereafter) based on hCFTR functional data and derived from a gating model developed for hCFTR (Csanady et al., 2010; Liu et al., 2017). Kinetically, the E1372Q-zCFTR channel visits C_2 after it is first opened by ATP:

$$C_1 <\!\!------\!\!> O \leftrightarrow C_2 \qquad \text{(Scheme 4.1, cf. Liu et al., 2017)}$$

In this scheme, C_1 represents the initial, ATP-free closed state; the ATP-bound closed state before NBD dimerization is enclosed in the dashed line; O and C_2 represent respectively the open and closed states with dimerized NBDs. It was also proposed that the transitions $O \leftrightarrow C_2$ reflect quick ATP-independent motions of parts of the TMDs (mobile external segments of TM8 and TM12) between an open and a closed conformation while the NBDs remain dimerized. Since such a "post-open" C_2 state, stable enough to be captured as dominant in cryo-EM zE1372Q structure (Zhang et al. 2017) was not observed in human functional data, this "post-open" idea was further extrapolated to the human equivalent E1371Q-hCFTR by speculating that frequent and abundant $O \leftrightarrow C_2$ transitions in human E1371Q-CFTR were filtered out because of the low bandwidth of recording, resulting in an apparent observed P_o close to unity. **Here**, by demonstrating very different gating behaviors between E1372Q-zCFTR and E1371Q-hCFTR at a single-channel level, we found that the extrapolation of the "post-open" idea to E1371Q-hCFTR based on the cryo-EM results of E1372Q-zCFTR is unnecessary. Moreover, if the P_o for hE1371Q were indeed far from unity with a tremendous amount of closures filtered out as posited (Zhang et al., 2017) and there were little functional difference between these two constructs, CFTR potentiator such as GLPG1837 (Yeh et al., 2017) should increase the macroscopic current of E1371Q-hCFTR by stabilizing the O state as it did on E1372Q-zCFTR (Figure 4.S4, E1372Q-zCFTR potentiated by GLPG1837). However, although GLPG1837 increased the steady state mean currents of E1372Q-zCFTR and WT-hCFTR, it failed to increase the macroscopic current of E1371Q-hCFTR as though the P_o of E1371Q-hCFTR is already close to unity (Figure 4

in Yeh et al., 2017 using E1371S-hCFTR). Thus, a simple explanation for the differences between E1372Q-zCFTR and E1371Q-hCFTR is that the C_2 state is more stable (relative to the open state) in the zebrafish construct.

A puzzle emerged when we look into two sets of experimental data. One set of data suggested that the directly measured ATPase activity for zebrafish CFTR (0.66 s^{-1} ATP turnover rate) is similar to, at least not smaller than, that of human CFTR (0.37 s^{-1} ATP turnover rate) measured within the same research group (Zhang and Chen, 2016; Liu et al., 2017). However, the other set of data using the same mathematical approach adopted by Liu et al. (2017) to indirectly estimate ATP turnover rate (0.52 s^{-1}) with the average time for completion of the gating cycle in a single-channel recording, which is based on one-to-one stoichiometry between gating cycles and numbers of ATP hydrolyzed suggested that the ATP turnover rates for zebrafish CFTR and human CFTR derived from our own single-channel recordings are distinctly different. Expressed with CHO cells, the average time of completion of the gating cycle for zCFTR is at least 2769 ms according to Figure 4.3 (0.36 s^{-1} ATP turnover rate) and for hCFTR is at least 866 ms (1.15 s^{-1} ATP turnover rate) (Yu et al., 2016). Thus the apparent ATP turnover rate in zCFTR from our single-channel recordings appears to be three folds smaller than that in hCFTR, conflict with a conclusion based on ATPase activity assays.

Thus, it is reasonable to reexam the assumption of one-to-one stoichiometry between gating cycles and numbers of ATP hydrolyzed in the biophysical approach adopted by Liu et al. (2017). If ATPase activity assays are reliable and the ATP turnover rate in zCFTR is indeed as proposed to be similar to that in hCFTR (Zhang and Chen, 2016; Liu et al., 2017), the obvious differences in gating kinetics between zCFTR and

162

hCFTR from our functional data especially the extremely long "gating cycle" of zCFTR lead us to suggest that at least for zCFTR, more than one ATP hydrolysis event should happen within the 2769 ms long "gating cycle", likely during the long interburst closed state (>2s), so as to yield an ATP turnover rate higher than 0.36 s^{-1} and similar to that of hCFTR (1.15 s^{-1}). This suggestion that the closed state of zCFTR can hydrolyze ATP, although awaits more direct experimental evidence, seems reasonable since the cryo-EM structure of E1372Q-zCFTR indeed shows a tight NBD dimer with all the conserved interactions with ATP at the dimer interface but the TMDs in a closed state. It is also not surprising that ATP hydrolysis events in the closed state if they exist, are not obviously resolvable in WT-hCFTR because of the brief interburst closed duration ($\tau_{interburst}$ = 480 ms, reported in Yu et al., 2016). More experiments are needed and mutations at the TMDs with much longer (such as K978C and V847T) or briefer "gating cycle" (such as L102C and R117H) are helpful to test this idea.

Before we end our discussion of the gating properties of zCFTR, we note that all these gating characteristics observed in zCFTR including low P_o, brief opening bursts and prolonged inter-burst durations for WT-zCFTR channels, as well as shortened relaxation time constant for E1372Q-zCFTR, are reminiscent of a hCFTR variant R117H we reported previously, which should work as a good candidate to test the idea of ATP hydrolysis in the closed state considering its long $\tau_{interburst}$ (τ_o = 23 ms, τ_{C1} = 39 ms τ_{c2} = 1897 ms in Yu et al., 2016).

Although R117H-hCFTR causes mild-form CF with abnormal gating and chloride conductance due to a mutation at the first extracellular loop of the TMDs, its responses to ATP and phosphate analogues are qualitatively similar to WT-hCFTR (Yu et al., 2016).

In contrast, although zCFTR shares many gating characteristics with R117H-hCFTR, it responds differently to these reagents that assess the function of NBDs (Figure 4.S5). For instance, different from the ability of PP_i to lock open WT-hCFTR (Tsai et al., 2009; Jih et al., 2012), the effect of PP_i on WT-zCFTR is negligible (Figure 4.S5A). More strikingly, 2'-deoxy-ATP and P-ATP, both more effective ligands than ATP for hCFTR (Aleksandrov et al., 2002; Tsai et al., 2010), did not gate WT-zCFTR well (Figure 4.S5B and 4.S5C) under the same condition. Thus, although the NBDs are highly conserved in sequence (66 % homology between hCFTR and zCFTR), some minor structural variations in the NBDs may exist and bear significant functional consequences. Although the binding sites for CFTR potentiators such as GLPG1837 or inhibitors such as $CFTR_{inh-172}$, GlyH-101 are yet to be identified, our data also suggest subtle differences in affinity between hCFTR (Kopeikin et al., 2010 and Figure 4.S6; Yeh et al., 2017) and zCFTR (Figure 4.S7 and 4.S8). The mechanism behind these surprising differences awaits more investigations on zCFTR in the future, but all the functional differences observed in the current study cannot be accounted for by the codon optimization employed for both cryo-EM and current studies since nearly identical results were obtained for native form zCFTR expressed in CHO cells (For details, see the Supporting Materials).

Collectively, our thorough characterization of zCFTR with the patch-clamp techniques unveiled a wide spectrum of functional differences between zCFTR and hCFTR despite their presumed high structural similarities. On one hand, these functional data remind us of the unrivaled temporal resolution of electrophysiological methodologies that allows monitoring the real-time dynamic properties of a single CFTR molecule in the cell membrane. On the other hand, high-resolution CFTR structures

bestowed with their unparalleled spatial resolution, when put in the context of the functional data, could definitively shed light on the molecular mechanism of this medically important protein and potentially provide novel insights for the development of new therapeutic interventions for CF clinics.
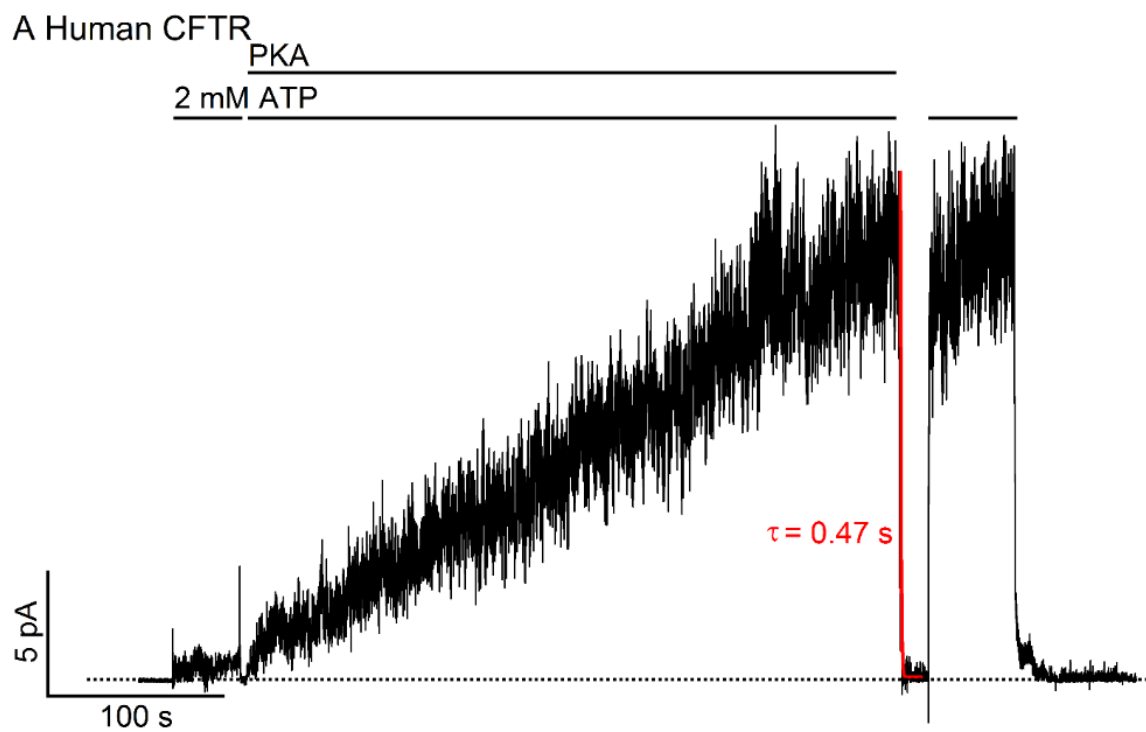
4.6 Supporting Materials

Figure 4.S1. WT-hCFTR is PKA phosphorylation activated and ATP-gated.
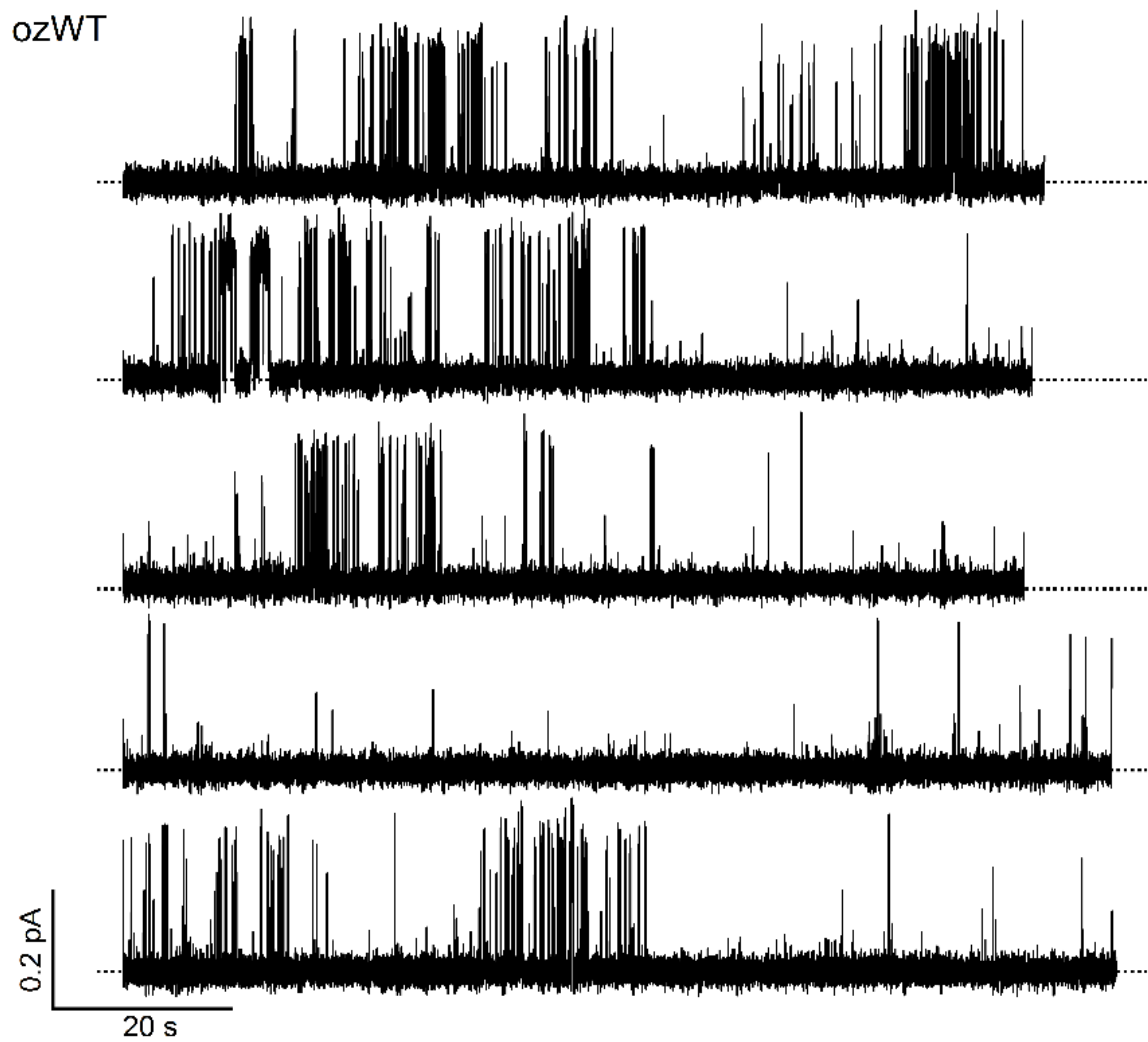
Figure 4.S2. More single-channel recordings of WT-zCFTR. These recordings from multiple patches

show clearly the stochastic behavior of WT-zCFTR with long interburst duration and brief openings.

Figure 4.S3. E1372Q-zCFTR at +50 mV. The representative recording of E1372Q-zCFTR recorded at

+50 mV suggests that the observed frequent intra-burst closures (Figure 4.4B) within a lock-open burst are

not due to intrinsic anionic molecule blocking, which is voltage dependent.
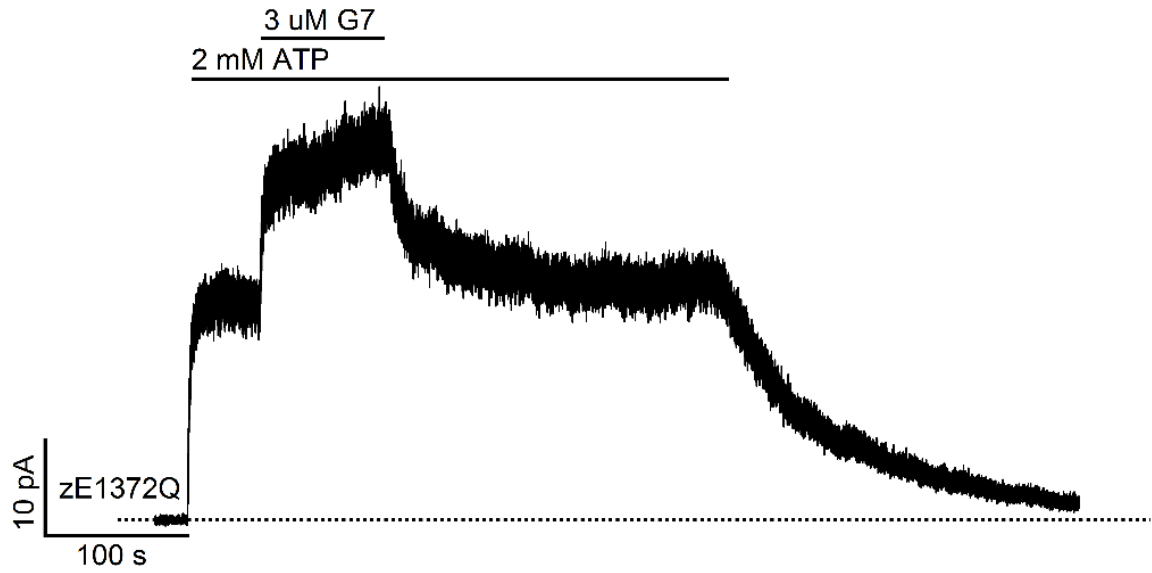
Figure 4.S4. GLPG1837 potentiates E1372Q-zCFTR. Of note, this potentiation of GLPG1837 is consistent with the estimation of a P_o to be below 0.5. $P_o = 0.35$ could be an overestimation since this frequent open and close might be contributed by multiple locked-open channels with low open probability. The data of E1372Q-zCFTR suggests that although the NBDs are highly conserved in CFTR across all species, the lock-open E1372Q-zCFTR still behaves differently, i.e. prefers the closed state with low P_o.

169
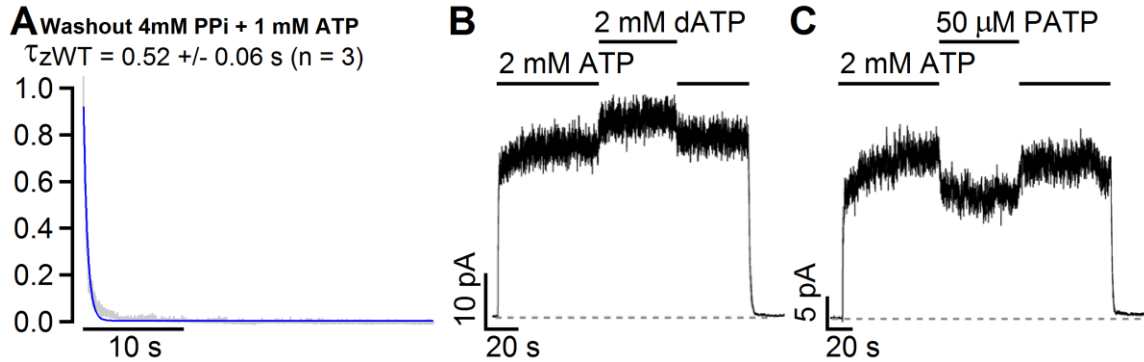
Figure 4.S5. zCFTR shows different responses to ATP and phosphate analogues. **A.** Normalized current decay upon washing out 1mM ATP and 4 Mm MgPPi shows even smaller time constant as compared with washing out 2 mM ATP (0.68 s in Figure 4.4A). **B.** 2 mM dATP shows similar potency as 2 mM ATP for zCFTR whereas 2 mM dATP strongly increase the mean current of WT-hCFTR than 2 mM ATP (Aleksandrov et al., 2002). **C.** 50 μM P-ATP decreases the mean current of zCFTR (I_{PATP}/I_{ATP}=0.51±0.02, N=4). On the contrary, 50 μM P-ATP results in almost a 2-fold current increase in hCFTR as compared with 2.75 mM ATP (Jih et al., 2011).

To further investigate the NBD machinery of zCFTR, we tested the effect of pyrophosphate (PP$_i$) and ATP analogues d-ATP and P-ATP. PP$_i$ is reported to effectively lock-open hCFTR once applied with lower concentration of ATP, thus as a result, the time constant of the current decay upon washing out the cocktail (1 mM Mg^{2+}ATP and 4 mM Mg^{2+}PPi) is dramatically prolonged to 30 s (Jih et al., 2011). In our study, the application of PP$_i$ is not able to lock open the channels since the time constant from single-exponential fitting of the current decay phase upon washing out the cocktail (1 mM Mg^{2+}ATP and 4 mM Mg^{2+}PP$_i$) is almost identical to that upon washing out ATP alone (0.68s in Figure 4.4A for washing out 2 mM Mg^{2+}PP$_i$). As reported previously, ATP analogues 2 mM d-ATP and 50 μM P-ATP increase the Po or the mean current dramatically as compared with 2 mM ATP (Aleksandrov et al., 2002; Jih et al., 2011), however, the same concentration of d-ATP (2 mM) shows an overall same channel

activity as hCFTR and P-ATP (50 μM) surprisingly shows a decreased channel activity

($I_{P\text{-}ATP}/I_{ATP}$=0.51±0.02, N=4). Collectively, the zCFTR not only shows different gating

behaviors in the presence of ATP (Figure 4.2 and 4.3) but also shows different responses

to ATP and phosphate analogues despite the highly conserved NBDs between zCFTR

and hCFTR.
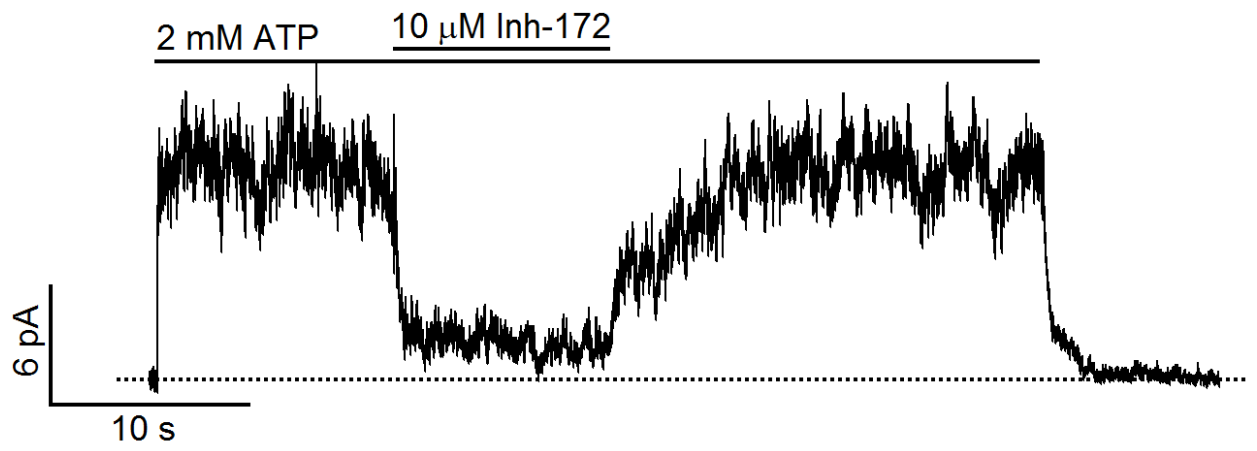
Figure 4.S6. 10 μM Inh-172 inhibit 90% of hCFTR current.
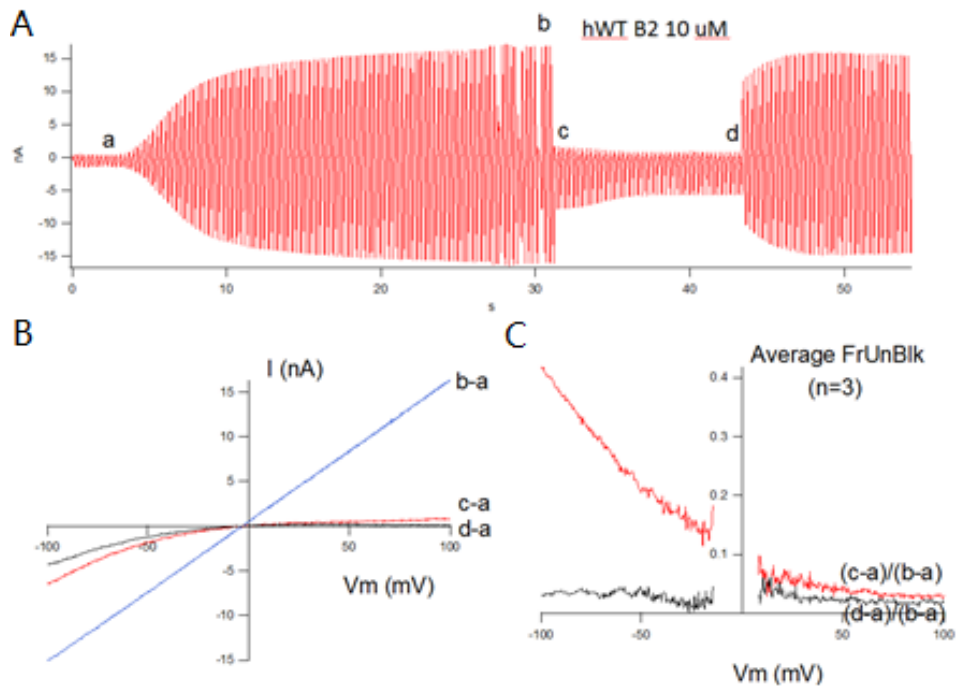
Figure 4.S7. WT-hCFTR blocked by external GlyH101. A. External 10 μM GlyH-101 block WT-hCFTR shows a fast one phase. **B.** Net current shows stronger block of GlyH-101 at positive voltage. **C.** The fraction of unblock for the fast block process represents (c-a)/(b-a) in panel C and the final block stage represents (d-a)/(b-a). The $F_{unblock}$ - V relationship suggests that the fast block process by external GlyH-101 shows clear voltage-dependence that almost eliminates the current and final blocked stage is voltage-independent. Of note, 10 μM GlyH-101 (B2) applied to WT-hCFTR shows only one phase of current decay.
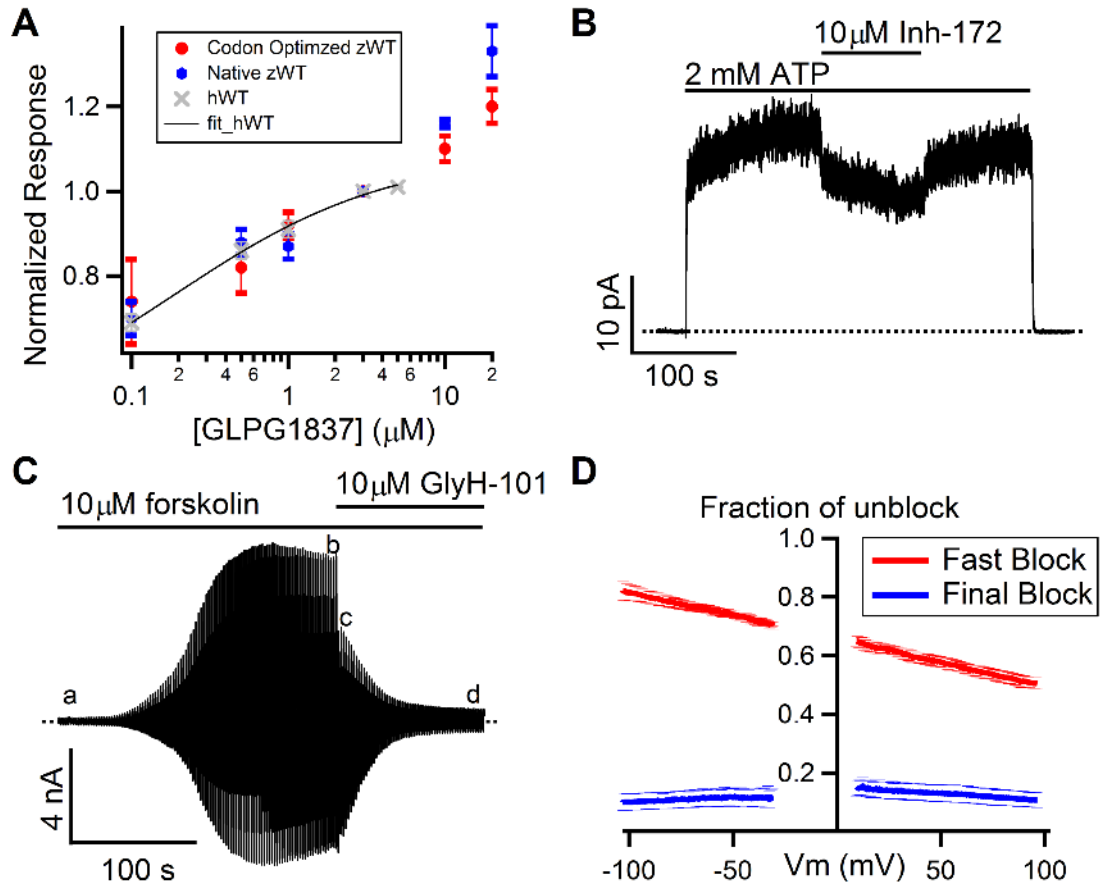
Figure 4.S8. Pharmacological exploration on zCFTR also reveals different characteristics. A. zCFTR

is further potentiated by higher concentration of GLPG1837 than 3 μM GLPG1837. However, 3 μM

GLPG1837 is enough to show full efficacy in hCFTR (Yeh et al., 2017). **B.** CFTR inhibitor-172 shows less

inhibition effect on zCFTR whereas 10 inhibitor-172 eliminate about 90% of hCFTR current in Figure 4.S6

(Kopeikin et al., 2010). **C.** External application of GlyH-101 shows a two-step block upon zCFTR. **D.**

Averaged fraction of unblock for both fast blocking process and final block stage extracted from recording

in panel C. The fraction of unblock for the fast block process represent (c-a)/(b-a) in panel C and the final

block stage represents (d-a)/(b-a). The F_{ub} - V relationship suggests that the fast block process by external

GlyH-101 shows clear voltage-dependence and final blocked stage is voltage-independent.

The data that zE1372Q prefers the closed state with dimerized NBDs suggest of a certain degree of autonomy in the TMDs. This autonomy of the TMDs may be potentiated to stabilize the open state by CFTR potentiator GLPG1837 since GLPG1837 is reported to work at the TMDs to increase the Po independent of the NBDs (Yeh et al., 2017). Thus we tested the efficacy of GLPG1837 on zCFTR and found that, unlike hCFTR to be fully potentiated by 3 µM GLPG1837, higher concentrations such as 10 µM and 20 µM further increase the macroscopic current of zCFTR (Figure **4.S8**A). In addition, the different electro-positivity in the pore of zCFTR revealed by the single-channel behaviors (smaller conductance and inward-rectification) may also suggest a different response of zCFTR to CFTR inhibitors, such as Inh-172. Indeed, our data (Figure **4.S8**B) show that, 10 µM Inh-172 only inhibits 30% of the current on zCFTR (Figure **4.S8**B) while the same concentration of Inh-172 inhibits the macroscopic current of hCFTR by about 90% (Figure **4.S6)** (Kopeikin et al., 2010). Furthermore, the whole-cell recording of zCFTR blocked by external GlyH-101 demonstrates a biphasic current decay upon the application of 10 µM GlyH-101(**4.S8**C and **4.S8**D), which suggests at least two processes/steps/binding sites for GlyH-101 blockage in contrast with the data that 10 µM GlyH-101 applied to hCFTR shows only one phase of fast current decay (Figure **4.S7A**).

4.7 References

Aleksandrov, A.A., L. Aleksandrov, and J.R. Riordan. 2002. Nucleoside triphosphate pentose ring impact on CFTR gating and hydrolysis. *FEBS letters*. 518:183-188.

Aubin, C.N., and P. Linsdell. 2006. Positive charges at the intracellular mouth of the pore regulate anion conduction in the CFTR chloride channel. *The Journal of general physiology*. 128:535-545.

Bompadre, S.G., T. Ai, J.H. Cho, X. Wang, Y. Sohma, M. Li, and T.C. Hwang. 2005a. CFTR gating I: Characterization of the ATP-dependent gating of a phosphorylation-independent CFTR channel (DeltaR-CFTR). *The Journal of general physiology*. 125:361-375.

Bompadre, S.G., J.H. Cho, X. Wang, X. Zou, Y. Sohma, M. Li, and T.C. Hwang. 2005b. CFTR gating II: Effects of nucleotide binding on the stability of open states. *The Journal of general physiology*. 125:377-394.

Bose, S.J., T.S. Scott-Ward, Z. Cai, and D.N. Sheppard. 2015. Exploiting species differences to understand the CFTR Cl- channel. *Biochemical Society transactions*. 43:975-982.

Csanady, L., P. Vergani, and D.C. Gadsby. 2010. Strict coupling between CFTR's catalytic cycle and gating of its Cl- ion pore revealed by distributions of open channel burst durations. *Proceedings of the National Academy of Sciences of the United States of America*. 107:1241-1246.

Cui, G., N. Khazanov, B.B. Stauffer, D.T. Infield, B.R. Imhoff, H. Senderowitz, and N.A. McCarty. 2016. Potentiators exert distinct effects on human, murine, and Xenopus CFTR. *American journal of physiology. Lung cellular and molecular physiology*. 311:L192-207.

Cui, G., and N.A. McCarty. 2015. Murine and human CFTR exhibit different sensitivities to CFTR potentiators. *American journal of physiology. Lung cellular and molecular physiology*.ajplung 00181 02015.

Dong, Q., L.S. Ostedgaard, C. Rogers, D.W. Vermeer, Y. Zhang, and M.J. Welsh. 2012. Human-mouse cystic fibrosis transmembrane conductance regulator (CFTR) chimeras identify regions that partially rescue CFTR-DeltaF508 processing and alter its gating defect. *Proceedings of the National Academy of Sciences of the United States of America*. 109:917-922.

El Hiani, Y., and P. Linsdell. 2015. Functional Architecture of the Cytoplasmic Entrance to the Cystic Fibrosis Transmembrane Conductance Regulator Chloride Channel Pore. *The Journal of biological chemistry*. 290:15855-15865.

El Hiani, Y., A. Negoda, and P. Linsdell. 2016. Cytoplasmic pathway followed by chloride ions to enter the CFTR channel pore. *Cellular and molecular life sciences : CMLS*. 73:1917-1925.

Gadsby, D.C. 2009. Ion channels versus ion pumps: the principal difference, in principle. *Nature reviews. Molecular cell biology*. 10:344-352.

Gao, X., Y. Bai, and T.C. Hwang. 2013. Cysteine scanning of CFTR's first
transmembrane segment reveals its plausible roles in gating and permeation.
Biophys J. 104:786-797.

Hadida, S., F. Van Goor, J. Zhou, V. Arumugam, J. McCartney, A. Hazlewood, C.
Decker, P. Negulescu, and P.D. Grootenhuis. 2014. Discovery of N-(2,4-Di-tert-
butyl-5-hydroxyphenyl)-4-oxo-1,4-dihydroquinoline-3-carboxamide (VX-770,
Ivacaftor), a Potent and Orally Bioavailable CFTR Potentiator. *Journal of
medicinal chemistry*. 57:9776-9795.

Hwang, T.C., and D.N. Sheppard. 2009. Gating of the CFTR Cl- channel by ATP-driven
nucleotide-binding domain dimerisation. *The Journal of physiology*. 587:2151-
2161.

Hwang, T.C., J.T. Yeh, J. Zhang, Y.C. Yu, H.I. Yeh, and S. Destefano. 2018. Structural
mechanisms of CFTR function and dysfunction. *The Journal of general
physiology*.

Jih, K.Y., M. Li, T.C. Hwang, and S.G. Bompadre. 2011. The most common cystic
fibrosis-associated mutation destabilizes the dimeric state of the nucleotide-
binding domains of CFTR. *The Journal of physiology*. 589:2719-2731.

Jih, K.Y., Y. Sohma, M. Li, and T.C. Hwang. 2012. Identification of a novel post-
hydrolytic state in CFTR gating. *The Journal of general physiology*. 139:359-370.

Kopeikin, Z., Y. Sohma, M. Li, and T.C. Hwang. 2010. On the mechanism of CFTR
inhibition by a thiazolidinone derivative. *The Journal of general physiology*.
136:659-671.

Lansdell, K.A., S.J. Delaney, D.P. Lunn, S.A. Thomson, D.N. Sheppard, and B.J.
Wainwright. 1998. Comparison of the gating behaviour of human and murine
cystic fibrosis transmembrane conductance regulator Cl- channels expressed in
mammalian cells. *The Journal of physiology*. 508 (Pt 2):379-392.

Liu, F., Z. Zhang, L. Csanady, D.C. Gadsby, and J. Chen. 2017. Molecular Structure of
the Human CFTR Ion Channel. *Cell*. 169:85-95 e88.

Locher, K.P. 2009. Review. Structure and mechanism of ATP-binding cassette
transporters. *Philosophical transactions of the Royal Society of London. Series B,
Biological sciences*. 364:239-245.

Martin, S.L., V. Saint-Criq, T.C. Hwang, and L. Csanady. 2018. Ion channels as targets
to treat cystic fibrosis lung disease. *Journal of cystic fibrosis : official journal of
the European Cystic Fibrosis Society*. 17:S22-S27.

McCarty, N.A. 2000. Permeation through the CFTR chloride channel. *The Journal of
experimental biology*. 203:1947-1962.

Mense, M., P. Vergani, D.M. White, G. Altberg, A.C. Nairn, and D.C. Gadsby. 2006. In
vivo phosphorylation of CFTR promotes formation of a nucleotide-binding
domain heterodimer. *EMBO J*. 25:4728-4739.

Norimatsu, Y., A. Ivetac, C. Alexander, J. Kirkham, N. O'Donnell, D.C. Dawson, and
M.S. Sansom. 2012. Cystic fibrosis transmembrane conductance regulator: a
molecular model defines the architecture of the anion conduction path and locates
a "bottleneck" in the pore. *Biochemistry*. 51:2199-2212.

Ostedgaard, L.S., C.S. Rogers, Q. Dong, C.O. Randak, D.W. Vermeer, T. Rokhlina, P.H. Karp, and M.J. Welsh. 2007. Processing and function of CFTR-DeltaF508 are species-dependent. *Proceedings of the National Academy of Sciences of the United States of America*. 104:15370-15375.

Riordan, J.R., J.M. Rommens, B. Kerem, N. Alon, R. Rozmahel, Z. Grzelczak, J. Zielenski, S. Lok, N. Plavsic, J.L. Chou, and et al. 1989. Identification of the cystic fibrosis gene: cloning and characterization of complementary DNA. *Science*. 245:1066-1073.

Seeger, M.A., and H.W. van Veen. 2009. Molecular basis of multidrug transport by ABC transporters. *Biochimica et Biophysica Acta (BBA) - Proteins and Proteomics*. 1794:725-737.

Szollosi, D., D. Rose-Sperling, U.A. Hellmich, and T. Stockner. 2017. Comparison of mechanistic transport cycle models of ABC exporters. *Biochimica et biophysica acta*.

Tata, F., P. Stanier, C. Wicking, S. Halford, H. Kruyer, N.J. Lench, P.J. Scambler, C. Hansen, J.C. Braman, R. Williamson, and et al. 1991. Cloning the mouse homolog of the human cystic fibrosis transmembrane conductance regulator gene. *Genomics*. 10:301-307.

Tsai, M.F., M. Li, and T.C. Hwang. 2010. Stable ATP binding mediated by a partial NBD dimer of the CFTR chloride channel. *The Journal of general physiology*. 135:399-414.

Tsai, M.F., H. Shimizu, Y. Sohma, M. Li, and T.C. Hwang. 2009. State-dependent modulation of CFTR gating by pyrophosphate. *The Journal of general physiology*. 133:405-419.

Van Goor, F., S. Hadida, P.D. Grootenhuis, B. Burton, D. Cao, T. Neuberger, A. Turnbull, A. Singh, J. Joubran, A. Hazlewood, J. Zhou, J. McCartney, V. Arumugam, C. Decker, J. Yang, C. Young, E.R. Olson, J.J. Wine, R.A. Frizzell, M. Ashlock, and P. Negulescu. 2009. Rescue of CF airway epithelial cell function in vitro by a CFTR potentiator, VX-770. *Proceedings of the National Academy of Sciences of the United States of America*. 106:18825-18830.

Vergani, P., S.W. Lockless, A.C. Nairn, and D.C. Gadsby. 2005. CFTR channel opening by ATP-driven tight dimerization of its nucleotide-binding domains. *Nature*. 433:876-880.

Vergani, P., A.C. Nairn, and D.C. Gadsby. 2003. On the mechanism of MgATP-dependent gating of CFTR Cl- channels. *The Journal of general physiology*. 121:17-36.

Wang, W., Y. El Hiani, and P. Linsdell. 2011. Alignment of transmembrane regions in the cystic fibrosis transmembrane conductance regulator chloride channel pore. *The Journal of general physiology*. 138:165-178.

Welsh, M.J., M.P. Anderson, D.P. Rich, H.A. Berger, G.M. Denning, L.S. Ostedgaard, D.N. Sheppard, S.H. Cheng, R.J. Gregory, and A.E. Smith. 1992. Cystic fibrosis transmembrane conductance regulator: a chloride channel with novel regulation. *Neuron*. 8:821-829.

Winter, M.C., D.N. Sheppard, M.R. Carson, and M.J. Welsh. 1994. Effect of ATP concentration on CFTR Cl- channels: a kinetic analysis of channel regulation. *Biophys J*. 66:1398-1403.

Yeh, H.I., Y. Sohma, K. Conrath, and T.C. Hwang. 2017. A common mechanism for CFTR potentiators. *The Journal of general physiology*.

Yeh, H.I., J.T. Yeh, and T.C. Hwang. 2015. Modulation of CFTR gating by permeant ions. *The Journal of general physiology*. 145:47-60.

Yorifuji, T., W.K. Lemna, C.F. Ballard, C.L. Rosenbloom, R. Rozmahel, N. Plavsic, L.C. Tsui, and A.L. Beaudet. 1991. Molecular cloning and sequence analysis of the murine cDNA for the cystic fibrosis transmembrane conductance regulator. *Genomics*. 10:547-550.

Yu, Y.C., Y. Sohma, and T.C. Hwang. 2016. On the mechanism of gating defects caused by the R117H mutation in cystic fibrosis transmembrane conductance regulator. *The Journal of physiology*. 594:3227-3244.

Zhang, J., and T.C. Hwang. 2015. The Fifth Transmembrane Segment of Cystic Fibrosis Transmembrane Conductance Regulator Contributes to Its Anion Permeation Pathway. *Biochemistry*. 54:3839-3850.

Zhang, J., and T.C. Hwang. 2017. Electrostatic tuning of the pre- and post-hydrolytic open states in CFTR. *The Journal of general physiology*. 149:355-372.

Zhang, Z., and J. Chen. 2016. Atomic Structure of the Cystic Fibrosis Transmembrane Conductance Regulator. *Cell*. 167:1586-1597 e1589.

Zhang, Z., F. Liu, and J. Chen. 2017. Conformational Changes of CFTR upon

    Phosphorylation and ATP Binding. *Cell*.

Zhou, Z., S. Hu, and T.C. Hwang. 2001. Voltage-dependent flickery block of an open

    cystic fibrosis transmembrane conductance regulator (CFTR) channel pore. *The*

    Journal of physiology. 532:435-448.

Zhou, Z., X. Wang, H.Y. Liu, X. Zou, M. Li, and T.C. Hwang. 2006. The two ATP

    binding sites of cystic fibrosis transmembrane conductance regulator (CFTR) play

    distinct roles in gating kinetics and energetics. *The Journal of general physiology*.

    128:413-422.

CHAPTER 5

Future directions

5.1 Overview

Our knowledge about the structure and function of CFTR has been magnified due to fruitful research in the field over the past ten years. While many basic questions regarding the fundamental properties of CFTR have been addressed, some of them are still under debate. Accumulated biophysical studies using SCAM have revealed the structure of the channel permeation pathway at the residue level. Key residues within the gate or selectivity filer (such as T338, F337, S341and L102) or those critical in tuning the electrostatic profile of the pore (such as R352, R303 and K95), or those required for maintaining open channel stability (such as D993, D924 and R347) were identified (see details in review by Hwang et al., 2018). The basic structure of the two NBDs, their dimer conformation and the role of ATP molecules in gating were also described.

The mission to characterize CFTR from a static snapshot angle was basically accomplished. Next era will demand researchers to not only characterize CFTR with higher spatial and temporal resolution, but also to understand a CFTR from a dynamic angle. More studies to address a dynamic CFTR have become urgent given that a solid foundation built by the tremendous amount of functional data is now available.

With the helpful cryo-EM CFTR structures currently available (Zhang and Chen, 2016; Liu et al., 2017; Zhang et al., 2017) and hopefully more structures are coming out down the road, future experimental design will be more accurate, efficient and feasible.

So in the following sections, I will propose a few testable ideas based on the insights derived from my previous work (Chapter 2-4) and the work from my colleagues and many other groups, with the hope of projecting a few productive research directions that can continue generating useful information to advance the field of CFTR study.

5.2 Utilize the O_1O_2 phenotype to reexam previous ATP hydrolysis related gating issues and facilitate future gating studies.

The mutations showing the O_1O_2 phenotype clearly differentiate the pre- and post-hydrolytic open states within one opening burst, which provide a higher resolution to observe the timing of ATP hydrolysis event more directly (Gunderson and Kopito, 1995; Ishihara and Welsh, 1997; Zhang and Hwang, 2017). This advantage of the O_1O_2 phenotype can be applied widely to study the hydrolysis related gating mechanism and is particularly useful in studying the mutations within the TMDs, which not only affect the channel conductance but also alter the gating behavior of CFTR. For instance, K978C, a mutation in the cytoplasmic end of TM9 (Figure 5.1A) shows a largely increased P_o (0.9 vs 0.5 for WT-CFTR Yeh et al., 2015) with a reduced single-channel amplitude (Figure 5.1B). However, the mechanism behind the increase of P_o is still unclear. According to the cryo-EM structure of human CFTR, K978 seems to be involved in interacting with part of the Regulatory Domain which obstructs the NBD dimer interface (Figure 5.1A) (Liu et al., 2017). Nevertheless, introducing N306D or M348R/R352C should be able to resolve more detailed events happening within the long opening burst.
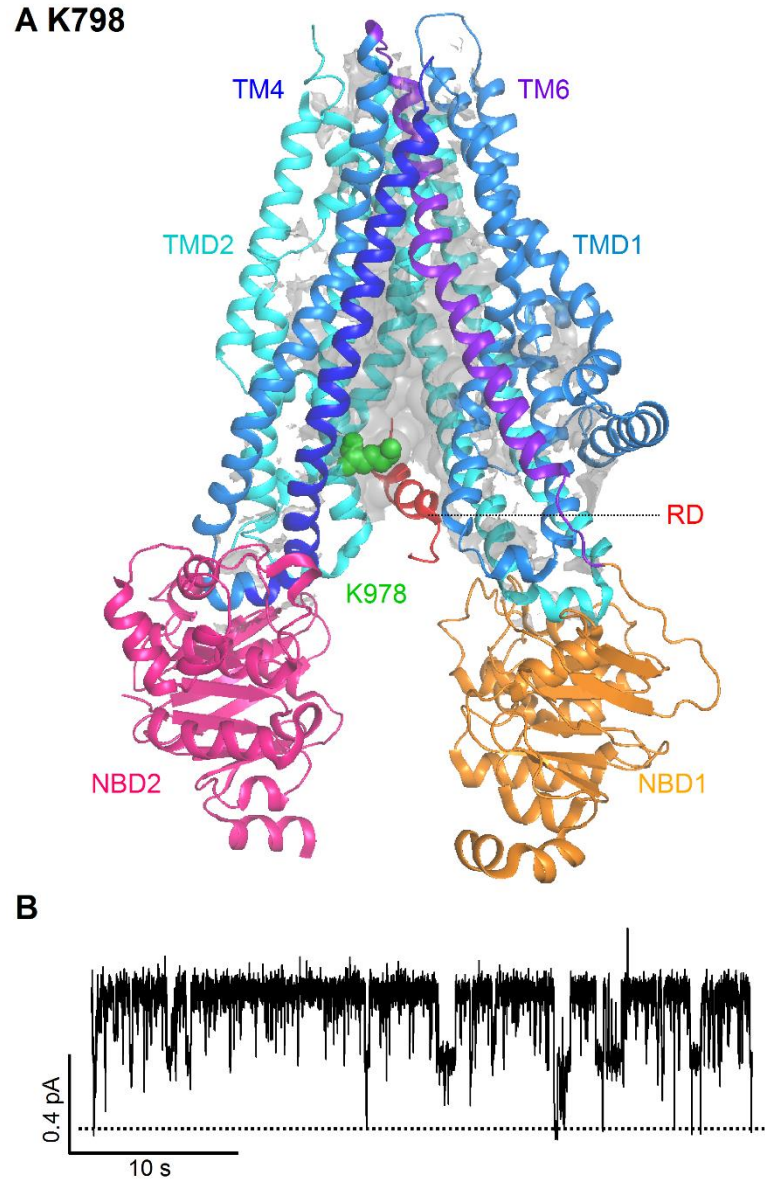
Figure 5.1 Location of K978 and the *Po* of K978C. A. K978 (green spheres) is located close to the cytoplasmic end of TM9, a location where a small portion of the RD is sandwiched between the two halves of the protein. K978 may directly interact with the RD and indirectly interact with the NBDs. **B.** A representative single-channel recording of K978C in the presence of 2 mM ATP with two channels opening with P_o close to unity. Dashed line represents the baseline current when two channel are both closed. The single-channel amplitude of K978C is decreased to around 0.3 pA, likely due to the neutralization of a positive charge.

A similar mutation is L102C/Cysless in TM1, located at the outer limit of the internal vestibule. The single-channel recording of L102C/Cysless shows sick gating behavior, similar to that of R117H (Gao et al., 2013; Yu et al., 2016). Surprisingly, once modified by MTSET$^+$, the L102C/Cysless channel becomes locked in the open state with reduced conductance and ATP-independent (Gao et al., 2013). Similar pore-lining residues showing altered gating behaviors once modified also include M348C/Cysless and I344C/Cysless modified by MTSET$^+$ (Bai et al., 2010). The studying of ATP hydrolysis events in these mutations not only offer deeper insight about why theses mutations are locked open but also offer straight forward insights to answer one critical question: if ATP hydrolysis at the NBDs is altered by mutations in the TMDs? If yes, how come?

Studies combining these mutants with the O_1O_2 phenotype will also provide key evidence to resolve the controversial "re-entry" events, a process happens when ATP hydrolytic products are released from the NBD dimer interface in the open state but before the channels closes, another ATP molecule enters the vacant NBD binding site 2 to induce a second round of NBD dimerization and prolong the existing open burst (Jih and Hwang, 2012; Jih et al., 2012). The "re-entry" events challenge the one-to-one stoichiometry between CFTR gating cycles and the numbers of ATP hydrolyzed. Since for WT-CFTR, such "re-entry" events do not happen frequently due the brief open time of WT-CFTR, the gain-of-function mutations aforementioned offer a diverse platform to test whether the "re-entry" events are indeed common in CFTR gating.

The O_1O_2 phenotype should also be applied to re-exam the mechanism of mutations at the NBD dimer interface that are proposed to alter ATP binding, or NBD dimerization

or ATP hydrolysis, such as Y1219I, W401G and G551D. The O_1O_2 phenotype should also be helpful in investigating the intriguing surprisingly high spontaneous opening mutants such as mutation K978C (Figure 5.2) and F1296S/N1303Q (Figure 5.3 and Figure 5.4).
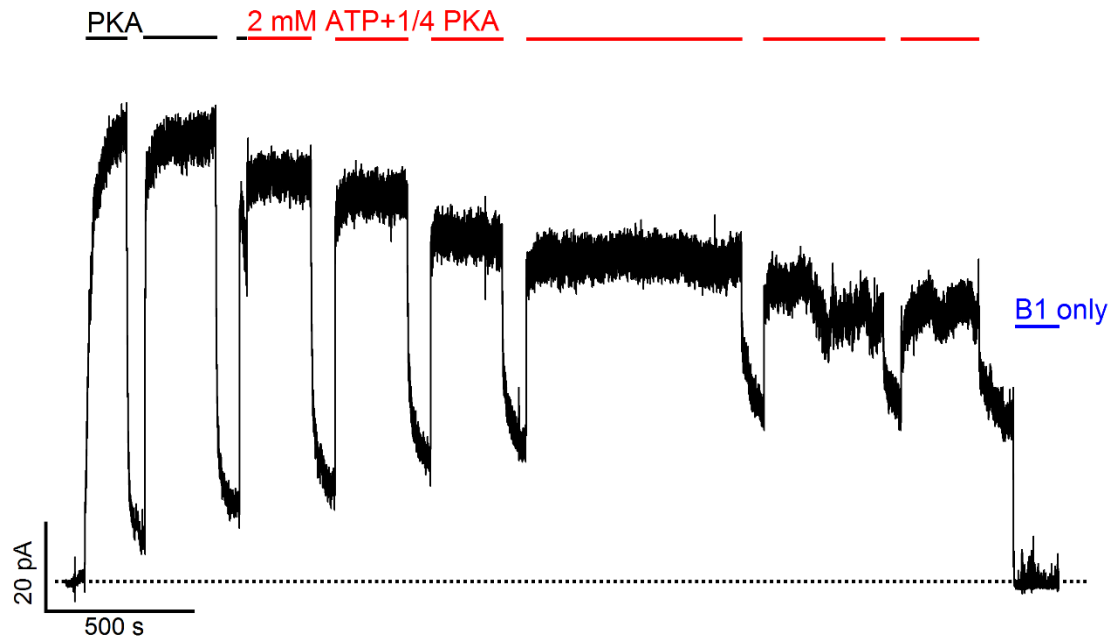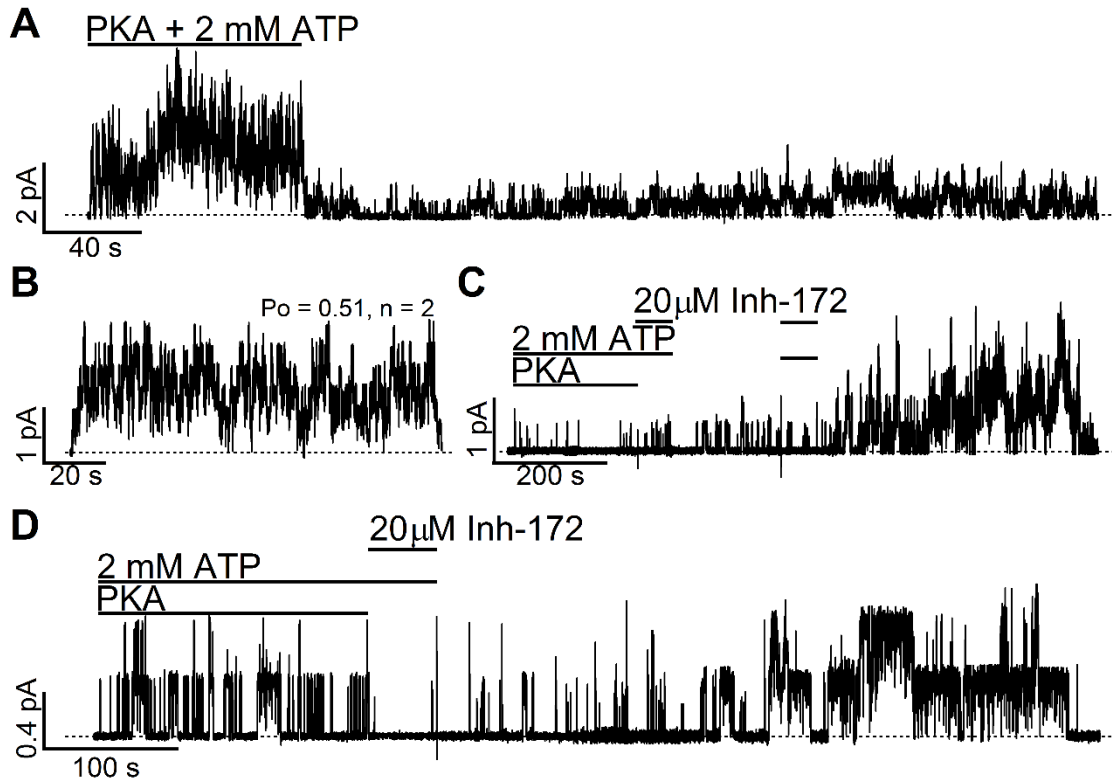
Figure 5.2 Time dependent increase of K978C spontaneous opening activity. The spontaneous (ATP-independent) opening of K978C shows clear time-dependent increase. Application of Inhibitor-172 (B1) at the end of the recording confirmed that the large residual spontaneous current after ATP washout is indeed CFTR current.
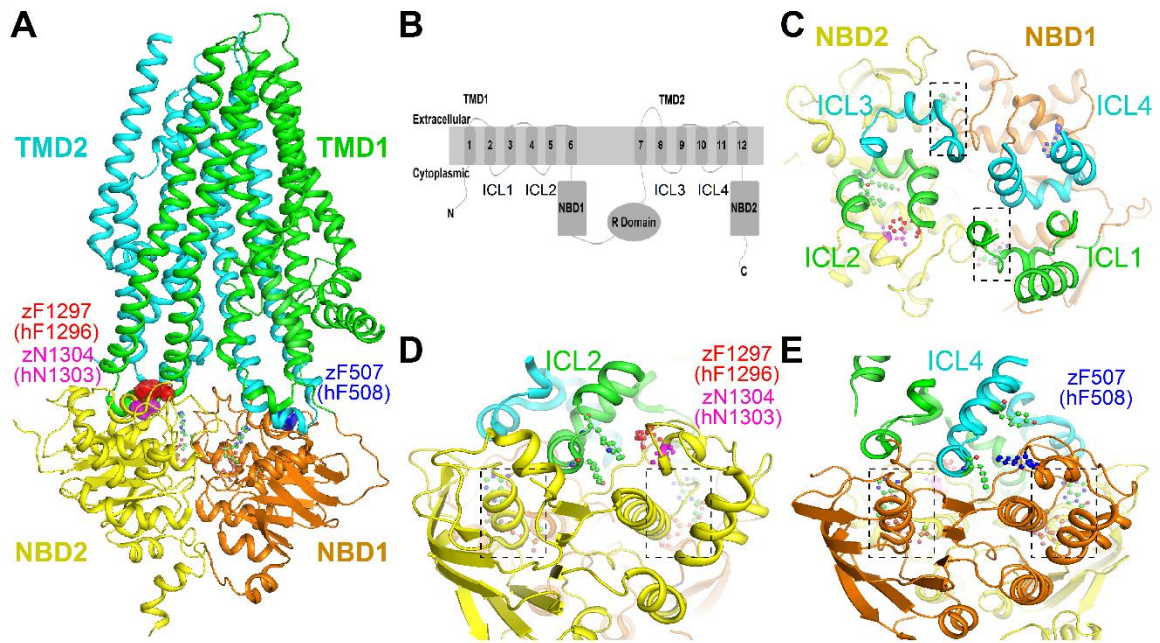
Figure 5.3 F1296 and N1303 are located at the coupling pocket between ICL2 and NBD2. A. Similar

to K978C, the double mutant F1296S/N1303Q also shows dramatic increase of spontaneous current (see

Figure 5.4 below). Different from K978C in TM9 (Figure 5.1), the double mutant F1296S/N1303Q resides

right in the ICL2-NBD2 coupling pocket. **B.** Basic topology model of CFTR representing a heterodimer of

two TMD-NBD complexes linked by a RD, which suggest a pseudo-symmetrical arrangement of the

residues across the whole protein. **C.** Top view suggest that double mutant F1296S/N1303Q resides in a

critical location, which is almost a mirror of F508. **D.** Lateral view shows that double mutant

F1296S/N1303Q resides within the ICL2-NBD2 coupling pocket. **E.** Lateral view suggests that F508 reside

in the ICL4-NBD1 coupling pocket.

Figure 5.4 F1296S/N1303Q shows time-dependent increase of spontaneous open activity. A. A representative recording with brief application of PKA+ATP cocktail shows obvious increases of the spontaneous openings after long time in the absence of PKA and ATP. **B.** The early stage steady-state current of F1296S/N1303Q in the presence of 2 mM ATP shows a P_o ~ 0.5, very close to that of WT-CFTR. **C.** A representative recording with even briefer application of PKA and ATP cocktail shows a dramatic increase of spontaneous current to a level much higher than that in the presence of PKA and ATP cocktail. **D.** A representative recording with brief application of PKA and ATP cocktail shows that the high spontaneous current seems to come from some channels with extensively prolonged open time duration.

5.3 Is part of TM8 pore-lining, at least temporally? What is the role of TM8 in gating and selectivity?

10 out of 12 TMs have been thoroughly investigated as regard to their roles in pore forming. In short, TM1 (Wang et al., 2011; Gao et al., 2013), TM3 (Norimatsu et al., 2012; El Hiani et al., 2016), TM4 (El Hiani et al., 2016), TM5 (Zhang and Hwang, 2015; El Hiani et al., 2016), TM6 (Fatehi and Linsdell, 2008; Alexander et al., 2009; Bai et al., 2010; El Hiani and Linsdell, 2010; Norimatsu et al., 2012; El Hiani et al., 2016), TM9 (Norimatsu et al., 2012), TM10 (El Hiani and Linsdell, 2015), TM11 (Wang et al., 2014) and TM12 (Bai et al., 2011; Qian et al., 2011; Norimatsu et al., 2012; Gao and Hwang, 2015) line the pore. On the contrary, TM7 is located peripheral to the protein core and therefore is not pore-lining (Wang et al., 2014; Zhang and Hwang, 2015). It is good time to investigate TM2 and TM8 with thorough SCAM screening especially when TM8 seems to be the major asymmetrical part of the pore architecture and is proposed to play a critical role in the channel gating (Zhang et al., 2017). Again, combining the SCAM study with the O_1O_2 phenotype, we could expect to extract more details about CFTR's structure and gating mechanism from the recordings of TM2 and TM8.

5.4 Can we identify the binding site (s) for CFTR potentiator Vx770 or inhibitor Inh-172 through comparative functional studies among CFTR orthologs?

Functional characterizations of zebrafish CFTR described in Chapter 4 have established differences between zebrafish and human CFTR orthologs. These studies have setup a decent starting point to launch extensive investigations on other orthologs of CFTR, including mouse, rat, pig, chicken, dog, and salmon.

The sequence comparison among CFTR orthologs, once combined with functional studies, could potentially offer a deeper understanding of CFTR's structure, function and evolution pathway. The thorough comparison and categorization of a large pool of CFTR orthologs based on their sequence and functional properties, we may be able to identify the binding sites for CFTR potentiators currently available and even provide more candidate binding sites for future drug development. Some of my preliminary data show two different categories: GLPG1837-positive orthologs including human, zebrafish, chicken and GLPG1837-negative orthologs including mouse, rat and surprisingly salmon (Figure 5.5). These CFTR orthologs show different responses not only to potentiator GLPG1837 but also to ATP analogues such as PATP (see example in Chapter 4).
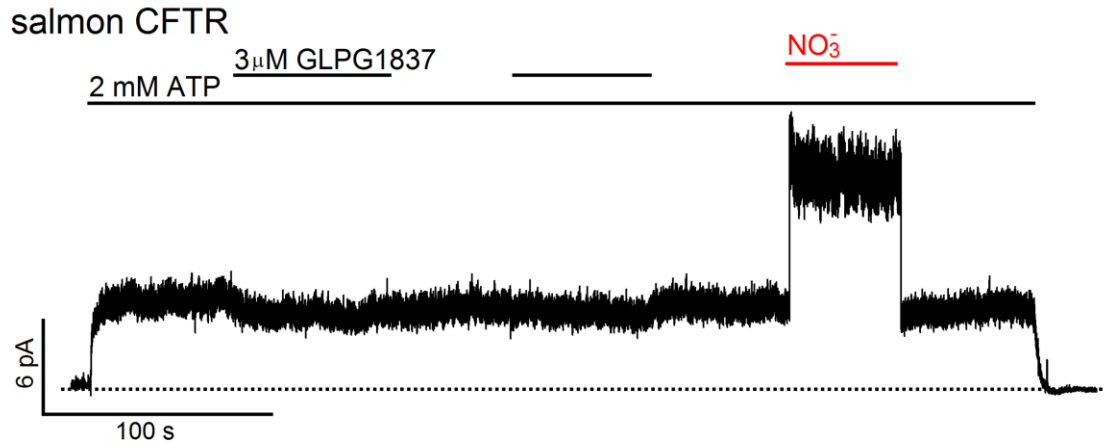
Figure 5.5 Salmon CFTR does not respond to 3 μM GLPG1837. On the contrary, NO_3^- increases the mean current of salmon CFTR by ~ 1.5 folds.

Additionally, mouse CFTR shows an intriguing gating pattering, quite different from both human CFTR and zebrafish CFTR (Chapter 4). Mouse CFTR shows very stable but smaller conductance state overlaid with high frequency of larger conductance but brief opening events, which is also different from the typical the O_1O_2 phenotype (Figure 5.6 compared with Chapter 3). Are these two conductance states in mouse CFTR related with ATP hydrolysis or simply reflecting the thermodynamic motions of part of the TMDs, such as the outer segment of TM8 or TM12? Answers to these questions awaits more studies and may shed light on the relationship between pore architecture and gating transitions.

mouse CFTR
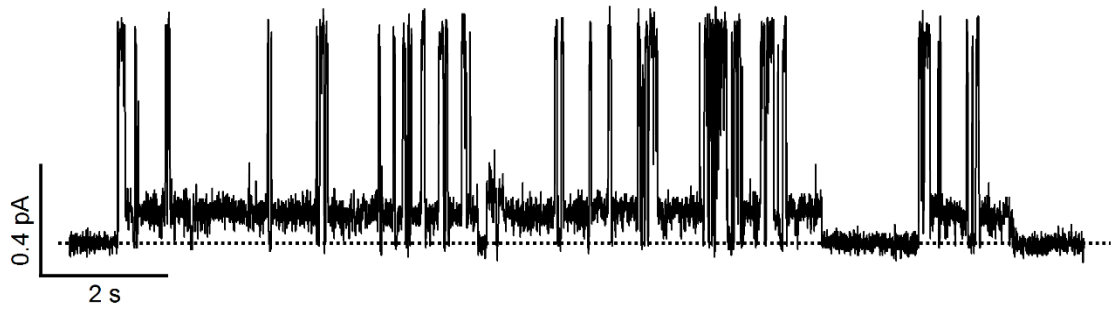
Figure 5.6 Single-channel gating behavior of mouse CFTR. A. representative single-channel recording of mouse CFTR in the presence of 2 mM ATP recorded under -80 mV, suggests two open channel conductance levels: a smaller and stable open state and a much larger but briefer open state. The transitions between these two open states do not follow the preferred gating pattern as C→O_1→O_2→C as seen in the typical O_1O_2 phenotype.

5.5 Conclusions

Over the past years of rigorous scientific training towards my doctoral degree, I have learned the importance of the quality of data, which determines if and to what extent rigorous interpretations can be made. Individual steps and progresses might be small, but gradual accumulations of solid data lay the foundation for a better understanding of the molecular physiology and pharmacology of CFTR. The high-quality, reproducible data I presented in this dissertation are out of a tradition established by my co-workers through more than two decades of relentless pursuit of CFTR physiology.

As a beginner, I started my research focusing on the roles the TM5 and TM7 in pore forming, which form just a small portion of the TMDs. I found that TM5 lines the pore but TM7 does not. As I mastered the basic skills about the biophysical study of CFTR, my experiences led me to explore the relationship between the pore architecture and the process of ATP hydrolysis—a project studying the CFTR protein at a larger scale with an aim to understand CFTR's dynamic motions. I found that very subtle changes in the electrostatic profile of the internal vestibule can confer the O_1O_2 phenotype. Later on with the cryo-EM structures available, I expanded my scale to study the CFTR protein as a whole and globally compared the characteristics between two CFTR orthologs, human and zebrafish CFTR. The comparative study reemphasized that CFTR is so complicated that minor structural variance can result in dramatic functional divergences and meanwhile brought up one mechanistically important possibility that the closed state zebrafish CFTR may hydrolyze ATP.

With more cut-edge techniques emerging in the future, we can expect expedition in CFTR study and optimistically hope that a cure of CF is just around the corner.

5.6 References

Alexander, C., A. Ivetac, X. Liu, Y. Norimatsu, J.R. Serrano, A. Landstrom, M. Sansom, and D.C. Dawson. 2009. Cystic Fibrosis Transmembrane Conductance Regulator: Using Differential Reactivity toward Channel-Permeant and Channel-Impermeant Thiol-Reactive Probes To Test a Molecular Model for the Pore. *Biochemistry*. 48:10078-10088.

Bai, Y., M. Li, and T.C. Hwang. 2010. Dual roles of the sixth transmembrane segment of the CFTR chloride channel in gating and permeation. *The Journal of general physiology*. 136:293-309.

Bai, Y., M. Li, and T.C. Hwang. 2011. Structural basis for the channel function of a degraded ABC transporter, CFTR (ABCC7). *The Journal of general physiology*. 138:495-507.

El Hiani, Y., and P. Linsdell. 2010. Changes in accessibility of cytoplasmic substances to the pore associated with activation of the cystic fibrosis transmembrane conductance regulator chloride channel. *The Journal of biological chemistry*. 285:32126-32140.

El Hiani, Y., and P. Linsdell. 2015. Functional Architecture of the Cytoplasmic Entrance to the Cystic Fibrosis Transmembrane Conductance Regulator Chloride Channel Pore. *The Journal of biological chemistry*. 290:15855-15865.

El Hiani, Y., A. Negoda, and P. Linsdell. 2016. Cytoplasmic pathway followed by chloride ions to enter the CFTR channel pore. *Cellular and molecular life sciences : CMLS*. 73:1917-1925.

Fatehi, M., and P. Linsdell. 2008. State-dependent access of anions to the cystic fibrosis transmembrane conductance regulator chloride channel pore. *The Journal of biological chemistry*. 283:6102-6109.

Gao, X., Y. Bai, and T.C. Hwang. 2013. Cysteine scanning of CFTR's first transmembrane segment reveals its plausible roles in gating and permeation. *Biophys J*. 104:786-797.

Gao, X., and T.C. Hwang. 2015. Localizing a gate in CFTR. *Proceedings of the National Academy of Sciences of the United States of America*.

Gunderson, K.L., and R.R. Kopito. 1995. Conformational states of CFTR associated with channel gating: the role ATP binding and hydrolysis. *Cell*. 82:231-239.

Hwang, T.C., J.T. Yeh, J. Zhang, Y.C. Yu, H.I. Yeh, and S. Destefano. 2018. Structural mechanisms of CFTR function and dysfunction. *The Journal of general physiology*.

Ishihara, H., and M.J. Welsh. 1997. Block by MOPS reveals a conformation change in the CFTR pore produced by ATP hydrolysis. *The American journal of physiology*. 273:C1278-1289.

Jih, K.Y., and T.C. Hwang. 2012. Nonequilibrium gating of CFTR on an equilibrium theme. *Physiology*. 27:351-361.

Jih, K.Y., Y. Sohma, and T.C. Hwang. 2012. Nonintegral stoichiometry in CFTR gating revealed by a pore-lining mutation. *The Journal of general physiology*. 140:347-359.

Liu, F., Z. Zhang, L. Csanady, D.C. Gadsby, and J. Chen. 2017. Molecular Structure of the Human CFTR Ion Channel. *Cell*. 169:85-95 e88.

Norimatsu, Y., A. Ivetac, C. Alexander, J. Kirkham, N. O'Donnell, D.C. Dawson, and M.S.P. Sansom. 2012. Cystic Fibrosis Transmembrane Conductance Regulator: A Molecular Model Defines the Architecture of the Anion Conduction Path and Locates a "Bottleneck" in the Pore. *Biochemistry*. 51:2199-2212.

Qian, F., Y. El Hiani, and P. Linsdell. 2011. Functional arrangement of the 12th transmembrane region in the CFTR chloride channel pore based on functional investigation of a cysteine-less CFTR variant. *Pflugers Archiv : European journal of physiology*. 462:559-571.

Wang, W., Y. El Hiani, H.N. Rubaiy, and P. Linsdell. 2014. Relative contribution of different transmembrane segments to the CFTR chloride channel pore. *Pflugers Archiv : European journal of physiology*. 466:477-490.

Yu, Y.C., Y. Sohma, and T.C. Hwang. 2016. On the mechanism of gating defects caused by the R117H mutation in cystic fibrosis transmembrane conductance regulator. *The Journal of physiology*. 594:3227-3244.

Zhang, J., and T.C. Hwang. 2015. The Fifth Transmembrane Segment of Cystic Fibrosis Transmembrane Conductance Regulator Contributes to Its Anion Permeation Pathway. *Biochemistry*. 54:3839-3850.

Zhang, J., and T.C. Hwang. 2017. Electrostatic tuning of the pre- and post-hydrolytic open states in CFTR. *The Journal of general physiology*. 149:355-372.

Zhang, Z., and J. Chen. 2016. Atomic Structure of the Cystic Fibrosis Transmembrane
Conductance Regulator. *Cell*. 167:1586-1597 e1589.

Zhang, Z., F. Liu, and J. Chen. 2017. Conformational Changes of CFTR upon
Phosphorylation and ATP Binding. *Cell*.

VITA

Jingyao Zhang was born in Linkou city, Heilongjiang Province, the northernmost province of China, in January, 1988. He grew up living with his grandparents and finished his middle school in Linkou city. Then he started his boarding school life in Harbin No. 3 High School in Harbin, the capital city of Heilongjiang Province, which is 7 hours away from Linkou city by train. After graduated from high school, he attended Zhejiang University in Zhejiang Province, a southern coastal city which is even more distant from Linkou city, 40 hours one-way by train in 2006.

He graduated from Zhejiang University with a BS in Biological Engineering and then entered the University of Missouri-Columbia, Missouri to pursue the degree of doctor of philosophy in Biological Engineering since 2012.